CHALMERS
UNIVERSITY OF TECHNOLOGY

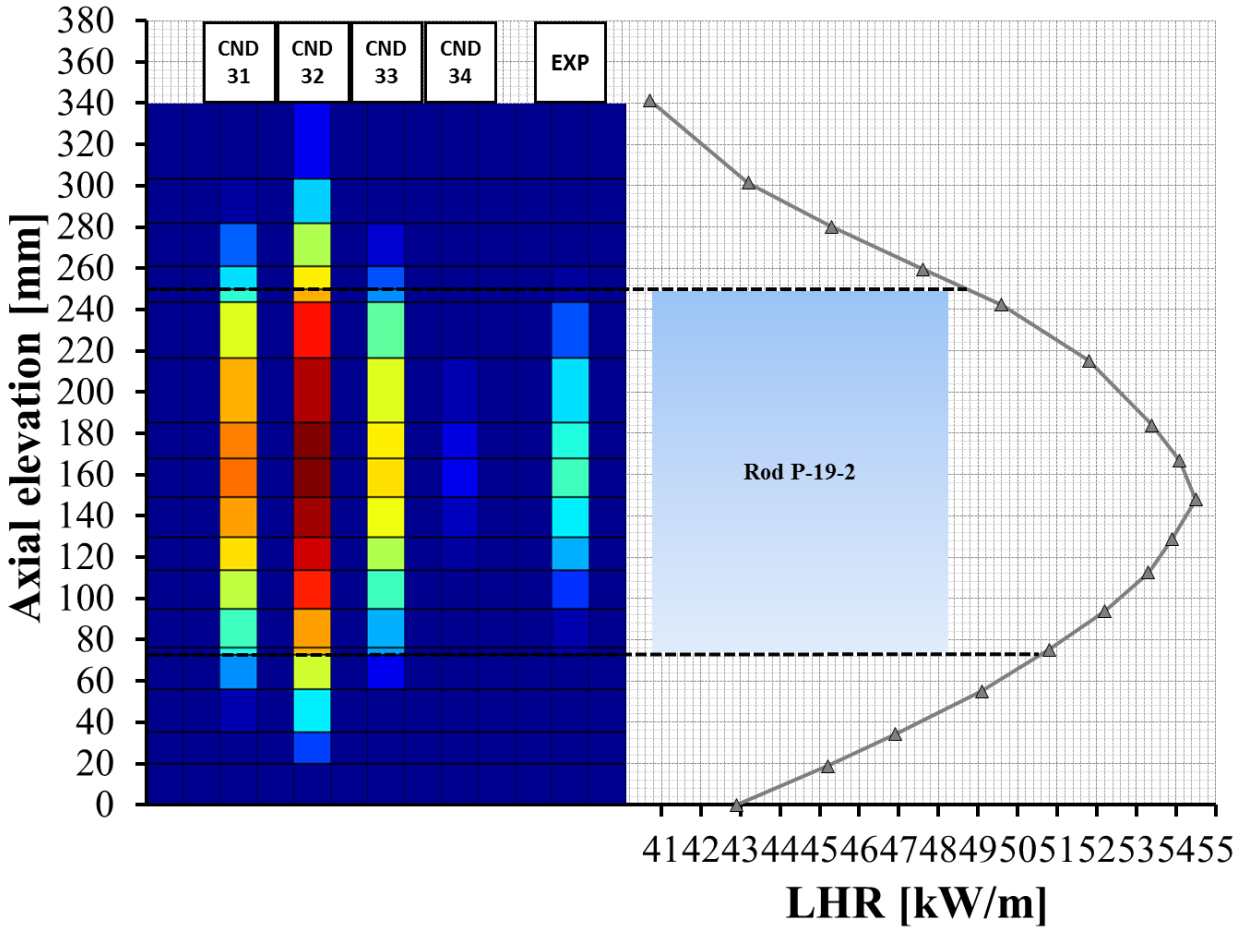

Modelling thermal dependent phenomena of MOX fuel with focus on thermal conductivity

Master's thesis in Nuclear Engineering

Ahmed Aly

Department of Applied Physics
Division of Nuclear Engineering
CHALMERS UNIVERSITY OF TECHNOLOGY
Gothenburg, Sweden 2015
CTH-NT-312

CTH-NT-312

Modelling thermal dependent phenomena of MOX fuel with focus on thermal conductivity

Master's Degree Thesis
Master Program of Nuclear Engineering
CHALMERS UNIVERSITY OF TECHNOLOGY

Ahmed Aly

Department of Applied Physics
Division of Nuclear Engineering
CHALMERS UNIVERSITY OF TECHNOLOGY
Gothenburg, Sweden 2015

Modelling thermal dependent phenomena of MOX fuel with focus on thermal conductivity
Master's Degree Thesis
Ahmed Aly

Master's thesis
CTH-NT-312
Department of Applied Physics
Division of Nuclear Engineering
Chalmers University of Technology
SE-412 96 Gothenburg
Sweden
TEL: +46 (0)31-772 1000

Sponsor:
PELGRIMM EC project

Cover:
Melting heights and fractions predicted by TRANSURANUS code Vs the experimental measurement along with the corresponding linear heat rate needed to cause incipient melting in rod P-19-2.

Chalmers Reproservice
Gothenburg, Sweden 2015

Modelling thermal dependent phenomena of MOX fuel with focus on thermal conductivity
Master's thesis in Nuclear Engineering
Ahmed Aly
Department of Applied Physics
Division of Nuclear Engineering
Chalmers University of Technology

Abstract

Among the parameters that govern the myriad of processes that occur during irradiation of fuel rods, the fuel temperature is by far the most important one. The correct prediction of the fuel temperature profile is therefore the basis for the simulation of integral fuel rods by means of fuel performance codes. It is therefore of critical importance to any computer code used for simulation of integral fuel rod behavior to be able to predict the thermal conductivity of the fuel correctly since it directly affects the temperature.

The present activity is conducted in the framework of the PELGRIMM EC Project and deals with the assessment of MOX fuel conductivity correlations used in the TRANSURANUS code and comparing them to open literature correlations and experimental data then verifying the code against selected integral fuel rod experiments done for both thermal and fast reactors. In order to assess the thermal conductivity correlations of MOX fuel, other phenomena that would affect the prediction of temperature have been investigated as well in order to capture the integral behavior of MOX for thermal and fast reactors. This step helped in assessing the ability of thermal conductivity correlations to predict fuel temperature while excluding the effects of other phenomena meanwhile giving a general information about the ability of different models to predict the phenomenon they predict.

It was shown during this work that TRANSURANUS is able to predict temperature, hence the thermal conductivity of thermal reactor MOX with high accuracy. On the other hand, the work revealed a potential field of improvement to predict the thermal conductivity of FR grade MOX, especially if not of stoichiometric grade and if in fresh conditions. However, the code seems to be on the conservative side when modeling FR MOX. A first step in this improvement was taken in this work and targeted the modification of the high temperature thermal conductivity term in order to be able to obtain a better, less conservative prediction of the melting of FR fuel rods early in life in the reactor core.
Keywords: Thermal conductivity, MOX, TRANSURANUS, LWR, FBR, Fuel temperature, Fuel Melting, Halden, HBWR, EBR-II

Acknowledgements

I would like to show my appreciation to PELGRIMM for financing this thesis work and trusting me to do it. I got out of it with a good experience that I could not imagine getting it elsewhere. I am very thankful to my supervisors Dr. Alessandro Del Nevo and Dr. Davide Rozzia from ENEA research center in Brasimone, Bologna, Italy for all the managerial and scientific help they provided to me. I am thankful to Alessandro Del Nevo for all his comments and the guidance he gave during the whole scheme of the work, for how he helped facilitating any difficulties I faced and for being such an inspiring personality, that one looks up to. I cannot imagine this thesis to be done without the thorough supervision of Davide Rozzia. I am grateful for all the knowledge I gained from him and that he did not keep anything out of my reach and always enthusiastically gave answers and solutions to all my questions and how he guided me to perform all the needed tasks quicker. I am also so grateful to my co-worker and landlord Ms. Graziella Tonelli for being such a great host, for her help during my first days in Italy, and during the hard times of my shoulder injury. I am thankful to her beautiful family that surrounded me with love during my stay in Italy.

I am totally grateful to Prof. Christophe Demazière my teacher and examiner from Chalmers university for all the knowledge I gained from him during my master program study that made this thesis possible. I am truly honored to have him as my examiner. I am thankful as well to everyone that I met in ENEA Brasimone for the friendly atmosphere they surrounded me with, and for the magnificent coffee times we had together that made everyday work fun.

I would not forget to thank my former student counsellor Ms. Pia Hepsever and the current one Ms. Helena Sörquist for helping me to obtain my residence permit in a quick manner. This Helped me focus on the tasks of my thesis.

And last but not least, I am grateful to my beloved brother Amr Aly for being there for me during my whole life and for his moral support and encouragement during my stay in Italy that never made me feel lonely.

Ahmed Aly,
Gothenburg, 19/5/2015.

CONTENTS

ABSTRACT I

ABBREVIATIONS VI

LIST OF FIGURES AND TABLES VII

1 INTRODUCTION 1

1.1 Objective of the activity 1

1.2 Framework of the activity 1

2 THEORETICAL BACKGROUND 3

2.1 Thermal conductivity of ceramic fuel 3

2.2 Effect of temperature 4

2.3 Effect of stoichiometry 5

2.4 Effect of burn-up 5

2.5 Effect of fuel porosity 6

2.6 Effect of Plutonium content 7

2.7 Summary of parameters affecting thermal conductivity 7

3 MOX FUEL CONDUCTIVITY CORRELATIONS 9

3.1 TRANSURANUS correlations 9

3.1.1 Correlation by Van Uffelen and Schubert 9

3.1.2 Correlation by Carbajo 9

3.1.3 Correlation by Lanning and Beyer 11

3.1.4 Correlation by Wiesenack. 11

3.2 Open Literature correlations 12

3.2.1 Martin review 1982 12

3.2.2 FTHCON subcode-MATPRO 13

3.2.3 The COMETHE formulation-1982 14

3.2.4 Baron Hervè 1995 Model 14

3.3 Experimental data and correlations 15

3.4 Conclusive remarks 20

4 TRANSURANUS CODE 23

4.1 Thermal Analysis 23

4.1.1 Basic Equations 24

4.1.2 Boundary Conditions 24

4.1.3 Heat transfer 25

4.2 Mechanical analysis 25
4.2.1 Boundary conditions 26
4.3 Burn-up Equations 27
4.3.1 The RADAR model 28
4.3.2 The TRANSURANUS-LWR Burn-up Model 28

5 ANALYSIS OF LWR MOX: IFA-597 EXPERIMENT 29

5.1 Description of the experiment 29
5.1.1 Background and objective of the experiment 29
5.1.2 Halden Boiling Water Reactor (HBWR) 29
5.1.3 Design of the rig and rods 32
5.1.4 Linear Heat rating (LHR) 33
5.2 Modelling IFA597.4/.5 with TU 34
5.2.1 Development of TU input file 34
5.2.2 Boundary conditions 35
5.2.3 Burn-up investigation 36
5.3 Reference analysis of IFA597.4/.5 37
5.3.1 Fuel temperature 37
5.3.2 FGR and pin pressurization 37
5.4 Sensitivity analysis 42
5.4.1 Linear heat rating uncertainty 43
5.4.2 Thermal conductivity correlations 46
5.4.3 Relocation models 47
5.4.4 Swelling correlations 48
5.4.5 FGR models 50
5.4.6 Gap conductance models 51
5.4.7 Other parameters 52
5.5 Radial analysis 53
5.5.1 IFA597.4 Radial analysis (5 MWD/kgU) 54
5.5.2 IFA597.5 Radial analysis (24 MWD/kgU) 56

6 ANALYSIS OF FR MOX: HEDL P-19 EXPERIMENT 59

6.1 Description of the experiment 59
6.1.1 Background and objective of the experiment 59
6.1.2 Experimental breeder reactor #2 (EBR-II) 61
6.2 Modelling HEDL P-19 with TU 63
6.2.1 Development of TU input file 63
6.2.2 Boundary conditions 64
6.3 Reference analysis of HEDL P-19 rods 65
6.3.1 Temperature prediction 65
6.3.2 Gap width 66
6.3.3 Central void 66

6.3.4 Columnar grains 66
6.3.5 Melting radius 66
6.3.6 Melting elevation 67
6.4 Sensitivity analysis 74
6.4.1 Thermal conductivity correlations 75
6.4.2 Relocation models analysis 78
6.4.3 Solidus-liquidus melting models 78
6.4.4 Fuel restructuring models 79
6.4.5 Initial gap width 80
6.5 Radial analysis 81
7 REVIEW OF THERMAL CONDUCTIVITY CORRELATIONS 85
8 CONCLUSION 93
REFERENCES 95

Abbreviations

ANL	Argonne National Laboratory
at.%	Atomic percentage
BH-95	Baron-Hervè 1995
BOL	Beginning Of Life
BU	BurnUp
BWR	Boiling Water Reactor
Cs	Cesium
EBR-II	Experimental Breeder Reactor #2
El	Electronic
EOL	End Of Life
FBR	Fast Breeder Reactor
FD	Dissolved Fission products
FFTF	Fast Flux Test Facility
FGR	Fission Gas Release
FP	Precipitated Fission products
FR	Radiation Factor/ Fast Reactor
Gd_2O_3	Gadolinia
HBWR	Heavy Boiling Water Reactor
HEDL	Hanford Engineering Development Laboratory
HPG	Halden Project Group
HRP	Halden Reactor Project
IFA	Instrumental Fuel Assembly
ITU	Institute for TransUranium elements
Kr	Krypton
Latt	Lattice
LHR	Linear Heat Rate
LMFBR	Liquid Metal Fast Breeder Reactor
LWR	Light Water Reactor
MA	Minor Actinides
mfp	mean free path
MIMAS	Micronized MAster blend
MOX	Mixed OXide fuel
Nd	Neodymium
OL	Open Literature
O/M	Oxygen to Metal ratio
P	Porosity
PCMI	Pellet Cladding Mechanical Interaction
PIE	Post Irradiation Evaluation
PuO_2	Plutonium dioxide
PWR	Pressurized Water Reactor
Rad	Radiation
RADAR	RAting Depressing Analysis routine
TD	Theoretical Density
TU	TRANSURANUS
UO_2	Uranium dioxide
wt.%	Weight percentage
X	Deviation from stoichiometry
Xe	Xenon
Zr	Zirconium

List of figures and tables

Figure 2-1 $(U\text{-}Pu)_y\text{-}O_x$ fuel total thermal conductivity along with its different constituting components. *4*

Figure 2-2 $(U\text{-}Pu)_y\text{-}O_x$ conductivity: effect of deviation from stoichiometry on the thermal conductivity. *5*

Figure 2-3 $(U\text{-}Pu)_y\text{-}O_x$ conductivity: effect of burn-up on the thermal conductivity. *6*

Figure 3-1 MOX thermal conductivity: comparison between correlations and experimental data for 100%TD, O/M=2, PU=20 wt.%. *16*

Figure 3-2 MOX thermal conductivity: comparison between correlations and experimental data for 95%TD, O/M=2, PU=20 wt.%. *17*

Figure 3-3 MOX thermal conductivity: comparison between Wiesenack correlation and experimental data for 95%TD, O/M=2, PU=20 wt.%. *17*

Figure 3-4 MOX thermal conductivity: comparison between correlations and experimental data for 95%TD, O/M=1.98, PU=20 wt.%. *18*

Figure 3-5 MOX thermal conductivity: comparison between correlations and experimental data for 95%TD, O/M=1.93, PU=20 wt.%. *19*

Figure 3-6 MOX thermal conductivity: comparison between correlations and experimental data for 95%TD, O/M=2, PU=6 wt.%. *20*

Figure 4-1 Four possible modes of an interaction between fuel and cladding. [11] *27*

Figure 5-1 HBWR, schematic diagram and main operation parameters. [21] *31*

Figure 5-2 HBWR, plan view of the reactor top lid and main parameters. [21] *31*

Figure 5-3 IFA-597 experiment, schematic radial view of the test rig. [2] *33*

Figure 5-4 Linear heat rating of solid and hollow rods. *34*

Figure 5-5 Simulation of IFA-597, preliminary results: burn-up analysis. *37*

Figure 5-6 Simulation of IFA-597, reference results: fuel temperature evolution in rod 10. ..... *39*

Figure 5-7 Simulation of IFA-597, reference results: fuel temperature evolution in rod 11. ..... *39*

Figure 5-8 Simulation of IFA-597, reference results: FGR evolution in rod 10. ..... *40*

Figure 5-9 Simulation of IFA-597, reference results: FGR evolution in rod 11. ..... *40*

Figure 5-10 Simulation of IFA-597, reference results: pin pressure evolution in rod 10. ..... *41*

Figure 5-11 Simulation of IFA-597, reference results: pin pressure evolution in rod 11. ..... *41*

Figure 5-12 Simulation of IFA-597, sensitivity analysis on LHR, fuel temperature. *44*

Figure 5-13 Simulation of IFA-597, sensitivity analysis on LHR, FGR. *44*

Figure 5-14 Simulation of IFA-597, sensitivity analysis on LHR, rod pressure. *45*

Figure 5-15 Simulation of IFA-597, sensitivity analysis on LHR, variation on fuel centreline prediction of rod-10. ..... *45*

Figure 5-16 Simulation of IFA-597, sensitivity analysis on LHR, variation on rod pressure prediction of rod-10. ..... *45*

Figure 5-17 Simulation of IFA-597, sensitivity analysis on fuel conductivity correlations, temperature prediction. *46*

Figure 5-18 Simulation of IFA-597, sensitivity analysis on fuel conductivity correlations, rod pressure and FGR prediction. *47*

Figure 5-19 Simulation of IFA-597, sensitivity analysis on relocation models, temperature prediction. 48

Figure 5-20 Simulation of IFA-597, sensitivity analysis on relocation models, Pressure & FGR prediction. 48

Figure 5-21 Simulation of IFA-597, sensitivity analysis on swelling correlations, temperature prediction. 49

Figure 5-22 Simulation of IFA-597, sensitivity analysis on swelling correlations, rod pressure and FGR prediction. 50

Figure 5-23 Simulation of IFA-597, sensitivity analysis on FGR: Intra-granular model coupled with inter-granular model IGRBDM=3, temperature and FGR predictions. 51

Figure 5-24 Simulation of IFA-597, sensitivity analysis on FGR: Inter-granular models coupled with intra-granular model FGRMOD=6, temperature and FGR predictions. 51

Figure 5-25 Simulation of IFA-597, sensitivity analysis on gap conductance, temperature prediction. 52

Figure 5-26 IFA-597, temperature radial profile at 5MWd/kgHM as function of the conductivity correlation adopted 54

Figure 5-27 IFA-597 at 5 MWd/kgHM, thermal conductivity profiles when applied to rod-10, comparison with open literature correlations and experimental data 55

Figure 5-28 IFA-597 at 5MWd/kgHM, thermal conductivity profiles when applied to rod-11, comparison with open literature correlations and experimental data. 55

Figure 5-29 IFA-597, temperature radial profile at 24MWd/kgHM as function of the conductivity correlation adopted 56

Figure 5-30 IFA-597 at 24 MWd/kgHM, thermal conductivity profiles when applied to rod-10, comparison with open literature correlations and experimental data 57

Figure 5-31 IFA-597 at 24 MWd/kgHM, thermal conductivity profiles when applied to rod-11, comparison with open literature correlations and experimental data 57

Figure 6-1 HEDL P-19, pin power axial profile.[3] 60

Figure 6-2 HEDL P-19, EBR-II power history during the experiment.[3] 61

Figure 6-3 Schematic diagram of EBR-II plant. [29] 62

Figure 6-4 Simulation of HEDL P-19, rod P19-2, LHR at 17 axial elevations. 65

Figure 6-5 Simulation of HEDL P-19, rod P19-2, coolant temperature at 17 axial elevations. 65

Figure 6-6 Simulation of HEDL P-19, rod P19-2, reference analysis, centreline temperature. 67

Figure 6-7 Simulation of HEDL P-19, rod P19-5, reference analysis, centreline temperature. 68

Figure 6-8 Simulation of HEDL P-19, rod P19-2, reference analysis, radial temperature profile at the end of the ramp. 68

Figure 6-9 Simulation of HEDL P-19, rod P19-5, reference analysis, radial temperature profile at the end of the ramp. 69

Figure 6-10 Simulation of HEDL P-19, rod P19-2, reference analysis, prediction of gap width at the end of the experiment. 69

Figure 6-11 Simulation of HEDL P-19, rod P19-5, reference analysis, prediction of gap width at the end of the experiment. 70

Figure 6-12 Simulation of HEDL P-19, rod P19-2, reference analysis, prediction of the central void at the end of the experiment. 70

Figure 6-13 Simulation of HEDL P-19, rod P19-5, reference analysis, prediction of the central void at the end of the experiment. 71

Figure 6-14 Simulation of HEDL P-19, rod P19-2, reference analysis, prediction of the columnar grain radii at the end of the experiment. *71*

Figure 6-15 Simulation of HEDL P-19, rod P19-5, reference analysis, prediction of the columnar grain radii at the end of the experiment. *72*

Figure 6-16 Simulation of HEDL P-19, rod P19-2, reference analysis, prediction of the melting radius. *72*

Figure 6-17 Simulation of HEDL P-19, rod P19-5, reference analysis, prediction of the melting radius. *73*

Figure 6-18 Simulation of HEDL P-19, rod P19-2, reference analysis, prediction of melting height. *73*

Figure 6-19 Simulation of HEDL P-19, rod P19-5, reference analysis, prediction of melting height. *74*

Figure 6-20 Simulation of HEDL-P19, sensitivity analysis on thermal conductivity correlations, prediction of melting height. *76*

Figure 6-21 Simulation of HEDL-P19, sensitivity analysis on thermal conductivity correlations, prediction of gap width at the end of the experiment. *76*

Figure 6-22 Simulation of HEDL-P19, sensitivity analysis on thermal conductivity correlations, prediction of central void at the end of the experiment. *77*

Figure 6-23 Simulation of HEDL-P19, sensitivity analysis on thermal conductivity correlations, prediction of columnar grain radius at the end of the experiment. *77*

Figure 6-24 Simulation of HEDL-P19, sensitivity analysis on thermal conductivity correlations, prediction of melting radii. *77*

Figure 6-25 Simulation of HEDL-P19, sensitivity analysis on relocation models, prediction of gap width at the end of the experiment. *78*

Figure 6-26 Simulation of HEDL-P19, sensitivity analysis on relocation models, prediction of melting height. *78*

Figure 6-27 Simulation of HEDL-P19, sensitivity analysis on melting models, prediction of central void at the end of the experiment. *79*

Figure 6-28 Simulation of HEDL-P19, sensitivity analysis on melting models, prediction of melting height. *79*

Figure 6-29 Simulation of HEDL-P19, sensitivity analysis on restructuring models, columnar grain radii prediction. *80*

Figure 6-30 Simulation of HEDL-P19, sensitivity analysis on initial gap size, prediction of melting height. *80*

Figure 6-31 Simulation of HEDL-P19, sensitivity analysis on, prediction of gap width at the end of the experiment. *81*

Figure 6-32 Radial profile of thermal conductivity for rod P-19-2. ..... *83*

Figure 6-33 Radial profile of thermal conductivity for rod P-19-5. ..... *83*

Figure 7-1 lattice and electronic conductivities comparison. *87*

Figure 7-2 Rod P-19-2, Comparison between the melting heights and fraction according to the original and modified correlations. *88*

Figure 7-3 Rod P-19-2, Comparison between the predicted gap width at the end of the experiment by the original and modified correlations. *88*

Figure 7-4 Rod P-19-2, Prediction of centreline temperature by the original and modified correlations. *89*

Figure 7-5 Rod P-19-5, Comparison between the melting heights and fraction according to the original and modified correlations. *89*

Figure 7-6 Rod P-19-2, Comparison between the predicted gap width at the end of the experiment by the original and modified correlations. *90*

Figure 7-7 Rod P-19-5, Prediction of centreline temperature by the original and modified correlations. *90*

Figure 7-8 Radial comparison of thermal conductivity for rod P-19-2 predicted by the original and the modified correlations. *91*

Table 2-1 Factors affecting thermal conductivity of MOX fuel *7*

Table.3-1 Summary of thermal conductivity correlations for MOX. *15*

Table.3-2 List of experimental data on MOX used for comparison with correlations. *16*

Table 5-1 HBWR, summary of the driver fuel main data. *30*

Table 5-2 IFA-597 experiment, rod characteristics. *32*

Table 5-3 IFA-597 experiment, summary of models and correlations that might affect the prediction of thermal conductivity of the rods. *35*

Table 5-4 IFA-597 experiment, local heat rate measurement positions. *36*

Table 5-5 Simulation of IFA-597, list of correlations, models and design parameters considered in the sensitivity studies. *43*

Table 5-6 IFA-597, summary of radial analysis main data. *54*

Table 6-1 HEDL P-19, design data. [3] *60*

Table 6-2 HEDL P-19, axial extension of fuel melting at the end of the experiment. [3] *60*

Table 6-3 HEDL P-19, measurements of central void, columnar grain radius and TD at pellet center at the end of the experiment. [3] *60*

Table 6-4 Simulation of HEDL P-19, summary of models and correlations that might affect the prediction of thermal conductivity of the rods. *63*

Table 6-5 Simulation of HEDL P-19, axial discretization of the fuel rods. *64*

Table 6-6 Simulation of HEDL-P19, list of correlations, models and design parameters considered in the sensitivity studies *75*

1 Introduction

1.1 Objective of the activity

The development of mixed oxide fuel (MOX) is a strategic option for current and new generation of nuclear reactors. Therefore, it is important to confirm that it can be implemented safely within a reactor system and that its characteristics fit with the type of reactor it will be used in. One of the issues to be investigated, is the assessment of the thermal performance of MOX during irradiation in order to ensure that the fuel element can endure the heat conditions of the reactor core in normal operation and have a safe margin in transient conditions during reactor life.

Among the parameters that governs the myriad of processes that occur during irradiation of fuel rods, the fuel temperature, is by far the most important one (i.e. it dominates the FGR and swelling mechanisms)[1]. The correct prediction of the fuel temperature profile is therefore the basis for the simulation of integral fuel rods by means of fuel performance codes. The objective of this work is to assess the ability of the computer code TRANSURANUS (TU) to predict the performance of MOX fuel rods within thermal and fast reactors with main focus drawn on thermal conductivity. Thorough investigation is given to the thermal conductivity prediction since it is the direct parameter used in determining the temperature profile and the prediction of melting in the investigated fuel rods. Various phenomena occurring in MOX fuel (densification, swelling, relocation, etc.) during irradiation were investigated to assess the integral capability of the code to model the thermal performance of the rods.
The study involves the analysis of four MOX rods. Two of them were irradiated in Halden heavy boiling water reactor (HBWR) within the IFA-597 experiment. The other two were irradiated in experimental breeder reactor #2 (EBR-II) for Hanford Engineering Development Laboratory HEDL P-19 experiment.
The IFA-597.4/.5/.6 experiment was done within the framework of the Halden reactor project (HRP) to investigate the thermal performance and FGR characteristics of MOX fuel. The main objective was to gather in-pile measurements of two MOX rods (solid and hollow) that can be used for further analysis and give more insight about the behavior of MOX within thermal, water cooled reactors. Another objective was the investigation of the difference between the behavior of MOX in solid rods and hollow rods.[2]
HEDL P-19 experiment took place in 1971 in the EBR-II reactor to investigate the effect of initial fuel-to-cladding diametral gap sizes on the linear-heat-rate needed to cause incipient fuel melting (power-to-melt), Q'_m, at beginning-of-life. Sixteen fresh MOX fueled rods representative of the Fast Flux Test Facility (FFTF) driver fuel were irradiated in this test. The results can also be projected on FBR fuel as well. The rods were subjected to power ramps at a specific designed linear power to induce melting. Some of the rods experienced melting and some did not. In this work, two rods P-19-2 (that experienced melting) and P-19-5 (that did not experience melting) were investigated.[3]

1.2 Framework of the activity

The activity is conducted in the framework of the PELGRIMM EC Project. PELGRIMM is a 4 year project, addressing Minor-Actinide (MA) bearing fuel developments for Generation IV Fast Reactor Systems to support the Strategic Research Agenda (SRA) of the European Sustainable Nuclear Energy –Technology Platform (SNE-TP). Both options, MA homogeneous recycle in driver fuels with MA content at a few percent, and heterogeneous recycle on UO_2 fuels bearing high MA contents, located in the radial core blanket, are considered. Two fuel forms (pellet and spherepac) will be investigated. Indeed, spherepac technology (that leads to production of beads that can be directly loaded in pins) is attractive regarding MA-bearing fuels as it would lead to a significant simplification

of the fabrication process and to a better accommodation of solid swelling (compared to pellets) under irradiation. These developments extend Europe's leading role in this area.
A total of 12 partners from research institutions, education establishments and industries will collaborate to share and leverage their skills, progress and achievements, covering a comprehensive set of investigations: fuel fabrication, fuel behaviour under irradiation through an irradiation test and the execution of Post Irradiation Examinations, modelling and simulation of fuel behaviour and performance under irradiation, from normal operating conditions to severe accidents, and finally by providing unique education and training possibilities.[30]

2 Theoretical background

2.1 Thermal conductivity of ceramic fuel

Thermal conductivity is a property representing the ability of a solid material to transfer heat. There are three phenomena considered when modelling thermal conductivity. Lattice vibrations, Radiation Heat Transfer and electronic conductivity [4].

Lattice vibration thermal conductivity (k_{latt}) is modelled by assuming the solid to be an ideal gas consisting of phonons. Phonons are quasi particles representing the wave nature of the vibrating solid in the lattice. They tend to collide with each other and with defects in the crystal with a certain mean free path. They transport their energy as they translate in the medium from the hot side to the cold one. Thermal conductivity depends on the amount of energy a phonon can carry and the mean free path of the phonon[5]. Phonon's mean free path should be inversely proportional to the temperature. Due to the presence of point defects in the crystal solid that acts as a barrier to phonon's mobility, the mean free path cannot keep monotonically increasing as the temperatures get lower[5]. This requires that the mean free path is inversely proportional to temperature plus an extra constant term representing phonon scattering with defects. Being proportional to the mean free path of the phonon, k_{latt} would be written as:

$$k_{latt} = \frac{1}{A + BT} \qquad \textit{Eq. 2-1}$$

Where *A*, and *B* are constants, and *T* is the temperature in (K).

Heat is conducted as well with radiation on the form of electromagnetic waves. Energy is transported due to the movement of charged particles (protons and electrons) which emit some of their energy on the form of electromagnetic radiation[5][6]. Radiation term of thermal conductivity (k_{rad}) is written on the form of a constant times the cube of temperature:

$$k_{rad} = CT^3 \qquad \textit{Eq. 2-2}$$

At temperatures high enough, energy is sufficient to generate an amount of electron-hole pairs that contribute to thermal conductivity (k_{el})[7].

$$k_{el} = 2\left(\frac{K_b}{e}\right)^2 T\left[\sigma + \frac{2\sigma_e\sigma_h}{\sigma}\left(\frac{E_g}{2K_bT} + 2\right)\right] \qquad \textit{Eq. 2-3}$$

Where:
k_{el}= electronic contribution to thermal conductivity.
K_b= Boltzmann constant, 1.38x10^{23} (J/K)
e= electron charge, 1.6x10^{-19} (Coul)
$\sigma_{e/h}$= electron/hole contribution to electrical conductivity ($\frac{1}{\Omega}$m)
$\sigma \quad = \sigma_e + \sigma_h$ ($\frac{1}{\Omega}$m)
E_g = energy gap between conduction and valence bands (J)

The first term on the right hand side of Eq. 2-3 is the conductivity effect of holes and electrons separately. The second term represents the ambipolar effect, which is the release of the kinetic energy of both the electron and the hole when they recombine together plus the release of their generation energy at areas of lower temperature leading to the transfer of heat electronically.

This equation can be simplified using some experimental data and assumptions to be written on the form:[4]

$$k_{el} = D\frac{e^{\frac{-E}{T}}}{T^n} \qquad \textit{Eq. 2-4}$$

Where *D*, *E* and *n* are constants. It should be noted that *n* differs from one model to another.

These physical principles of heat conduction and their equation forms are generally taken into account in the models even if they can be implemented in different ways. In general, all the thermal conductivity models implemented in fuel pin mechanic codes take the lattice vibration term into account and most of them will include one of the other two principles. Few models take all three principles into account.

2.2 Effect of temperature

Thermal conductivity of UOx and MOX is a property that depends on temperature. It has been noted experimentally that the thermal conductivity decreases with temperature until a minimum is reached in the range between 1500 to 2000 K as shown in *Figure 2-1*. This decrease is due to the lattice vibration term, which is inversely proportional to the temperature. At temperatures above the plateau range, the thermal conductivity begins to rise again due to the radiation and electronic term. Radiation heat conduction takes place above the plateau temperature even though it is not that much significant[5]. Electronic term of the thermal conductivity is the second term that is responsible for the increase of thermal conductivity.
As usual, the lattice vibration is implemented including other factors that affect the heat conductivity other than temperature (e.g. burn-up rate, deviation from stoichiometry, etc). Some models, take the radiation conduction term into consideration to explain the increase of thermal conductivity at higher temperatures, while others relate that increase to the electronic conduction term.

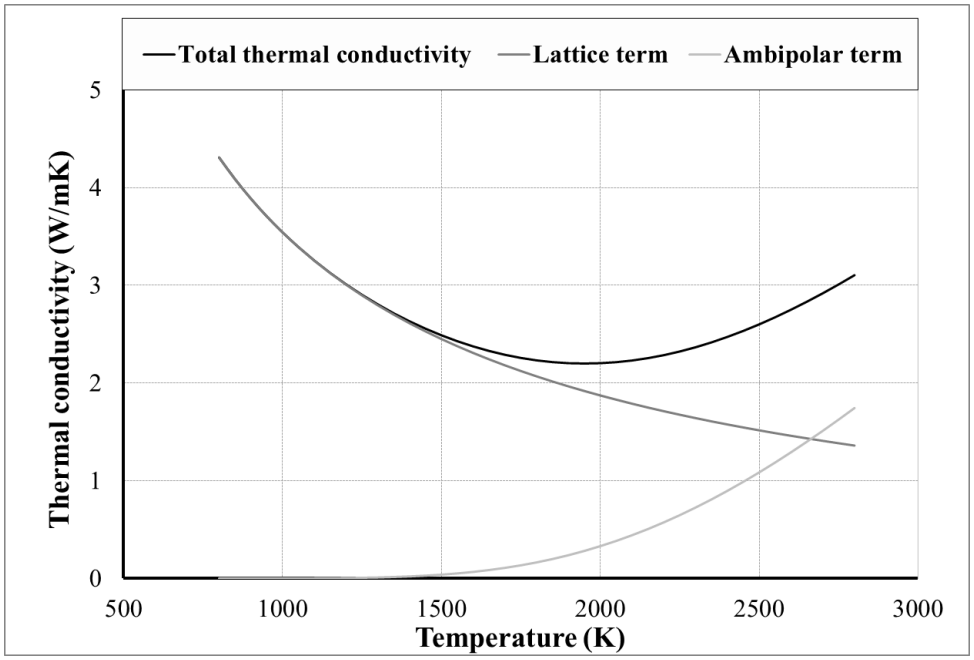

Figure 2-1 $(U\text{-}Pu)_y\text{-}O_x$ fuel total thermal conductivity along with its different constituting components.

2.3 Effect of stoichiometry

The theoretical oxygen to metal ratio (O/M) between Uranium or Plutonium oxide (U-Pu)O_2 is two. Deviation from this value is generally adopted by design and is induced in the nuclear fuel as effect of irradiation. The deviation can lead to hyper (>2) or hypo (<2) stoichiometric state of the fuel[8].
The effect of deviation from stoichiometry is generally modelled by assuming that this deviation causes more defects in the lattice. This perturbation is included in the constant A in Eq. 2-1 which represents the phonon-defect interaction in the lattice and is determined originally for stoichiometric fuel conditions.

The modification of Eq. 2-1 due to deviation from stoichiometry can be written as:

$$k_{latt} = \frac{1}{A_0 + C\mathrm{x} + BT} \qquad \textit{Eq. 2-5}$$

Where A_0 is the constant *A* for stoichiometric fuel and *C* is a constant multiplied by x which is the deviation form stoichiometry (O/M-2). Therefore, the higher the deviation from stoichiometry, the lower the thermal conductivity becomes (*Figure 2-2*). Deviation from stoichiometry also affects the behavior of thermal conductivity with temperature. In facts, as the fuel deviates from stoichiometry the lower the temperature at which the thermal conductivity reaches its minimum. It can be noticed as well that the effect of deviation from stoichiometry is important at lower temperatures while at higher temperature where the ambipolar term is more important, and the effect of deviation from stoichiometry is less significant.

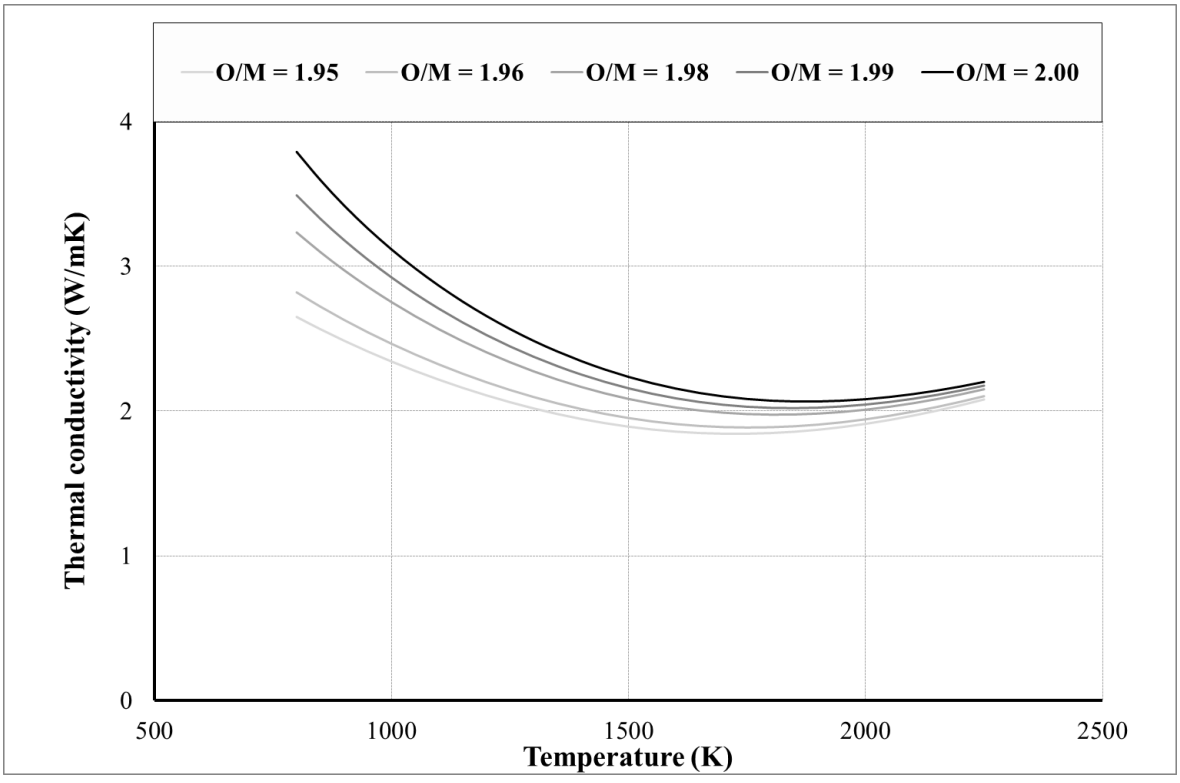

Figure 2-2 (U-Pu)$_y$-O$_x$ conductivity: effect of deviation from stoichiometry on the thermal conductivity.

2.4 Effect of burn-up

The irradiation process that takes place in a nuclear reactor leads to various changes in the properties of the fuel pellet. Defects in the lattice, porosity increase, deviation from stoichiometry and fuel

cracking with irradiation lead to degradation of the thermal conductivity. This effect is important in fast reactors (FR) since burn-up can reach to more than 10% of the original weight content of the uranium and plutonium[8]. Solid fission products have different effects on thermal conductivity. In general, those that are dissolved tend to decrease the thermal conductivity, while those that are precipitated tends to increase it. Fission gases result in thermal conductivity degradation. The integral effect is however a degradation of conductivity with increasing burn-ups.

It is noticed as well that the higher the burn-up, the lower the rate of change of thermal conductivity with temperature *Figure 2-3*. Also as the burn-up increases, the lower the temperature for which the thermal conductivity reaches its minimum becomes before it increases again. At burn-up of 80 $\frac{MWd}{kgHM}$, the thermal conductivity is slightly changing with temperature until the temperature is above 1500 K where the effect of the ambipolar term of thermal conductivity starts to rise. This behavior is explained by the increase of the defects in the solid due to irradiation. As a consequence of this, the phonon-defect interaction in the fuel dominates with respect to the temperature dependent phonon-phonon interaction term.

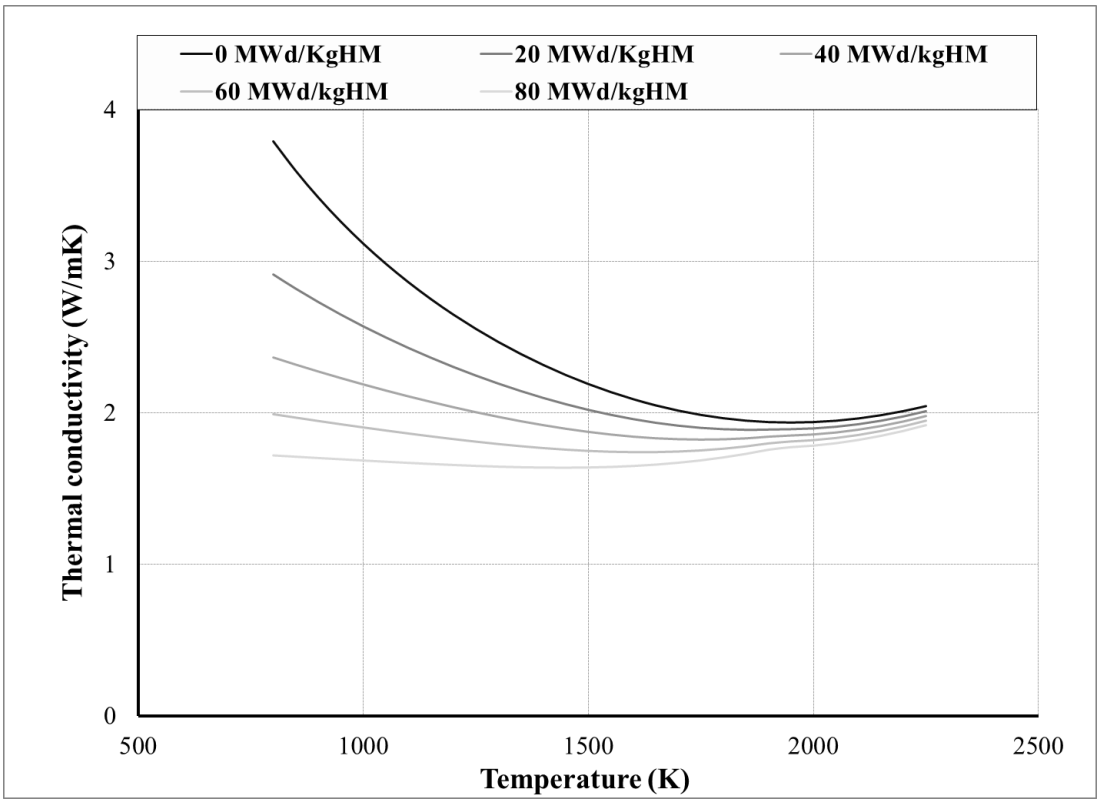

Figure 2-3 $(U\text{-}Pu)_y\text{-}O_x$ conductivity: effect of burn-up on the thermal conductivity.

2.5 Effect of fuel porosity

The presence of voids in the solid fuel pin leads to degradation of its thermal conductivity. A poreless fuel is required to obtain the maximum thermal conductivity. On the other side, the presence of pores in the fuel pin is important to accommodate the release of fission gases that are formed during irradiation. Fission gases can cause internal pressure of the fuel pin to increase leading to deformation and swelling of the fuel. This effect is more important for fast reactors than thermal reactors because the higher power density leads to more generation of fission gases [8].
The porosity (*P*) is defined as the volume of the pores inside the fuel divided by the total volume of the fuel. This can be written as:

$$P = 1 - \frac{\rho}{\rho_{TD}} \qquad \textit{Eq. 2-6}$$

Where ρ is the smeared density of the fuel, and ρ_{TD} is the theoretical density of the fuel's material without pores. The effect of porosity on thermal conductivity is considered by using a correction factor of the thermal conductivity. This factor has many formulations but the most used are the modified Loeb formula:

$$k = k_{TD}(1 - \alpha P) \qquad \textit{Eq. 2-7}$$

or the Maxwell-Eucken formula:

$$k = k_{TD}\frac{1-P}{1+\beta P} \qquad \textit{Eq. 2-8}$$

Where k_{TD} is the thermal conductivity of the poreless fuel, α and β are constants. Theoretically, the values of α is 1 and β is 0.5. Experimentally, the noticed values of these factors are higher than what the theory predicts. This is due to the fact that the pores are not randomly distributed in the lattice[9]. The wide range of values used for the constants α and β shows that they are in fact variables that depend on the pore shape. The values assigned to them represent an average of the porosity effect.

2.6 Effect of Plutonium content

The effect of Plutonium on the constants *A* and *B* in the lattice vibration thermal conductivity term has been carefully studied. Evidence does not show any systematic trend for the variation of the constant A, while it shows a systematic increase of the constant *B* in Eq. 2-1. Overall the effect of increasing Plutonium's content in the fuel is a decrease of the thermal conductivity of MOX fuel[5]. This decrease reaches up to 15% for a plutonium content of around 25 wt.%.

2.7 Summary of parameters affecting thermal conductivity

Table 2-1 summarizes the main factors affecting thermal conductivity of MOX fuel and the type of effect they have. The weight of the effect of each factor varies between different models as illustrated in later sections in the report for a variety of models.

Factor	**Effect**
Temperature	The main factor that is included in all the models and correlations. Thermal conductivity decreases with Temperature up to 1500-1800 K due to phonon-phonon interaction then increases again due to radiation and electronic conduction.
Deviation from stoichiometry	Decrease or increase of stoichiometry (2±X) leads to a decrease in thermal conductivity.
Burn-up	Thermal conductivity degrades with burn-up.
Porosity	The more decrease of the smeared density of the fuel from the theoretical density value, the lower the thermal conductivity becomes.
Plutonium content	Increase of the plutonium content of the fuel results in a degradation of the thermal conductivity of the fuel.

Table 2-1 Factors affecting thermal conductivity of MOX fuel.

3 MOX fuel conductivity correlations

In this chapter, the Thermal conductivity correlations adopted in TRANSURANUS code to simulate MOX fuel conductivity[11], open literature correlations and experimental data from various open literature sources are compared with each other. More details about the studied correlations can be found in reference [12].

3.1 TRANSURANUS correlations

3.1.1 Correlation by Van Uffelen and Schubert

This correlation is the standard recommended correlation by TU code. It is based on the data obtained experimentally by Duriez et al. where the laser flash technique was used to measure the thermal diffusivity of MOX fuel. The Pu content of the fuel was between 3-15 wt.%, O/M ratio between 1.95 and 2.0 and in the temperature range between 700-2300 K. The thermal conductivity was modelled by using values of the heat capacity calculated from Kopp's law[10]. The ambipolar electronic thermal conductivity term is based on the work of Ronchi et al. in which they measured the thermal diffusivity and the heat capacity of UO_2 for a temperature range between 500 and 1900°C using an advanced laser-flash technique that gave better results than conventional laser flash methods at high temperatures[15]. The correlation gives the thermal conductivity of MOX as a function of temperature and burn-up:

$$k_{100} = \frac{1}{a + a_1 bu + bT + b_1 bu\, T_p} + \frac{c}{T^2} e^{-\frac{d}{T}} \qquad \textit{Eq. 3-1}$$

Where
a=0.0308
$a1$ =5.498x10^{-3}
b=2.515 x10^{-4}
$b1$= -2.498 x10^{-6}
c= 4.715x x10^{9}
d=16361
T is in K and T_p = min(1923,T), bu is the local burn-up in $\frac{MWd}{kgHM}$
The porosity effect can be taken into account using the following correction formula:

$$k_P = k_{100}(1 - P)^{2.5} \qquad \textit{Eq. 3-2}$$

This correlation has been assessed assuming different conditions. Due to the lattice vibration term, the correlation predicts a decrease of thermal conductivity with temperature until it reaches a minimum around 2000 K and then begins to rise again due to the electronic heat conduction. The effect of burn-up on the thermal conductivity is more important at lower temperature. At 800 K the thermal conductivity decreased by 60% of its original value for un-irradiated fuel when the burn-up reached 100 $\frac{MWd}{kgHM}$. For 2000 K, the thermal conductivity for the same range of burn-up decreases only by 10%.

3.1.2 Correlation by Carbajo

This correlation is based on the work of Carbajo et.al. that takes basis for best value estimation of data available from open literature and available recommendations given in other works. The physically based correlation by Lucuta et al. was recommended. It gives the thermal conductivity as a function of temperature, burn-up, and deviation from stoichiometry along with a porosity correction.

The correlation takes the fuel irradiation into account as well as the effect of dissolved and precipitated solid fission fragments as a separate function from the un-irradiated fully dense fuel element[16].
The thermal conductivity for a 100% TD MOX fuel is given by

$$k_{100} = 1.158x\left(\frac{1}{a_0 + a_1X + (b_0 + b_1X)t_k} + \frac{c}{{t_k}^{2.5}}e^{-\frac{d}{t_k}}\right) x\, FD(bu,T)xFP(bu,T)xFR(T)\ \frac{W}{mK} \qquad \textit{Eq. 3-3}$$

Where
a_0=0.035, a_1=2.85, b_0 =0.286, *b1*= -0.715, *c*= 6400 and *d*=16.35
X is the deviation from stoichiometry,
t_k=$\frac{T}{1000}$ and *T* is the temperature in [K]

The factor *FD* represnts the negative effect of dissolved fission fragments on the thermal conductivity and is defined as:

$$FD(bu_{at},T) = \omega\left[\arctan(\frac{1}{\omega})\right] \qquad \textit{Eq. 3-4}$$

For bu_{at} >0 and

$$FD(0,T) = 1 \qquad \textit{Eq.3-5}$$

where

$$\omega = \frac{1.09}{bu_{at}^{3.265}} + 0.0643\ \left(\frac{T}{bu_{at}}\right)^{1/2} \qquad \text{Eq.3-6}$$

bu_{at} is the burn-up in at.%
The factor *FP* represents the increase in thermal conductivity due to the precipitaed solid fission products:

$$FP(bu_{at},T) = 1 + \frac{0.019bu_{at}}{(3 - 0.019\ bu_{at})\left[1 + exp\left(-\frac{T-1200}{100}\right)\right]} \qquad \textit{Eq.3-7}$$

.
The factor *FR* accounts for radiation effects. It is important below 900 K and reaches near unity rapidly above 900 K and does not play a significant role above that temperautre.

$$FR(T) = 1 - \frac{0.2}{1 + exp\left(\frac{T-900}{80}\right)} \qquad \textit{Eq.3-8}$$

The porosity effect is modelled using the Maxwell-Euckman correction formula

$$k_P = k_{100}(\frac{1-P}{1+2P}) \qquad \text{Eq.3-9}$$

The correlation predicts a decrease of thermal conductivity with temperature due to lattice vibration until it reaches a minimum around 2000 K. Then, it begins to rise again due to the electronic heat conduction. It can be noticed as well that the thermal conductivity decreases with burn-up. The effect of burn-up on the thermal conductivity is more important at lower temperature. At 800 K, the thermal conductivity decreased by 40% of its original value for un-irradiated fuel when the burn-up reached 10 at.%. For 2000 K, the thermal conductivity for the same range of burn-up decreases by 15%.
It can be noticed that the lower the temperature, the higher the degradation of thermal conductivity with deviation from stoichiometry. For 800 K the thermal conductivity decreases by 30% for a

deviation from stoichiometry of 0.05. At 2000 K for the same range of deviations, the decrease of thermal conductivity is around 8% and decreases more as the temperature goes higher.

3.1.3 Correlation by Lanning and Beyer

This correlation gives the thermal conductivity for 95% TD MOX according to Lanning and Beyer. The correlation is based on the work of Duriez et al.[10] It gives the thermal conductivity as a function of temperature, burn-up and deviation from stoichiometry included in the lattice vibration term and another term for ambipolar thermal conductivity that is a function of temperature only.
The thermal conductivity for MOX 95% TD is given by:

$$k_{95} = \frac{1}{(A(X) + B(X)T + f(bu) + (1 - 0.9e^{-0.04bu})xg(bu)xh(T))} + \frac{C_{mod}}{T^2}e^{-\frac{D}{T}} \qquad \text{Eq.3-10}$$

Where:
X is the deviation from stoichiometry and
$A(X) = 0.035 + 2.85X$
$B(X) = (2.86 - 7.15X)x10^{-4}$
$f(bu) = 1.87x10^{-3}xbu$
$g(bu) = 0.038xbu^{0.28}$
$h(T) = \frac{1}{1 + 396e^{\frac{-6380}{T}}}$
$C_{mod} = 1.5x10^{9}$
$D = 13520$
T is in K and the burn-up is in $\frac{MWd}{kgHM}$.
A porosity correction term according to Lucuta is applied to obtain the thermal conductivity at different real densities. The porosity correction is on the form of Maxwell-Euckman formula:

$$k_p = k_{95}x1.0789x\left(\frac{(1-P)}{1+0.5\mathrm{P}}\right) \qquad \text{Eq.3-11}$$

The correlation predicts decrease of thermal conductivity with temperature until it reaches a minimum between 1850 and 1900 K then begins to rise again due to the electronic heat conduction for a 95% TD of the fuel at different burn-ups. The effect of burn-up on the thermal conductivity is more important at lower temperature. The degradation of conductivity is in the order of 40% at 800 K (in the range 0 – 100 MWd/kgHM). At 2000 K, the thermal conductivity for the same range of burn-up decreases by 18%.
The more hypostoichiometric the fuel is, the higher the decrease of the thermal conductivity becomes. For a change of O/M from 2 to 1.95, the decrease in thermal conductivity can reach up to 30% at 800 K. This effect gets lower as the temperature goes high. At 2000 K the reduction in thermal conductivity on the same range of change of O/M ratio is about 8%.

3.1.4 Correlation by Wiesenack.

Correlation 34 is the original Wiesenack's correlation that is developed for UO_2 fuel. In order to apply it for MOX, the correlation is multiplied by a correction factor of 0.92. The original correlation gives the thermal conductivity of MOX as a function of temperature and burn-up on the form:

$$k_{95} = \frac{1}{A_0 + A_1 bu + Bxmin\{1650, \vartheta\} + B_2 buxmin\{1650, \vartheta\}} + Ce^{D\vartheta}\ [\frac{W}{mK}] \qquad \text{Eq.3-12}$$

Where:
$A_0 = 0.1148$

$A_1 = 0.0035$
$B = 2.475x10^{-4}$
$B_2 = -8.24175x10^{-7}$
$C = 0.0132$
$D = 0.00188$

And ϑ is the temperature in [°C] and *bu* is the burn-up in $\frac{MWd}{kgUO2}$
There is no specific equation for porosity correction given for this model so the original MATPRO-11 porosity correction is used:

$$k_P = k_{95}\frac{1-\beta P}{1-0.05\beta} \quad \text{Eq.3-13}$$

Where *P* is the porosity and $\beta = 2.58 - 0.58x10^{-3}\vartheta$

The correlation predicts a decrease of thermal conductivity with temperature until it reaches a minimum between 1700 and 1900 K. For un-irradiated fuel, the minimum of thermal conductivity is reached at 1900 K. The correlation indicates that as the burn-up of the fuel increases, that minimum in thermal conductivity is reached at a lower temperature. The minimum in thermal conductivity at burn-up of 100 $\frac{MWd}{kgUO2}$ is reached at a temperature range between 1500 to 1600 K.
The effect of burn-up on the thermal conductivity is higher at lower temperature. At 800 K the thermal conductivity decreased by 55% of its original value for un-irradiated fuel when the burn-up reached 100 $\frac{MWd}{kgHM}$. For 2000 K, the thermal conductivity for the same range of burn-up decreases by 25%. The burn-up at temperatures higher than 2000 K seems to have a constant effect. The amount of thermal conductivity decrease is the same regardless of the initial level of thermal conductivity.

3.2 Open Literature correlations

In this section, several open literature correlations are described along with the variables that are considered.

3.2.1 Martin review 1982

In his work that was published in 1982, Martin did a re-appraisal of four thermal conductivity correlations by Washington, Aniscough, Killeen and Brandt. He chose one of them to do some amendments on. The correlation chosen was that based on Washington's review in 1973. Even though the correlation by Killeen was the most physically based correlation for stoichiometric fuel, that of Washington was selected since there was no theoretical knowledge to apply the first one to non-stoichiometric fuel. Since the two correlations are close to each other at low and high temperature range, and even in the intermediate one, the deviation of Washington's correlation from that of Killeen should not cause great errors[9]. The data available were reappraised and the few new data that appeared since the work of Washington were added to the review. The correlation seemed to be giving satisfactory results for UO_2 and MOX as a function of temperature and O/M ratio.
The amended correlation can be written for hypostoichiometric MOX as:

$$K_{100} = \frac{1}{0.037 + 3.33X + 2.37.10^{-4}T} + 78.9.10^{-12}T^3 \quad \text{Eq.3-14}$$

The original correlations were tailored for UO_2 and were adapted to MOX by assuming a correction factor of 0.95. The new correlation neglected the effect of irradiation and the plutonium content in the temperature range of 500-2800 ^{0}C. It took the O/M ratio into account in the lattice vibration term.

The porosity correction was based on a modified Loeb formula for porosity level between 0< P <0.1 and based on Maxwell-Euckman formula in the range of 0.1< P <0.2.
The effect of deviation from stoichiometry is a degradation of the thermal conductivity. This effect is predicted from this correlation to be from 42% (at temperature of 800 K) to a value of 18% (at 2000 K, it decreases with temperature) for a stoichiometry change between (2 and 1.95). The effect of stoichiometry keeps decreasing with temperature but it can be considered important on the whole range of normal operation of a thermal and fast reactor fueled with MOX.

3.2.2 FTHCON subcode-MATPRO

The correlation used by the FTHCON subroutine determines the thermal conductivity of un-cracked UO_2 and MOX fuels as a function of temperature, O/M ratio and plutonium content of a solid fuel. It uses a porosity correction based on the Maxwell-Eucken relation. The burn-up is used only to calculate the melting temperature of the fuel. Interpolation is used to remedy the discontinuity of the slope in the temperature range between (1364-2300 K) [7].
The correlation is on the following form:

$$K = \left[\frac{D}{1+(6.5-0.00469T'(1-D)}\right]\left[\frac{C_V}{(A+BT'')(1+3e_{th})}\right] + 5.2997\text{x}10^{-3}\text{Te}^{\left[-\frac{13358}{\text{T}}\right]}\left\{1+0.169\left[\frac{13358}{\text{T}}+2\right]^2\right\} \quad \text{Eq.3-15}$$

Where:
K = Thermal conductivity (W/m.K).
D = fractional theoretical density.
C_V= Phonon contribution to the specific heat at constant volume (J/kg.K). MATPRO correlation for specific heat is used to calculate this factor.
e_{th}= Linear strain caused by thermal expansion for temperatures above 300 K. MATPRO correlation for linear strain is used to calculate this factor for uranium and plutonium then the value is weighted according to the percentage of Plutonium in the fuel.
$A = 0.339 + 12.6X$ represents the point defect contribution to the phonon's mfp, where X is the absolute value of the deviation from stoichiometry.
$B = 0.06867(1 + 0.6238\ PU)$ a factor representing the phonon-phonon scattering contribution to the thermal conductivity, where PU is the weight fraction of the plutonium content of the fuel.
T = Fuel temperature in (K).
T' = Fuel temperature if T<1364 K.
For temperature higher than 1834 K then $D\{1+\ [6.5-0.00469T']\} = -1$
For intermediate range (1364<T<1834), linear interpolation is used to obtain the value of T'
T'' = Fuel temperature if T<1800 K.
2050 if T> 2300 K.
Between 1800<T<2300 linear interpolation is used to obtain the value of T''.
Even though the deviation from stoichiometry is included in the model as a parameter determining thermal conductivity, it is slightly sensible with respect to deviation from stoichiometry (compared to the other models). The maximum change of thermal conductivity at temperature of 500 K is less than 2% and decreases more with temperature to reach less than 0.3% at 3000 K.
The correlation predicts a change of thermal conductivity between 12 to 9% with the plutonium content 0 to 30 wt.% between 500 K and 2250 K respectively. This shows a rate of decrease of 0.4 to 0.3% for every unit wt.% increase in Plutonium content. The results shows that the thermal conductivity is more dependent on Plutonium content than on deviation from stoichiometry.

3.2.3 The COMETHE formulation-1982

This formula is used for UO_2 and MOX fuels. It gives thermal conductivity of 95% TD fuel. A porosity correction is used to give the thermal conductivity at different porosities. The correlation was enhanced to take the plutonium weight percentage into account based on the data from Gibby, Van Crynest and Weilbacher[17]. The formula is written as follows:

$$K_{95TD} = \frac{A_0}{A_1 + A_2 X + (1 + B_0 q)T} + CT^3 \qquad \text{Eq.3-16}$$

Where:
K_{95TD} is given in (W/cm.K)
T = temperature (K)
X = absolute value of deviation from stoichiometry
q = Plutonium content
A_0 = 40.05
A_1 = 129.4
A_2 = 16020
B_0 = 0.8
C = 0.6416x10^{-12}

The model predicts a decrease in thermal conductivity at lower temperature of about 0.5% per wt.% increase in the Plutonium content for stoichiometric fuel. The rate of decrease slightly decreases above 2000 K. The decrease of thermal conductivity with hypostoichiometry can reach up to 42% decrease in thermal conductivity at lower temperatures (800 K). This effect decreases with temperature to reach around 18% decrease with stoichiometric decrease from 2 to 1.95 at 2000 K. For the whole range of temperatures of interest, the change of thermal conductivity with deviation from stoichiometry is higher than that due to increase of plutonium content of the fuel.

3.2.4 Baron Hervè 1995 Model

The model is a modification of the same model that originated in 1994. The modification concerns the high temperature term. It included originally a term relating high temperature conductivity to radiation. The modification substituted this term by another one that considers electronic thermal conductivity instead. This was done based on the work be Delette and Charles[17]. The model takes the temperature, deviation from stoichiometry, plutonium and Gadolinium content as variables. In order to apply this model to MOX fuel, the Gadolinium content should be set to zero in Eq.3-17

$$K(T) = \frac{1}{A_0 + A_1 x + A_2 g + A_3 g^2 + (B_0(1 + B_1 q) + B_2 g + B_3 g^2)T + \frac{C + Dg}{T^2}\exp(-\frac{W}{kT})} \qquad \textit{Eq.3-17}$$

Where:
k=Boltzmann constant (1.38.10^{-23} J/K)
W= (1.41*1.6)*10^{-19} J
A_0=4.4819.10^{-2}(m.K/W), A_1=4, A_2=0.611 (m.K/W), A_3=11.081(m.K/W)
B_0= 2.4544.10^{-4}(m/W) , B_1=0.8, B_2=9.603.10^{-4}(m/W), B_3=-1.768.10^{-2}(m/W)
C=5.516.10^{9}(W.K/m)
D=-4.302.10^{10}(W.K/m)
T is temperature in K up to 2600 K,
x is the absolute value of deviation from stoichiometry,

q is the plutonium weight content, and *g* is the Gadolinium weight content.

The model predicts the same effect of Plutonium as in the COMETHE formulation. Similar to the COMETHE formulation, the decrease of thermal conductivity with hypostoichiometry can reach up to 42% decrease in thermal conductivity at lower temperatures (800 K). This effect decreases with temperature to reach around 18% decrease with O/M ratio decrease from 2 to 1.95 (2000 K). For the whole range of temperatures of interest, the change of thermal conductivity with deviation from stoichiometry is higher than that due to the increase of plutonium content of the fuel.

3.3 Experimental data and correlations

In this section, the correlations presented in the previous sections are compared with experimental data from a variety of sources.[10][18][19] The comparison is done at different states of the modeling parameters used in the different correlations to be able to understand how sensitive the models are to those parametric changes and how much they agree with the experimental data at the different levels of the modeling parameters. All the comparisons with experimental data are done at zero burn-up since there were no other data possessed at higher burn-up values. In order to distinguish the TRANSURANUS models from the open literature correlations, the figures mentioned hereafter are plotted with this logic: solid lines will represent TU correlations while the open literature correlations are in dotted lines.
Table.3-1 summarizes the difference between all the studied models in terms of the parameters they take into account. *Table.3-2* summarizes the data sources used in each subsection and their details.

Name of the correlation	Temperature	Deviation from stoichiometry	Burnup	Plutonium content	Porosity	Source
Van Uffelen and Schubert	×		×		×	Standard TU
Carbajo	×	×	×		×	TU
Lanning and Beyer	×	×	×		×	TU
Wiesenack	×		×		×	TU
Martin	×	×		×	×	OL
Matpro	×	×		×	×	OL
COMETHE	×	×		×	×	OL
Baron Hervè	×	×		×	×	OL

Table.3-1 Summary of thermal conductivity correlations for MOX.

Data source	Year	Temperature range (K)	Number of points	Levels of parameters
Van Crynest	1968	813-2188	22	100% TD, O/M=2, Pu= 20 wt.%
Fukushima	1983	826-1817	29	
Hetzler	1987	1066-2143	20	
Van crynest & Weilbacher	N/A	813-2175	26	95%TD, O/M=2, Pu= 20 wt.%
Gibby	1969	825-1882	46	
Schemidt		900-16445	9	
Gibby	1969	917-2244	13	95%TD, O/M=1.98, Pu= 20 wt.%
Weilbacher	1972	893-2685	9	
Bonnoret	1988	1163-2291	20	

Gibby	1969	770-1423	13	95%TD, O/M=1.93, Pu= 20 wt.%
Schemidt	N/A	1110-2054	9	
Van crynest & Weilbacher	N/A	785-2026	6	
Weibacher	1972	778-2370	8	
Duriez	2000	817-2089	32	96%TD, O/M=2, Pu= 6 wt.%
Industrial MIMAS Sample	N/A	812-2083	43	

Table.3-2 List of experimental data on MOX used for comparison with correlations.

1-Comparison at 100% TD, O/M=2, Pu= 20 wt.%

The correlations are compared with experimental data from three sources, *Figure 3-1*. It can be noticed that the data from Van crynst and Hetzler have a large spread that almost covers the whole range of variation between the studied correlations. The data from Fukushima are more precise and it can be seen that Martin's correlation matches it in a quite good manner but in general, no decision with sufficient accuracy can be made from these data.

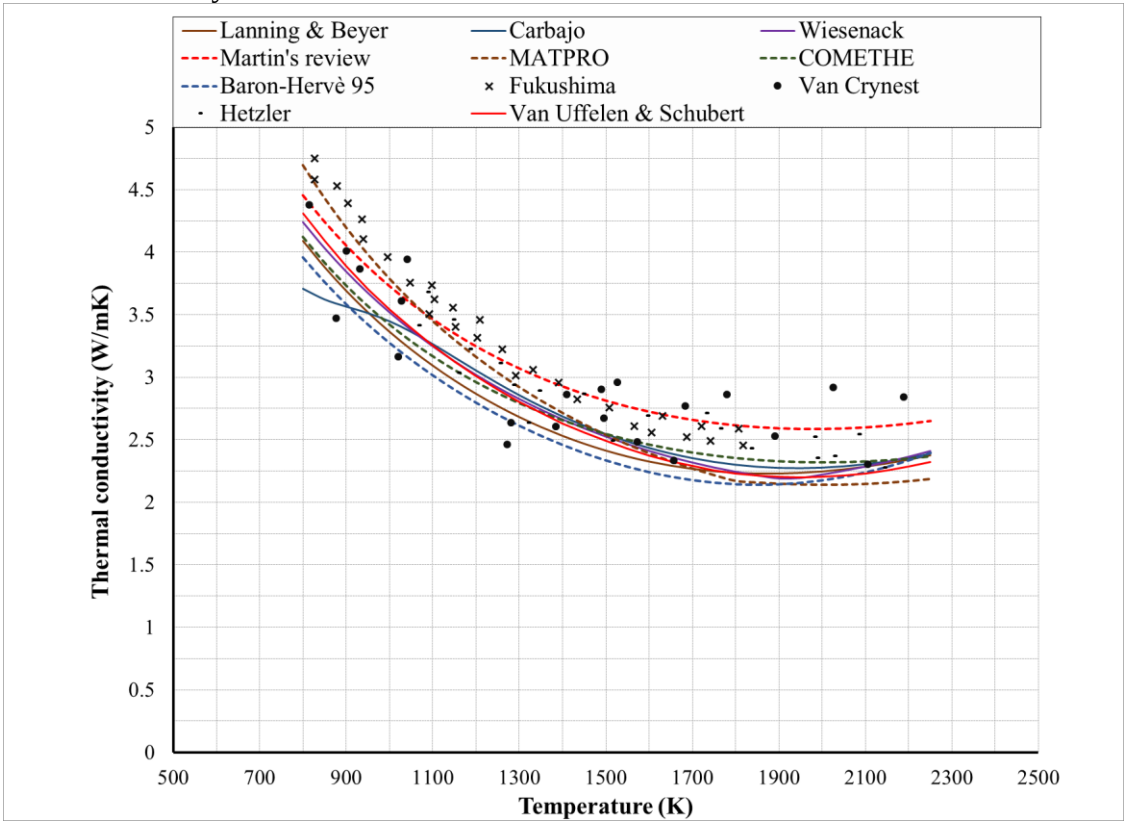

Figure 3-1 MOX thermal conductivity: comparison between correlations and experimental data for 100%TD, O/M=2, PU=20 wt.%.

2- Comparison at 95%TD, O/M=2, Pu= 20 wt.%

The correlations are compared with experimental data from three sources in *Figure 3-2*. The data from Van Crynest and Weilbacher have a large spread and spans the whole range of experimental data. A conclusion cannot be made based on their uncertainty. The data from Schemidt and Gibby are more accurate but are in opposite directions from each others. While Schemidt's data are higher than all the studied correlations, Gibby's data are lower than all of them. There is a preference given to Gibby's data for two reasons: the first is the larger number of data points and the wider range of temperature covered. The second comes from the fact that Wiesenack's correlation was designed for

UO_2 fuel then multiplied by a factor of 0.92 to fit it to MOX. The data from Schemidt then would predict a thermal conductivity of MOX that is equal to or even higher than UO_2 (*Figure 3-3*) which contradicts the fact that the conductivity of MOX is lower than that of UO_2.

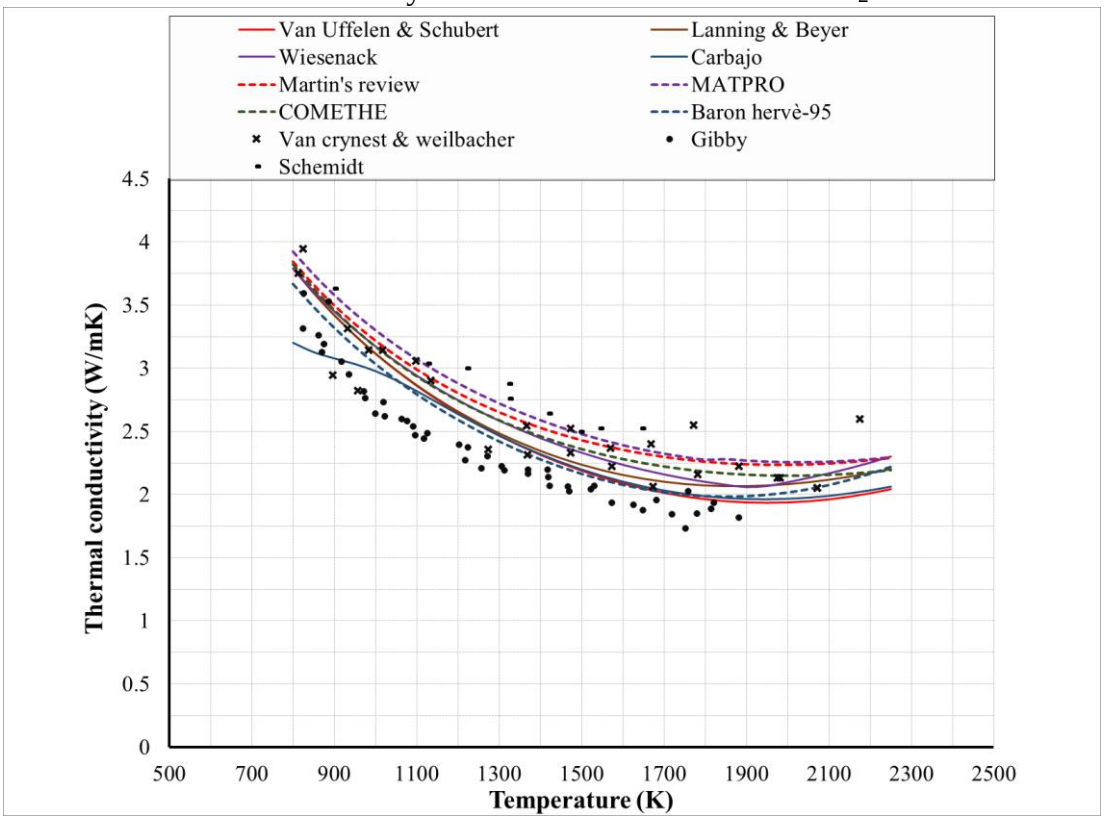

Figure 3-2 MOX thermal conductivity: comparison between correlations and experimental data for 95%TD, O/M=2, PU=20 wt.%.

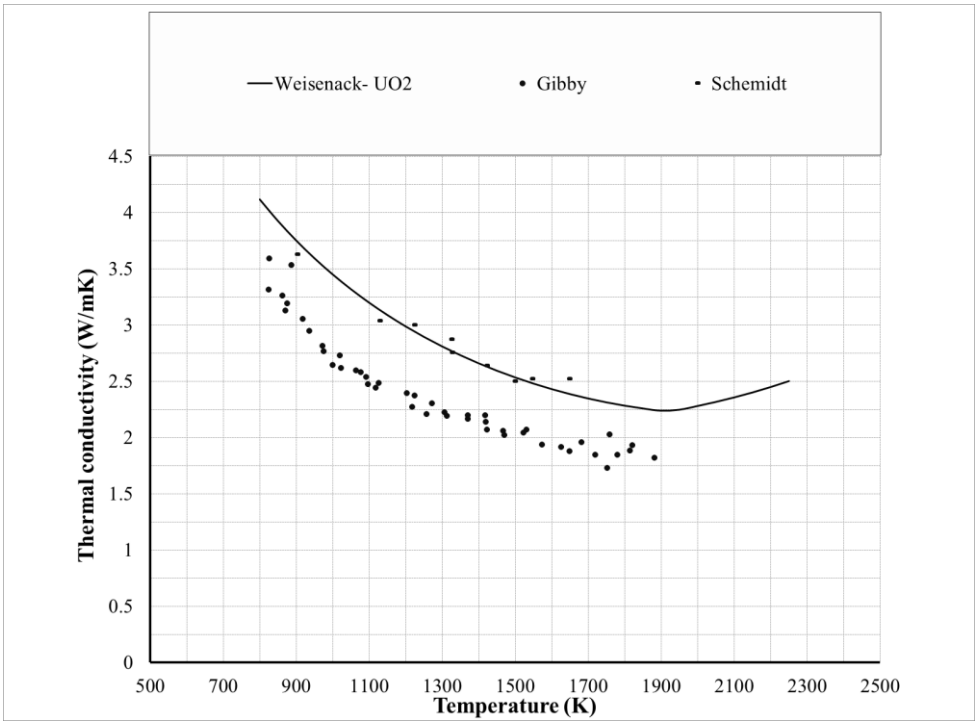

Figure 3-3 MOX thermal conductivity: comparison between Wiesenack correlation and experimental data for 95%TD, O/M=2, PU=20 wt.%.

3-Comparison at 95%TD, O/M=1.98, Pu= 20 wt.%

The correlations are compared with experimental data from three sources *Figure 3-4*. The included data are more precise than the previous cases and it can be noticed that the Baron-Hervè correlation has a good match with the data from Weilbacher and Gibby. Other correlations have a good match with the data from Bonnoret and weibacher data at higher temperatures. The TU correlations that do not take deviation from stoichiometry into account and Matpro correlation are higher than all the experimental data except for Van Uffelen and Schubert that matches the experimental data above 2000 K.

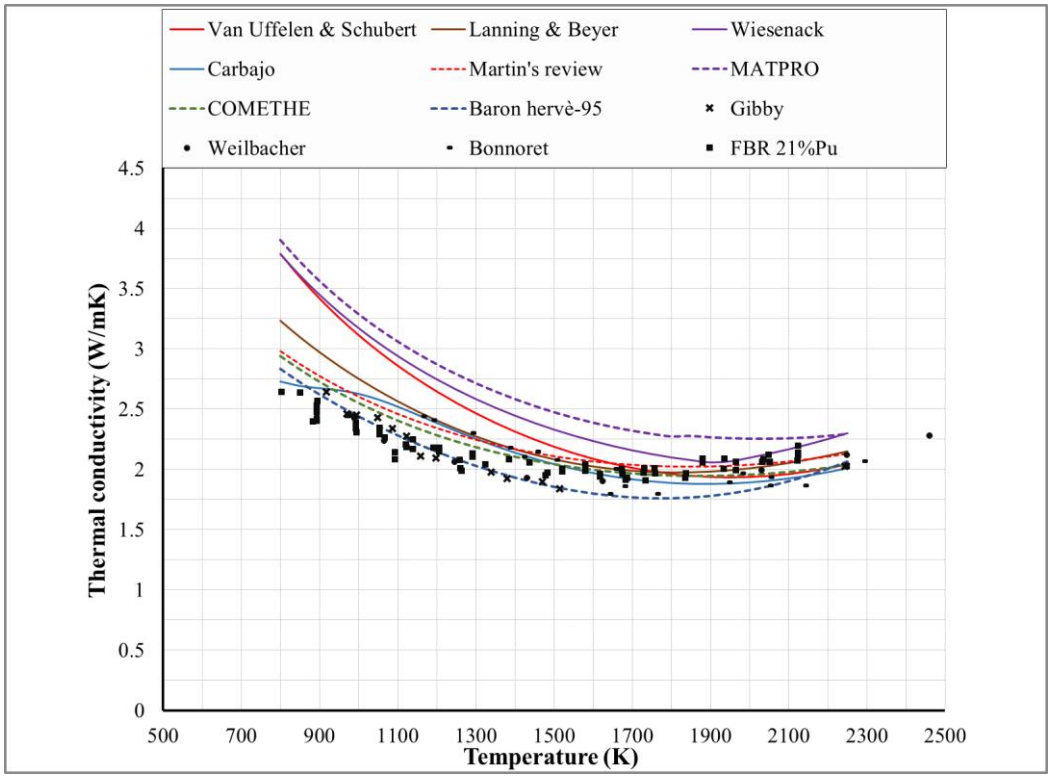

Figure 3-4 MOX thermal conductivity: comparison between correlations and experimental data for 95%TD, O/M=1.98, PU=20 wt.%.

4-Comparison at 95%TD, O/M=1.93, Pu= 20 wt.%

This is an extreme case and is reported here for clarifying the dependence of thermal conductivity on O/M ratio. A large deviation from stoichiometry leads to a drastic decrease in thermal conductivity as shown in *Figure 3-5*. It is clear that the correlations that do not take deviation from stoichiometry into account will fail to match the thermal conductivity measurements experimentally. The other correlations that take deviation from stoichiometry into account will generate a better prediction of the thermal conductivity. It is therefore visible that deviation from stoichiometry is an important factor that should be taken into account in any thermal conductivity correlation that aims to simulate non-stoichiometric fuel.

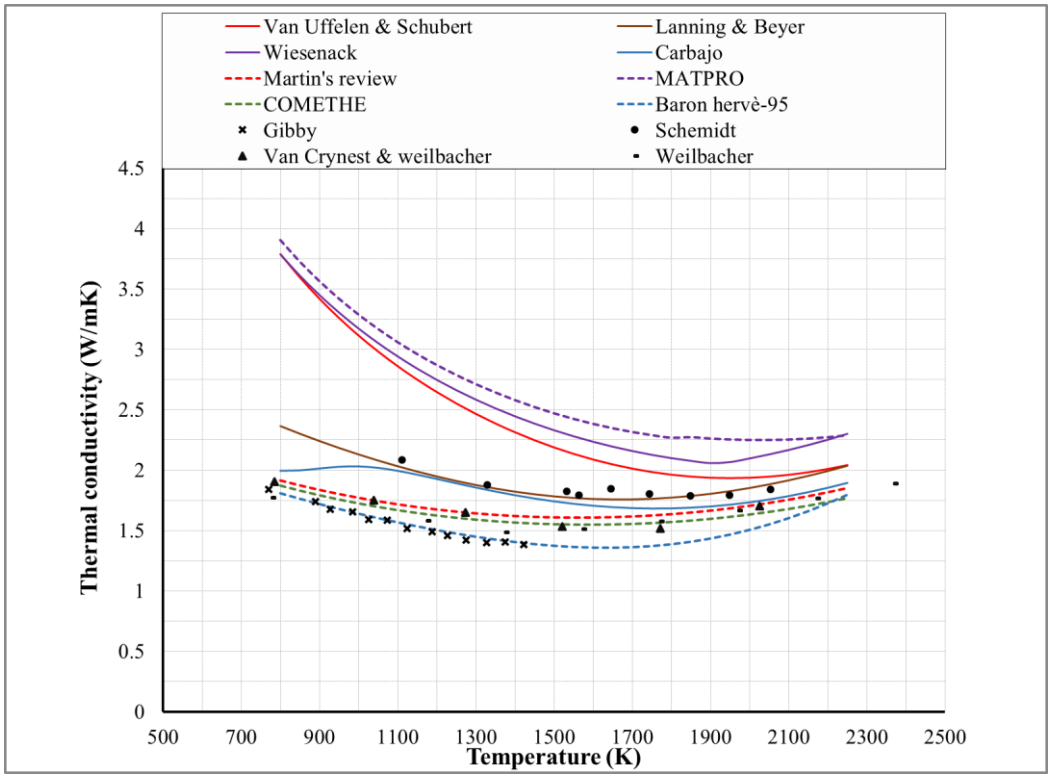

Figure 3-5 MOX thermal conductivity: comparison between correlations and experimental data for 95%TD, O/M=1.93, PU=20 wt.%.

5-Comparison at 95%TD, O/M=2, Pu= 6 wt.%

A comparison is made between the correlations and experimental data from Duriez and an industrial sample prepared used the MIMAS process (Micronized MAster blend). The process aims to producing soluble fuel that would be reprocessed to a final product that fulfills the requirements for LWR MOX fuel.[20] It can be seen (*Figure 3-6*) that TU thermal conductivity correlations fits well both the laboratory prepared sample of Duriez and the sample from industry. This gives an evidence of the ability of these correlations to predict the behavior of stoichiometric LWR MOX with low plutonium content. Open literature correlations seems to over-predict the thermal conductivity at lower plutonium contents except for Baron-Hervè correlation that is comparable to the samples data.

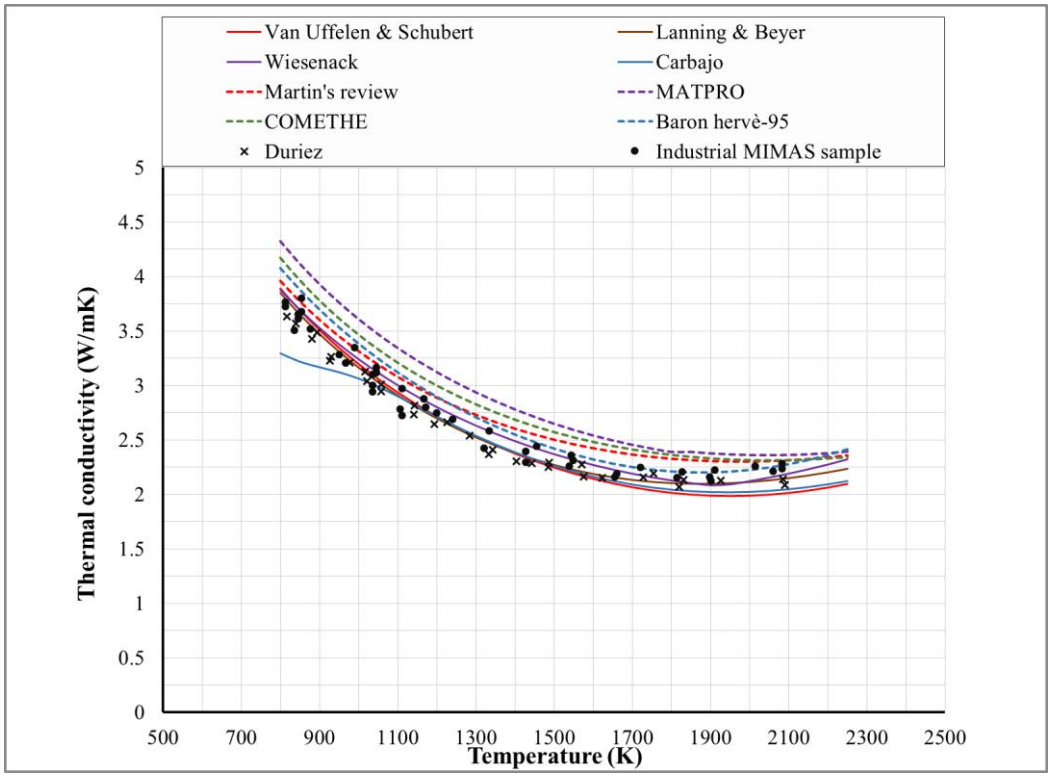

Figure 3-6 MOX thermal conductivity: comparison between correlations and experimental data for 95%TD, O/M=2, PU=6 wt.%.

3.4 Conclusive remarks

Thermal conductivity of MOX fuel is one of the parameters that govern the prediction of fuel temperature whose prediction is of great relevance to any integral fuel pin simulation. There are three mechanisms of heat conduction relevant to MOX; lattice, radiation and electronic conduction. Correlations used to predict thermal conductivity always consider lattice conduction and combine it with one of the two other mechanisms to predict the conduction at higher temperatures.
There are several parameters that govern the thermal conductivity. The main parameter is the temperature that is included in all correlations. In particular, thermal conductivity decreases with increasing the temperature up to 1500-1800 K then starts to increase again due to enhancement of conduction due to radiation or electronic conduction phenomena.

Other parameters such as (Burn-up, deviation from stoichiometry, Pu content) may or may not be included in a correlation and they vary in their importance. Therefore, it is important to investigate how critical it is not to include a certain parameter and how the correlations with different parameters deviate from each others:

Porosity obviously degrades the thermal conductivity.
Thermal conductivity always decreases with deviation from stoichiometry.
Thermal conductivity degrades with burn-up.
Increasing Pu content leads to a decrease in thermal conductivity.

It is important to note that thermal conductivity is more sensitive to all the investigated parameters at lower temperatures. As the temperature increases, the degradation of thermal conductivity is less sensitive to the variation of the studied parameters.

The TU code includes four correlations that are used to predict the MOX fuel conductivity. They all account for temperature, porosity and burn-up as parameters. Two of them include deviation from stoichiometry. The correlations of TU do not include Plutonium content.

Four other open literature correlations were investigated and compared with the ones from TU. They do not include burn-up as a factor but three of them include the plutonium content parameter. All of the open literature correlations include the deviation from stoichiometry, porosity and temperature as factors.
Comparing the correlations from both sources together gives some inferences related to their sensitivity to various parameters. At stoichiometric conditions the correlations deviate from each other, especially in the low temperature zone. This is due to the different data on which the correlations are based and the different parameters and their weighted effect in total.
As the deviation from stoichiometry increases, the variation increases between the two TU correlations that do not include deviation from stoichiometry and all the other correlations. The thermal conductivity is much less sensitive to variation in Pu content.
In order to confirm the results of the comparison between the correlations, experimental data were collected at different levels for each of the parameters. The role of experimental data is to judge which correlation predicts the variability with a certain parameter accurately. This was done for all the parameters except for burn-up due to non-possession of thermal conductivity data for MOX fuel at burn-up higher than zero.

The comparison confirmed the importance of deviation from stoichiometry. The correlations that do not include it will introduce a significant error if used for hypostoichiometric fuel. To sum up, a thermal conductivity correlation should include burn-up and deviation from stoichiometry which are important parameters to be included. Pu content is not that significant and could be neglected without critical errors. Porosity is taken into account as a correction factor with many formulae. Thermal conductivity at higher temperature is preferred to be modelled by electronic conduction mechanism but there is not enough data to prove it experimentally.

4 TRANSURANUS code

TRANSURANUS is a code developed by the institute of Transuranium elements to be used for the thermal and mechanical analysis of nuclear fuel rods.[11][13] The code includes a lot of physical models and numerical algorithms to predict the thermal and mechanical properties of the fuel rods and their effects on each other. In the next subsections, some details related to thermal, mechanical, and burn-up modelling by the code are extracted from the code's manual for illustration purposes.[11] The code is a quasi 2D model which relies basically on the concept of superposition of 1D radial and axial analysis. The physical phenomena modelled are covered by many available models for different materials used in fuel, cladding and structure material of the rod that are valid over the various operation conditions of the rods and different time range of the states in which the rod exists from milliseconds to years. The code can be used for both deterministic and probabilistic analyses.
The choice of the desired models of the different materials is fed to the code by the usage of an input file that dictates to the code the kind of analysis to be done (deterministic or probabilistic), the reactor type, fuel and cladding types and the details of their construction parameters on the macro and micro scales. It also informs the code whether structure materials are modelled or not, the numerical algorithms to be used and the time steps and the boundary conditions of the modelled situation etc. The results of the analysis are then stored in output subroutines that can be summoned both numerically and visually using a plotting tool as a function of time for discrete axial locations in the rod or as integral values, a function of axial position of the rod, or as a function of radius at different axial positions.

The *capabilities* of the TRANSURANUS code can be summarised as follows:

- Analysis of all fuel rod types under normal, off-normal and accident conditions (deterministic and probabilistic) is in principle possible.
- Consistent steady-state and transient analysis.
- Clearly defined mechanical-mathematical framework into which physical models can easily be incorporated.
- Fast and reliable.
- Database, models and code extensively verified.
- Applied by different groups and different licensing authorities.

4.1 Thermal Analysis

The main purpose of the thermal analysis is to be able to predict the temperature profile in the fuel rod and cladding. The accurate prediction of the temperature profile is of critical importance since it affects a lot of thermally dependent phenomena in the fuel rod (FGR, thermal expansion, restructuring creep, etc.). This analysis involves a lot of complexities and non-linearities and can be only solved numerically. Finite difference methods are basically used by TU for the thermal analysis with the occasional usage of finite element methods. A combination of both methods is the key to obtaining an extremely accurate solution. The methods used can be explicit, implicit or Crank-Nicholson schemes. The usage of Crank Nicholson scheme is a standard method for the transient analysis. Special models are used to predict the gap conductivity between fuel and cladding and the heat transfer coefficients in cracks inside the fuel. Melting, boiling, and phase changes of the rod materials are predicted by the code as well.

4.1.1 Basic Equations

Thermal analysis is performed using one-dimensional radial and axial energy conservation equations. The heat conduction equation for the fuel and the cladding is given by:

$$c\rho\partial\vartheta/\partial t = 1/r\ \partial/\partial r\ (\lambda r\ \partial\vartheta/\partial r) + q'''$$

where:
$c = c\ (t, r)$ = specific heat at constant pressure
$q''' = q'''\ (t, r)$ = power density
$r = r\ (t)$ = radius
t = time
$\vartheta = \vartheta\ (t, r)$ = temperature
$\lambda = \lambda\ (t, r)$ = thermal conductivity
$\rho = \rho\ (t, r)$ = density

and the energy equation for the coolant can be written in the form:

$$\partial(A\rho e)/\partial t + \partial(A\rho ew)/\partial z = -A\rho gw + Aq''' + 2\pi r_{cl,o}\, q''_{cl,c} - 2\pi r_{s,i}\, q''_{c,s} - A\partial(pw)/\partial z + \Sigma(s^i e^i) \quad \text{Eq. 4-1}$$

where:
$A = A\ (t, z)$ = area of coolant channel
$\rho = \rho\ (t, z)$ = density of coolant
$e = e\ (t, z)$ = total energy per unit mass
t = time
$w = w\ (t, z)$ = velocity of coolant
z = axial
$g = g\ (t, z)$ = gravitation constant
$q''' = q'''\ (t, z)$ = power density in coolant
$q'' = q''\ (t, z)$ = heat flux
$r = r\ (t, z)$ = radius
$p = p\ (t, z)$ = pressure of coolant
$s = s\ (t,z)$ = source terms
cl,o = cladding, outer
cl,c = cladding to coolant
c,s = coolant to structure
s,i = structure, inner

4.1.2 Boundary Conditions

The analysis can involve one of the following cases:

- Analysis of fuel
- Analysis of fuel and cladding
- Analysis of fuel, cladding and coolant
- Analysis of fuel, cladding, coolant and structure

For the coolant, two options are available:

- The coolant temperature is prescribed as a function of the axial distance and time.
- The coolant temperature is calculated based on a prescribed coolant inlet temperature and mass flow rate which may depend on the axial distance and time.

For the solids, fuel, cladding and structures the following conditions are available:

- Temperature (*Dirichlet condition*) – standard option for outer surface.
- Heat flux density (*Neumann condition*) – standard option for the inner surface (heat flux density is 0)

4.1.3 Heat transfer

Coolant

In general three regimes must be covered in a LWR:

- Sub-cooled regime, where only surface boiling occurs. This regime is typical for PWR's under normal operating conditions.
- Saturated, two phase regime. This regime is typical for BWR's under normal operating conditions.
- Saturated or overheated regime. This regime may be reached in all off-normal situations. A typical example is a LOCA.

Different types of coolant flow channels with different hydraulic diameters in a fuel assembly are considered:

- "normal" sub-channels inside the regular lattice (quadratic or hexagonal)
- those surrounding the control rod guide tubes
- those between adjacent assemblies in the core
- the corner rods of the fuel assemblies

Cladding

The heat transfer coefficient between fuel pellets and cladding depends on:

- gap width or contact pressure between fuel and cladding;
- gas pressure and composition;
- surface characteristics of cladding and fuel.

$$h_{gap} = h_{rod} + h_{con} + h_{gas} \qquad \textit{Eq. 4-2}$$

Fuel pellet

$$\rho c\, \partial T/\partial t = (1/r)\, \partial(\lambda r\, \partial T/\partial r)/\partial r + q''' \qquad \textit{Eq. 4-3}$$

inner boundary $\partial T/\partial r = 0$
outer boundary $\Delta T_{gap} = q'''/h_{gap}$

The temperature distribution in the pellets is affected by two terms:

- the heat source
- the fuel thermal conductivity.

4.2 Mechanical analysis

The main purpose of the mechanical analysis is to calculate the stresses and strains and the resultant deformations in the considered geometry.

In order to derive an adequate solution, the following assumptions are made:

- The geometric problem is confined to one-dimensional, plane and axisymmetric idealisation, i.e. the axial deformation is constant across the radius (modified plane strain condition).
- Although the fuel and cladding move axially (not necessarily at the same rate), planes perpendicular to the z-axis remain plane during deformation (plain strain condition), i.e. the rod remains cylindrical.
- Dynamic forces are in general not treated, and the time dependence inherent in the analysis (creep) is handled incrementally.
- The elastic constants E (Young's modulus of elasticity) and υ (Poisson ratio) are isotropic and constant within a cylindrical ring.
- The total strain can be written as the sum of elastic and non-elastic components.

The first two assumptions reduce the problem to one dimension. The third assumption indicates that the stresses are related through a local equilibrium condition for the radial force in the following form:

$$\partial\sigma_r/\partial R = (\sigma_t - \sigma_r)/R \qquad \textit{Eq. 4-4}$$

Based on the fifth assumption, the constitutive relations read:

$$\underline{\varepsilon}^{tot} = \underline{\varepsilon}^{elastic} + \underline{\varepsilon}^{non\text{-}elastic} \qquad \textit{Eq. 4-5}$$

$$\underline{\varepsilon} = [\varepsilon_r, \varepsilon_t, \varepsilon_a]$$

$$\varepsilon_r = [\sigma_r - \nu(\sigma_t + \sigma_a)]/E$$

$$\varepsilon_t = [\sigma_t - \nu(\sigma_r + \sigma_a)]/E$$

$$\varepsilon_a = [\sigma_a - \nu(\sigma_r + \sigma_t)]/E$$

Strains are divided into two categories as follows:

The elastic strains for an isotropic material are reversible
Non elastic strains consists of various contributions:

- Thermal strain
- Swelling
- Plasticity and creep
- Pellet cracking

4.2.1 Boundary conditions

Radial boundary conditions
The coolant pressure is the factor determining the stresses at the outer surface of the cladding. The radial boundary conditions in the fuel depends on the gap closure conditions. If the gap between the fuel and the cladding is open (no pellet cladding mechanical interaction), the fill gas pressure determines the radial stresses on the fuel periphery. At the center of the fuel, the geometrical condition of the fuel controls the stresses. If the pellets are hollow then the stresses are related to the fill gas pressure, while for fully cylindrical pins, the radial and tangential stresses are equal at the center of

the pellet. If the gap is closed then the contact pressure between the fuel and the cladding determines the boundary conditions at the periphery of the pellet while the other boundary conditions remains the same.

Axial boundary conditions

The axial strain is assumed to be constant in the plane perpendicular to the axial axis and is determined by the axial force balance. The friction forces depends on the PCMI and can be only taken into consideration iteratively. Even if the fuel and cladding are in contact with no gap in between them, they are not treated as a single body since there might be some sliding above or below. When a section is being analysed numerically, it is not known whether the friction forces originate from the slice above or the one below. The different modes of interaction between fuel and cladding can be seen in *Figure 4-1*. Some parts of the fuel rod slice may be trapped in between the slices and higher axial forces originate and act on the both the fuel and the cladding.

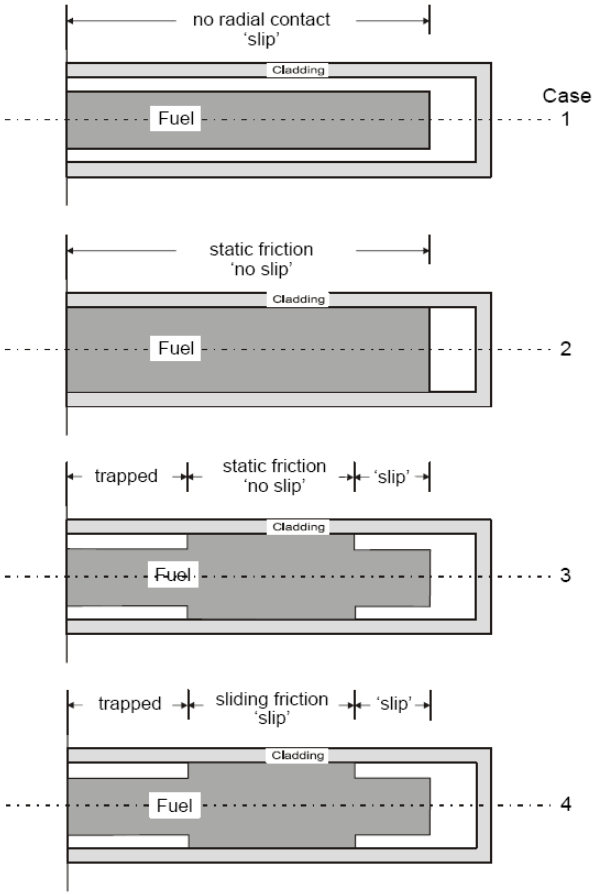

Figure 4-1 Four possible modes of an interaction between fuel and cladding. [11]

4.3 Burn-up Equations

Many of the thermal and mechanical characteristics of fuel rods depends on the burn-up conditions within the fuel rod. Therefore, it is important to correctly calculate the changes occurring in the fuel rod structure and the conditions due to burn-up before tackling the thermal and mechanical behaviour of the fuel rod at a certain time step.

It is crucial to calculate the following at each radial/axial position in the fuel:

- the fraction of fissile material burnt (local burn-up),
- the conversion of ^{238}U-238 to ^{239}Pu and the subsequent build-up and fission of the higher Pu isotopes,
- the build-up of fission products.

The radial power density is determined from the radial distribution of the fissile materials. After which the radial burn-up is determined, based upon which, the fission products radial distribution is obtained. Burn-up is given as a rod averaged burn-up or as an average for a certain slice in the fuel rod. In TRANSURANUS, two burn-up models are available:
1. the RADAR model.
2. the TRANSURANUS burn-up model TUBRNP.

4.3.1 The RADAR model

The RADAR model ("RAting Depression Analysis Routine") can be used for LWR and HWR conditions since the characteristic reactor quantities are given as input data. The most remarkable disadvantage of the model is that it neglects the formation of Plutonium isotopes heavier than ^{239}Pu. The main equations of the RADAR model are:

- a differential equation for the ^{235}U concentration
- a differential equation for the ^{239}Pu concentration
- the solution of simple diffusion theory for the thermal flux.

The absorption of neutrons in ^{238}U near the periphery of the pellet enhances the production of plutonium near the surface. The radial distribution of the plutonium is determined according to an empirical function.

4.3.2 The TRANSURANUS-LWR Burn-up Model

The TRANSURANUS-LWR burn-up model equations are based on the concept of *one group, spectrum-averaged cross-sections*. The radial distribution of plutonium is obtained also from an empirical function. The basic equations for the model are:

$$\partial N_{235}/\partial bu = -\sigma_{a,235}\, N_{235}\, A \qquad \textit{Eq. 4-6}$$

$$\partial N_{238}/\partial bu = -\sigma_{a,238}\, N_{238}\, f(r)\, A \qquad \textit{Eq. 4-7}$$

$$\partial N_{239}/\partial bu = -\sigma_{a,239}\, N_{239}\, A + \sigma_{c,238}\, N_{238}\, f(r)\, A \qquad \textit{Eq. 4-8}$$

$$\partial N_{j}/\partial bu = -\sigma_{a,j}\, N_{j}\, A + \sigma_{c,j-1}\, N_{j-1}\, A \qquad \textit{Eq. 4-9}$$

The radial power density profile is updated based on the average burn-up increment. The determination of the radial burn-up is done based on the new radial power density profile, after which the fission products concentrations are updated depending on their fission yields.

5 Analysis of LWR MOX: IFA-597 experiment

5.1 Description of the experiment

5.1.1 Background and objective of the experiment

Within the scope of the current work, it is important to give a brief description of IFA-597.4/.5/.6/.7. There were different stages of irradiation that were done in Halden reactor between July 1997 to January 2002. The experiment involved the irradiation of two MOX rods. One is a solid rod with four annular pellets on top to allow the accommodation of fuel center thermocouples. The other rod was a complete hollow pellets rod. Along with the thermocouples used to measure the centerline temperature, pressure bellows transducers were instrumented to provide data of the pressure along the time span of the experiment.[2]

The main purpose of IFA-597.4/.6 was to study the thermal behavior of MOX including fission gas release mechanisms (FGR) when subjected to normal operation. This was done in a single cluster rig that contained both rods. Subjecting them to the same conditions allowed the investigation of the different behavior of FGR of both kinds of rods. Deliberate power uprating was done in order to cause opening in the interlinkage at the grain boundaries of the fuel lattice. That would lead to significant gas release through these interlinked tunnels. This was done at 10 MWD/kg MOX for IFA-597.4 and at 22.27 MWD/kg MOX for IFA-597.6.

In IFA-597./5./7, the objective was to accumulate fission gases in the matrix; Hence FGR was to be avoided. In order to avoid FGR, the rig was shifted outwards in the core to reduce the power. Several UO_2 rods that were irradiated up to 13 MWD/kg UO_2 in IFA-597.1 were added to the rig along with the MOX rods. Four UO_2 rods were added in IFA-597.5. Three rods were used in IFA-597.7 to restrict FGRs. During IFA.-597.5/.7 the power level was maintained low in the MOX rods and no significant FGR was noticed.

Since the FGR during IFA-597./6 was higher than expected and could not be explained, it was decided that IFA-597.7 should be unloaded. The experiment stopped in January 2002. The focus in this report is on IFA-495.4./5 because of the unexpected behavior in IFA-597.6 and the termination of IFA-597.7

5.1.2 Halden Boiling Water Reactor (HBWR)

HBWR is a reactor located in Halden in the south of Norway near its borders with Sweden.[21] The reactor is a natural circulation heavy boiling water reactor. The maximum power of the reactor is 25 MW (thermal). Water temperature is 240°C pressurized to 33.3 bar. The reactor vessel primary circuit system dwells inside a rock cavern that is 30-60 m thick with a net volume of 4500 m^3. The reactor pressure vessel is made of carbon steel and is cylindrically shaped. The round shaped bottom and the cylindrical portion are cladded with stainless steel. A schematic diagram of the reactor, pressure vessel and operation data can be seen in *Figure 5-1*.

The Halden Boiling Water Reactor[21][22] is currently operated at 18 to 20 MW. The reactor has operated since 1959. Initially, the aim of the project was to investigate nuclear energy's capability as a supplier of steam to the wood pulp industry. The reactor facilities have then been subjected to a huge development until it became one of the most versatile in the world. Through these developments, around 300 in-pile experiment took place on different levels of complexities and purposes.
The flat reactor lid has individual penetrations for fuel assemblies, control stations and experimental equipment. Heavy water is used as a coolant, moderator and reflector with a total stock of 14 tons. A mixture of steam and water flows from the bottom going upwards by natural circulation through the

shroud tubes around the reactor core. When water reaches the top, its flow is then reversed and flows downwards. The steam is collected in the space above the water. Water then re-enters to the fuel assemblies through holes in the lower end of the core shroud. The steam continues its flow outside of the pressure vessel to two main steam generators. In that system heat is transferred to a secondary circuit containing light water. After this process, the steam condensate returns to the reactor by gravity.

On the secondary side of the circuit, two circulation pumps are used to drive the water through the steam transformers, a steam drum, and a steam generator where steam is produced in the tertiary circuit. This steam is considered as process steam and delivered to a paper mill with the capability of draining it to a nearby river. The facility has also high pressure loops with light water provided for testing under prototypic BWR and PWR conditions. In order to provide experimental variation of void fraction in the assemblies an external sub cooler loop is installed. The central location of the core is occupied by the emergency core cooling tubes.[23]

The source of the fuel charge is test fuel from participant organizations in member countries of the reactor project and a driver fuel assemblies used for providing reactivity needed for operation purposes. The core consists of 110-120 fuel assemblies. The test fuel is located in an open hexagonal lattice with a pitch 130 mm (Figure 5-2). The maximum height of the fuel section is 1710 mm. Currently, driver fuel assemblies consist of eight to nine fuel rods with 6% enrichment. The standards and specifications and main parameters of the facility are included in Table 5-1

Assembly	**Unit**	**Quantity**
Shroud material	--	Zr-2
Shroud ID	mm	71
Shroud thickness	mm	1
Number of rods per assembly	--	8
Pitch circle diameter	mm	50
Length from lowest pellet in lower rod to highest pellet in upper rod	mm	810
Fuel material	--	UO2
Fuel enrichment	%	6
Pellet density	g/cm3	10.52
Pellet OD	mm	10.49
Pellet height	mm	8.6-10.8
Length of natural fuel per rod	mm	12
Active length	mm	748-811
Cladding material	--	Zr-2, Zr-4
Cladding ID	mm	10.67
Cladding wall thickness	mm	0.8
Nominal gap	mm	0.16-0.18

Table 5-1 HBWR, summary of the driver fuel main data.

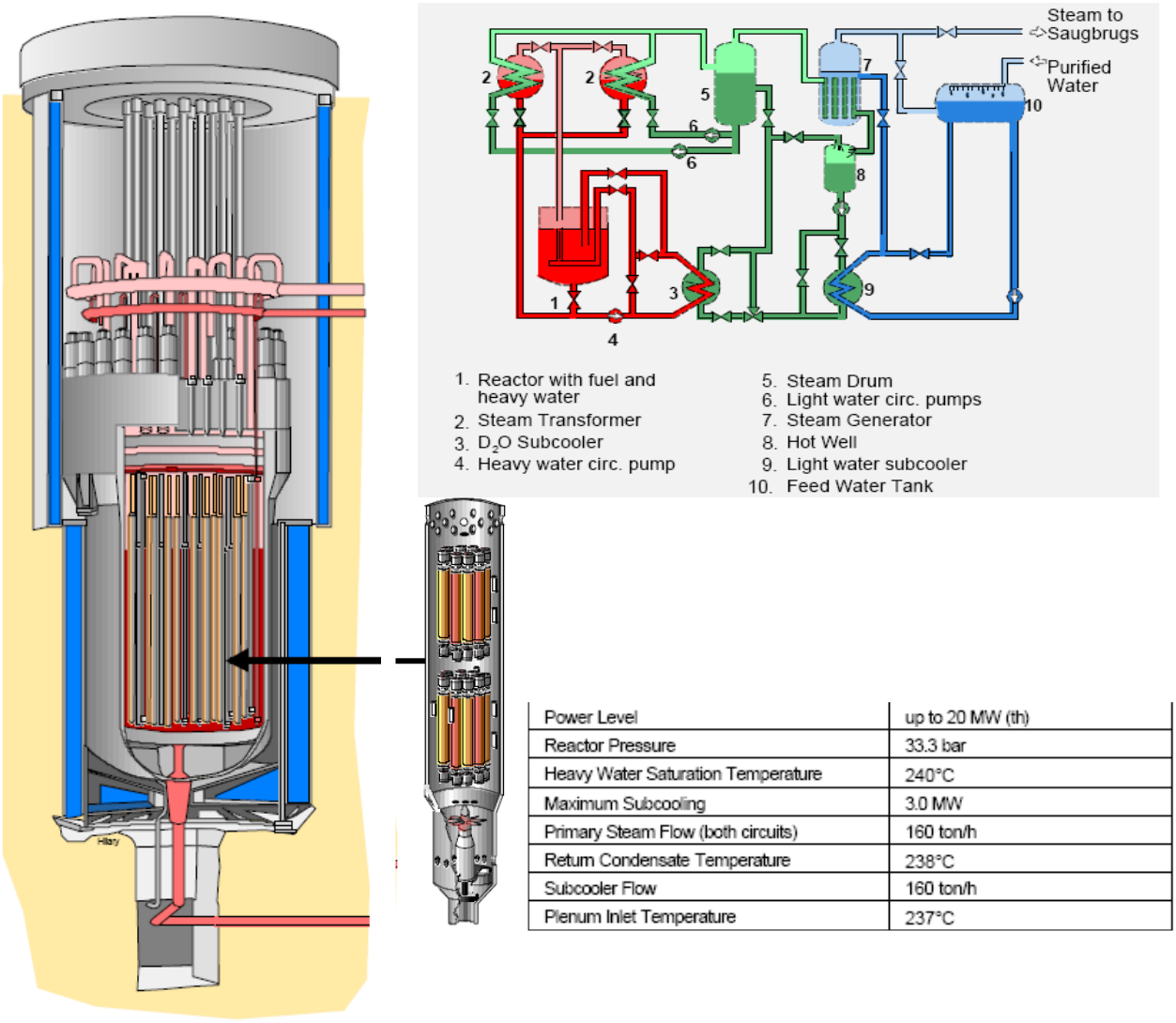

Power Level	up to 20 MW (th)
Reactor Pressure	33.3 bar
Heavy Water Saturation Temperature	240°C
Maximum Subcooling	3.0 MW
Primary Steam Flow (both circuits)	160 ton/h
Return Condensate Temperature	238°C
Subcooler Flow	160 ton/h
Plenum Inlet Temperature	237°C

Figure 5-1 HBWR, schematic diagram and main operation parameters. [21]

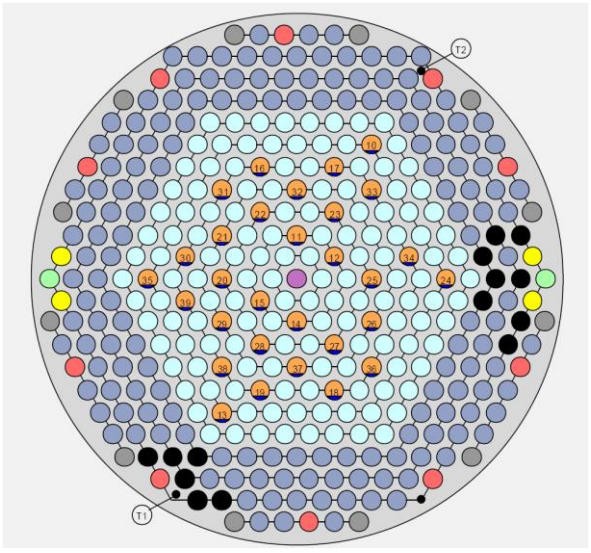

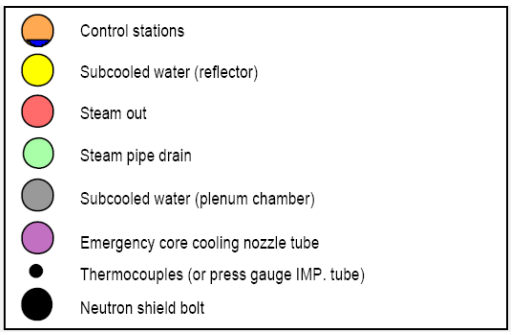

Number of Fuel Assembly	110
Number of Control Stations	30
Core height – usable length for placing fuel -	1710 mm
Configuration	open hexagonal lattice
Lattice Pitch	130 mm
Reflector Top: thickness	300 mm
Reflector Bottom: thickness	380 mm

Figure 5-2 HBWR, plan view of the reactor top lid and main parameters.[21]

5.1.3 Design of the rig and rods

In *Figure 5-3*, a schematic of the testing rig can be seen. The rig had one cluster that contained the MOX fuel and the power suppressing UO_2 when needed. The rig contained four Vanadium neutron detectors and three water coolant thermocouples. Two of those thermocouples were located at the outlet and one at the inlet. In core connectors for the instrument cables are placed at the top and bottom of each rod position.[2]

The rig operated in IFA-597.4 has power levels between 20-35 kW/m to release fission gases. It was relocated to an outer position later in IFA-597.5 to assure lower LHR and avoiding FGR. Then in IFA-597.6 it was relocated inwards again for the same reason as in IFA-597.4

The solid and hollow MOX rods named as rod 10 and rod 11 respectively were irradiated in IFA-597.4 as fresh rods with initial total Pu content of 8.44%, and 6.07% fissile Plutonium content. Manufacturing parameters of the rods are summarized in *Table 5-2* along with data of the UO_2 that were used in the experiment. Rod 10 is 224 mm height consisting of 17 solid fuel pellet and on top of them 4 hollow pellets in which the centerline thermocouple was accommodated. Rod 11 is 220 mm height consisting of 21 pellets all of them are hollow. The initial outer diameter of the pellets is 8.04 mm and the hollow pellets had an initial center hole diameter of 1.8 mm. Cladding outer diameter is 9.5 mm with a gap of 180 μm of width. The pressure bellow transducers were located at the bottom. The bellows were initially pressurized to 4 bar. The rods were pressurized with Helium to 5 bar at 20^0C.

	Rod 10	**Rod 11**	**Rod 1**	**Rod 2**	**Rod 3**	**Rod 5**
Fuel						
Fuel type	MIMAS-MOX	MIMAS-MOX	UO_2	UO_2	UO_2	UO_2
Active fuel length (mm)	224	220	503	502	499	502
Fuel mass (Kg)	0.1179	0.1106	0.404	0.415	0.419	0.432
Instrumentation upper end	TF1	TF2	-	-	-	-
Instrumentation lower end	PF2	PF5	-	EC3	EC4	-
Fuel density (g/cc)	10.54	←	10.55	←	←	←
Initial fuel enrichment (wt%)	6.07 Pu(f)	←	4.95 ^{235}U	←	←	←
Initial fuel diameter (mm)	8.04	←	10.25	←	10.45	100.58
Diam clearance (mm)	0.18	←	0.4		0.2	0.07
Pellet length (mm)	10.7	10.5	8.2	8.4	8.5	8.4
Pellet form (not including end pellets)	17 solid, 4 hollow	21 hollow	61 hollow	50 solid, 10 hollow	59 hollow	60 hollow
Drilled center hole diameter (mm)	1.8	←	1.9	←	←	←
Dishing	Both ends	←	Top end	←	←	←
Dishing depth (mm)	0.26	←	0.75	←	←	←
Rod						
Cladding material	Zr-4	←	Zr-2	←	←	←
Filler gas pressure (bar)	5 (He)	←	←	←	←	←
Cladding OD (mm)	9.5	←	12.25	←	←	←
Cladding thickness (mm)	0.64	←	0.8	←	←	←
Free volume (cc)	4.5	4.9	9.6	9.8	8.2	8.9

Table 5-2 IFA-597 experiment, rod characteristics.

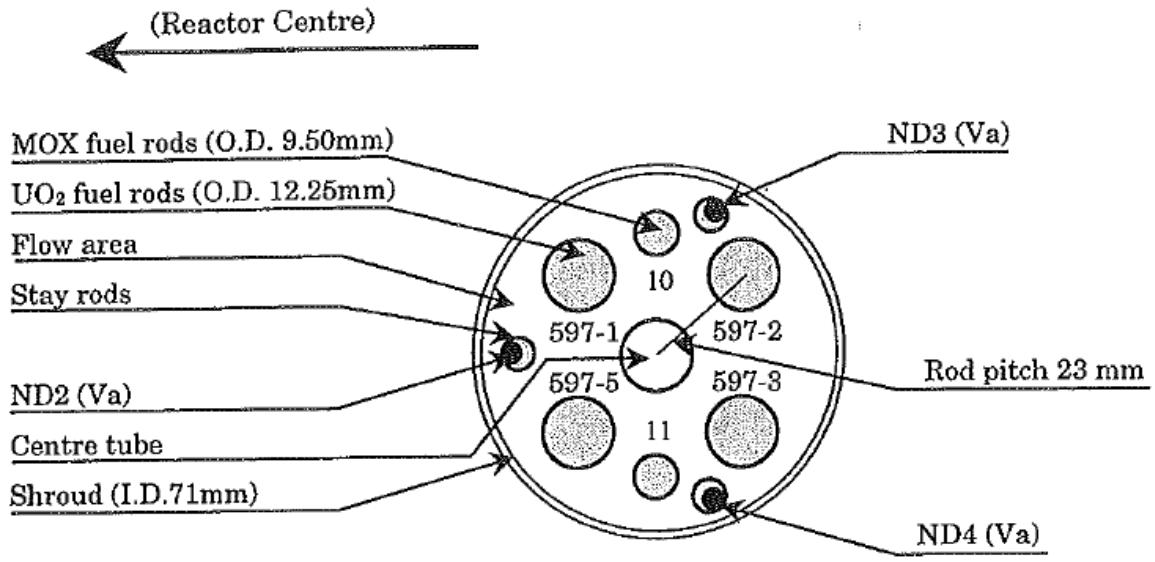

Figure 5-3 IFA-597 experiment, schematic radial view of the test rig. [2]

5.1.4 Linear Heat rating (LHR)

The location of the rig in the reactor and the small height of the rods led to a maximum to average heat rating in the rods almost equal to unity. Therefor the local LHR at the thermocouple position was almost the same as the average LHR in both rods. The LHR is more uniform for rod 11 with a variation less than 2% relative to 7% variation from average for rod 10. The plan of the experiment was to have power uprating every 10 MWD/kg MOX to study FGRs.

The linear heat rating begins in the first half of IFA-597.4 in the range of 30-35 kW/m and in the range of 27-30 kW/m in the second half of the experiment. During the experiment several occasional gas releases occurred. For IFA-597.5 the rods were relocated to a lower LHR location with the addition of four UO_2 rods to suppress the LHR of the MOX rods. No FGR was noticed because of the decrease of LHR to a range between 8-17 kW/m. In IFA-597.6 the heat rating was increased again to a level in the range of 20-24 kW/m. The average LHR in rod 10 was higher than rod 11. The maximum LHR was always located almost in the middle of the rods. There is an uncertainty level of 5% in the power level. This is generated from the calorimetric power calibration done at the beginning of each experiment done in HBWR for IFA rods. The uncertainty of this process is 5%. After the start of the experiment, repeating this process is not always possible. Thermal power level of the rods is then determined by neutronic simulations using the HELIOS code. The estimated error is expected to increase from 5% to 10% at the end of the experiment. In this study, the uncertainty in LHR will be considered only to be the initial 5% as shown in *Figure 5-4*

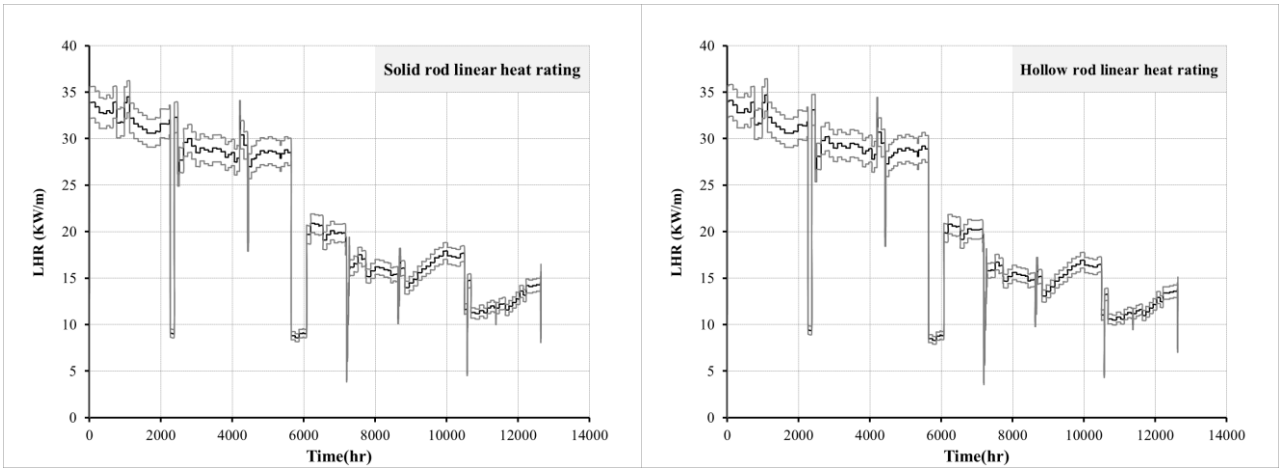

Figure 5-4 Linear heat rating of solid and hollow rods.

5.2 Modelling IFA597.4/.5 with TU

5.2.1 Development of TU input file

The fuel rods are modelled using TRANSURANUS code, version "v1m1j12", with the deterministic option, steady state thermal and mechanical analysis. The version of the manual is "v1m1j12"[11]. The boundary conditions were prepared using a Fortran-90 program prepared by the author.

The input decks are prepared according to the information available in the manual of the code. Most of the models used in the reference analysis were the standard recommended models by the code developers. Some deviations occurred when needed e.g. the usage of UO_2 models for the MOX fuel swelling because the MOX models available in the code are still under investigation and not totally validated. *Table 5-3* summarizes the options that have been selected and that are expected to affect the prediction of the fuel temperature.

IFA-597 Reference input decks			
Parameter	**Reference Option**	**Description**	**Other options**
Fuel conductivity	Correlation 31 (recommended)	Standard correlation of the thermal conductivity of MOX fuel (best estimate) according to Van Uffelen and Schubert, based on experimental data obtained by Duriez et al for fresh MOX fuel and laser flash measurements of irradiated MOX fuel at ITU. It is extended by an ambipolar term recommended by Ronchi et al.	32,33,34,35
Fuel swelling	Correlation 20	Developed by K. Lassmann from correlation 19. The gaseous swelling contribution was modified and integrated from the steady state equation considering the local contributions of the burn-up, the temperature, the stress and the diffusion coefficient.	18, 19, 21,25, 3, 11, 12, 13
Pellet fragment relocation	Model ireloc 8	Modified FRAPCON-3 model. It considers the as fabricated gap size, the burn-up and the linear heat rate.	2, 3, 4, 5, 6

Fuel grain growth	Model igrnsz 1 (recommended)	Grain growth model of Ainscough and Olsen. It computes the grain radius increase as function of the fuel local temperature assuming a maximum grain radius for each temperature.	--
Fuel densification	Model idensi 2 (recommended)	Empirical model for LWR and FBR. This model needs the input of the minimum porosity DENPOR at the end of thermal and irradiation induced densification and the time constant DENBUP (burn-up in MWd/tU, at which irradiation induced densification is terminated).	3, 7
Gap conductivity	Model ihgap 0 (recommended)	Standard Option: gas Bonding thermal conductivity of mixture according to Lindsay and Bromley. Accommodation coefficients are taken into account	1, 3, 4, 5
Fission gas release	Models: fgrmod6 (recommended), igrbdm3, Idifsolv0	FGRMOD 6: URGAS algorithm with the diffusion coefficients of Hj. Matzke (thermal) and a constant athermal diffusion coefficient. IGRBDM 3: New model developed according to modified Koo model for ramps simulations. IDIFSOLV 0: Diffusion equation is solved by the URGAS-algorithm.	Fgrmod: 4,9 Igrbdm: 0, 1, 2 Idifsov: 1, 2, 3 4,5,6

Table 5-3 IFA-597 experiment, summary of models and correlations that might affect the prediction of thermal conductivity of the rods.

5.2.2 Boundary conditions

The boundary conditions used are:

- Linear heat rate at 4 axial positions;
- Fast neutron flux (>1 MeV);
- Coolant temperature
- Coolant pressure.

Linear heat rate (LHR) is considered constant over the time step in which it applies. The heat rate increase/decrease with a rate of 6 (Kw/m.h) for any change between different values of LHR. This transition rate and the time needed for the LHR to be changed is calculated based on the LHR in the peak position. The linear heat rate was measured and calculated at four positions of the rods. One of them is at the position of the thermocouples and the rest are at the bottom, middle and top of the rods. The axial positions of the measurements can be seen in *Table 5-4*.

The active part of the fuel was considered in this study. It was divided into 4 slices at the positions of LHR measurement given in *Table 5-4*. The rods are divided into a number of m_3 slices that are determined by the number of boundary condition points given in the experiment data. In TU, there are two different methods of dealing with the discretized slices; slice option or sectional option. In both cases, the fuel is analyzed slice per slice, starting from slice 1 up to slice m_3. The difference is that with the slice option, a slice is analyzed at the middle, i.e. at the axial position $\frac{z_i+z_{i+1}}{2}$, whereas with the sectional option a slice is analysed at the bottom and the top, i.e. at the coordinates z_i and

z_{i+1}. Thus, the total number of axial analyses is m_3 for the slice option and m_3 +1 for the sectional option. In addition, there is another difference: in the slice option, it is assumed that all axial quantities, e.g. the linear rating, are constant along the slice, whereas in the sectional option these quantities may vary linearly along the slice.[11]

In this work, the rod is treated using the sectional option of the discretization since it showed more accuracy of capturing the experimental values of burn-up which is a crucial step in the beginning of the specific analysis of the code performance. The nodalization of the fuel rods is based on the positions of the locations on which the LHR is measured. A 5% uncertainty of LHR is taken into consideration in the analysis as a factor that might affect the results.
The fast flux is calculated from the LHR according to the following equation.

$$Fast\ flux\ level = 1.6.10^{11} * LHR$$

As for the coolant temperature and pressure they are taken as constant values for the cold and hot conditions. They are taken to be the standard values of operation of HBWR (240^0C, 33.3 bar).

Name	**Position-Rod10 (mm)**	**Name**	**Position-Rod11 (mm)**	**Location**
LHRB1	0.0	LHRB2	0.0	Bottom
LHRM1	112	LHRM2	110	Mid
LHRT1	224	LHRT2	220	Top
LHRTF1	184	LHRTF2	180	TF tip position

Table 5-4 IFA-597 experiment, local heat rate measurement positions.

5.2.3 Burn-up investigation

A first and important step to be done before any further analysis takes place is the investigation of the effect of burn-up. This is important to demonstrate the validity of any calculation done. In fact, it helps in assuring that the rod being analyzed is actually modelled in the actual state when the test ends. In TU code, burn-up was calculated according to TU-LWR burn-up models[11]. As usual, due to uncertainty of experimental data (which is ±5%) and simplification of the model adopted, the calculations are retained in agreement up to around ±10% of the experimental data.

In *Figure 5-5*, the experimental data are plotted taking into consideration 5% uncertainty. It can be seen that the burn-up for the solid rod is slightly under-predicted but lies within the 5% uncertainty of the experimental calculations. For the hollow rod, a general over-prediction of the burn-up is noticed that exceeds in the mid-section of the experiment the 5% uncertainty level but it is still acceptable (since it did not exceed 10% range of uncertainty). At the end of the experiment, the burn-up predicted by TU is within the 5% uncertainty again. To conclude, the calculations capture the burn-up of these rods and are therefore representative of their status.

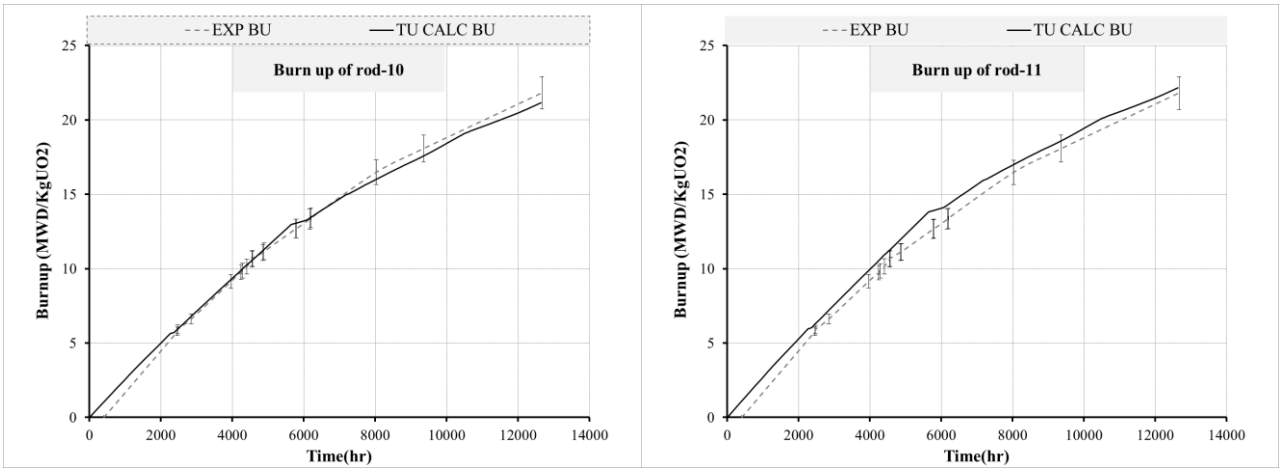

Figure 5-5 Simulation of IFA-597, preliminary results: burn-up analysis.

5.3 Reference analysis of IFA597.4/.5

5.3.1 Fuel temperature

The fuel temperature is analyzed in *Figure 5-6* and *Figure 5-7*. These figures report the measured centerline temperature, the simulated temperature at the corresponding axial position (which is slice 4) and the evolution of the fuel to cladding gap (simulated only) in the peak axial position (slice 2).

Solid rod (rod-10, *Figure 5-6*): matches well the experimental data. It can be noticed as well that at the end of each cycle, the code tends to slightly over-predict the temperature. This could be connected to uncertainties in the LHR. The fuel to cladding gap is predicted to remain opened.

The hollow rod (rod-11, *Figure 5-7*), is slightly under-predicted at the beginning of the first cycle. This could be connected to parameters that affect densification; in fact these parameters are modelled based on an average grain size and porosity whose local deviations may affect densification phenomena and consequently fuel temperature. The second cycle is less dependent upon densification and it follows the same trend as with the solid rod: the code begins with a good fit with experimental data then over-predicts the temperature later in the cycle.

During the whole simulated experiment, the predicted temperature did not deviate from the experiment measurement more than ±35 ^{0}C. This should lie within the ±5% uncertainty level of the LHR as later illustrated in the sensitivity analysis (section 5.4.1). The code can generally predict the temperature of the irradiated MOX appropriately. The dependency of the gap width on the temperature can be seen as well. As the temperature increases, the gap width tends to decrease and vice versa. Gap width size would affect the prediction of the gap conductivity which is a source of feed-back to the prediction of the centerline temperature.

5.3.2 FGR and pin pressurization

The Fission Gas Release (FGR) is analyzed in *Figure 5-8* and *Figure 5-9*. These figures report the measured centerline temperature, the simulated integral FGR and the calculated FGR (which has been given in the experimental report based on on-line pressure measurements and burn-up calculations).

The code under-estimated FGR for the solid rod, *Figure 5-8*. The maximum FGR predicted by the code was 4% while the experimental reached up to 7%. It should be mentioned that, in fuel pin mechanic code simulations, these relatively low values of FGR are generally retained acceptable even with deviations in the range -50%, +100%. When the code was able to predict releases, it predicted

them at the right onset and LHR. This confirms the selection of the burst release model (typically adopted for power ramps) which causes grain boundary venting when a given power variation and local temperature are met.

For the hollow rod, TU failed to predict FGRs, the maximum was 1% while the experiment reached up to 10.4%. The failure of the code with the hollow rod could not be explained but it might be due to the failure of predicting micro-cracking of the fuel which generates pathways for the fission gases to be released through.

The pin pressurization is depicted in *Figure 5-10* and *Figure 5-11*. These figures report the measured pin pressure, the simulated pin pressure and the simulated total and upper plenum free volumes.

For the solid rod (*Figure 5-10*), the pressure was slightly over-predicted in IFA-597.4 (first cycle) and slightly under-predicted in IFA-597.5 (second cycle). In the first cycle, the over prediction can be related to under estimation of densification or relocation by the code which means predicting a smaller free volume which leads to over prediction of the pressure. In the second cycle, the under-prediction of the pressure can be related to the under-prediction of FGR. The same is true for the hollow rod (*Figure 5-11*), and we can notice that the over prediction in the first cycle is higher than that of the solid rod and the pressure is highly under-predicted in the second cycle which is consistent with the very low FGRs predicted by the code.

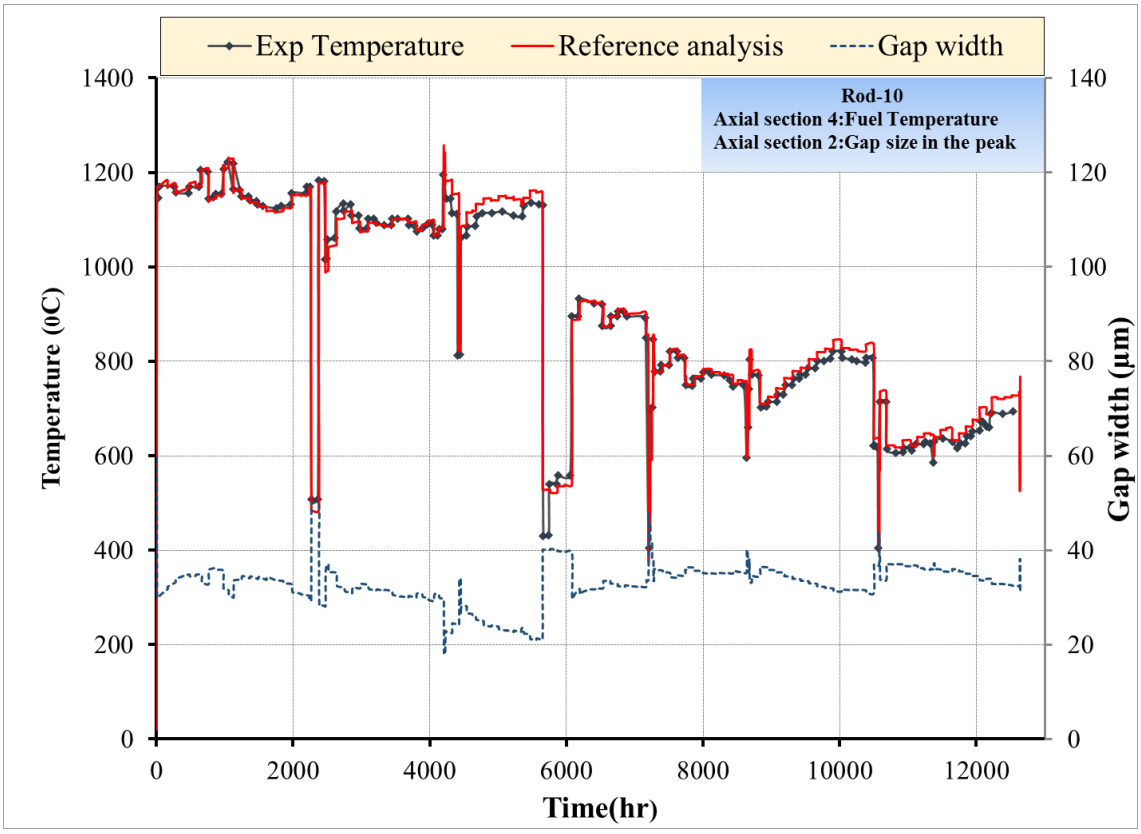

Figure 5-6 Simulation of IFA-597, reference results: fuel temperature evolution in rod 10.

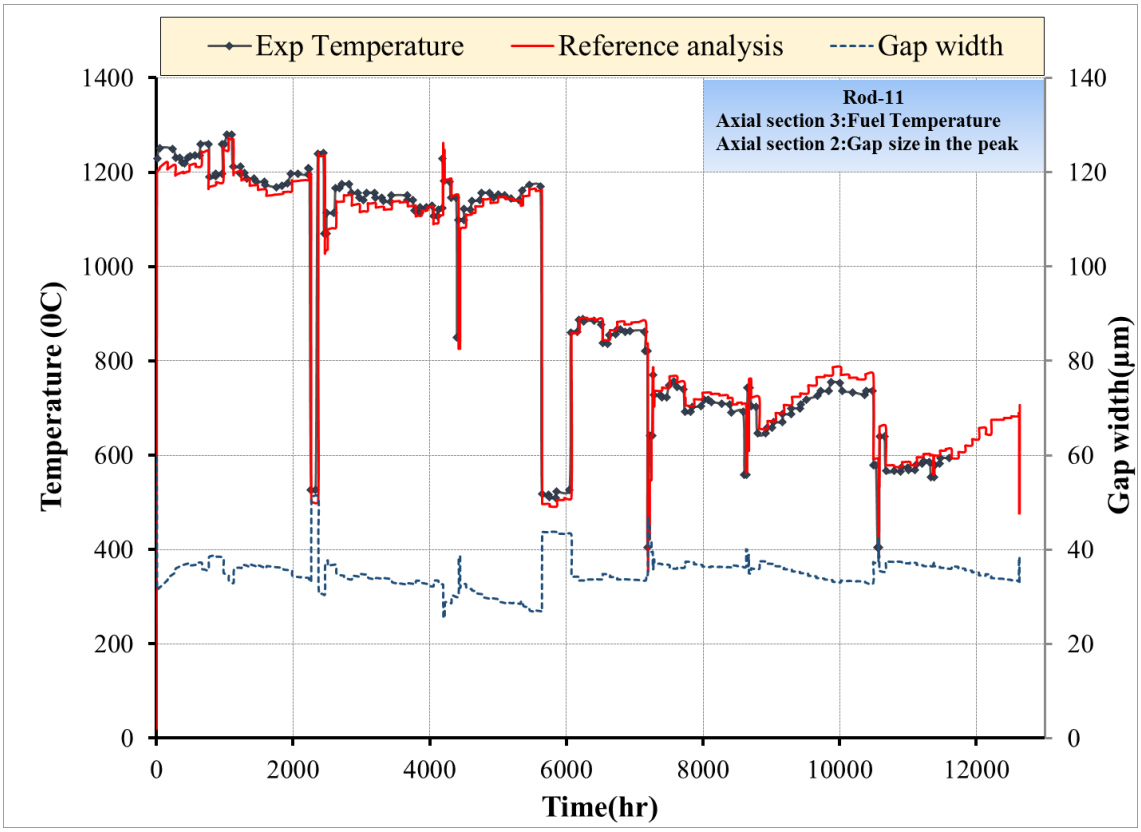

Figure 5-7 Simulation of IFA-597, reference results: fuel temperature evolution in rod 11.

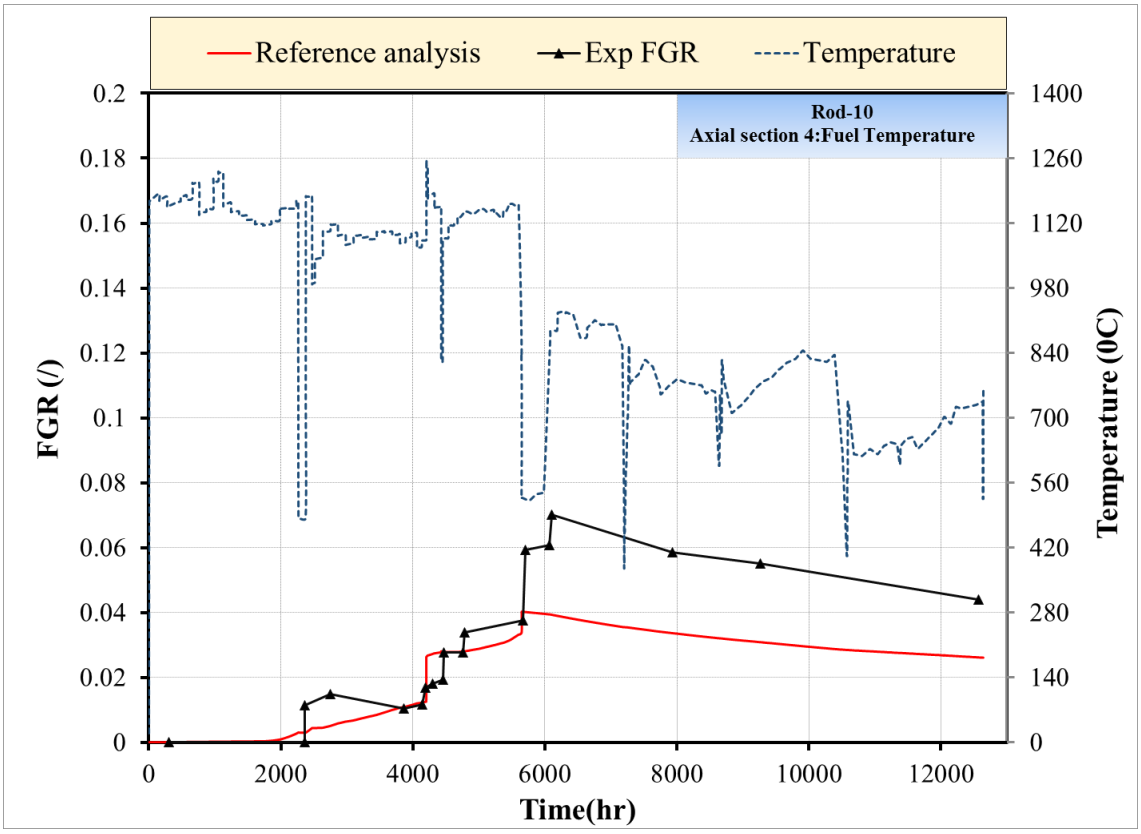

Figure 5-8 Simulation of IFA-597, reference results: FGR evolution in rod 10.

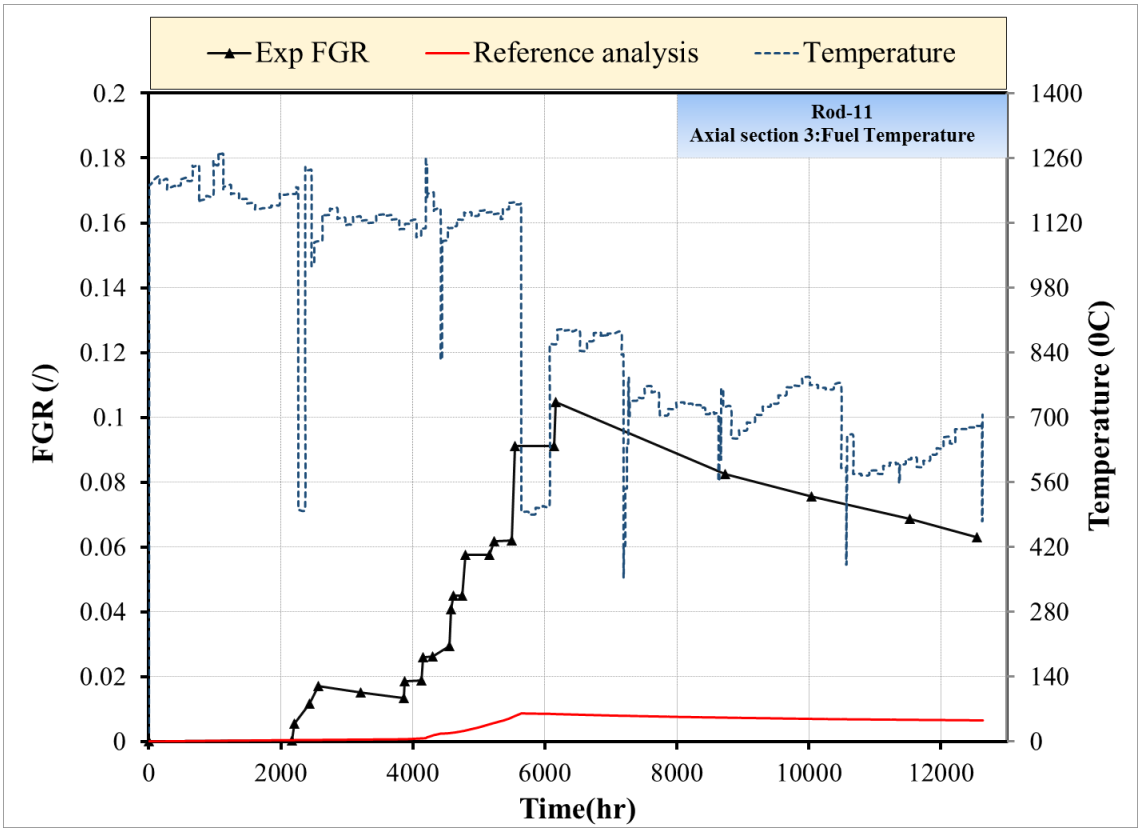

Figure 5-9 Simulation of IFA-597, reference results: FGR evolution in rod 11.

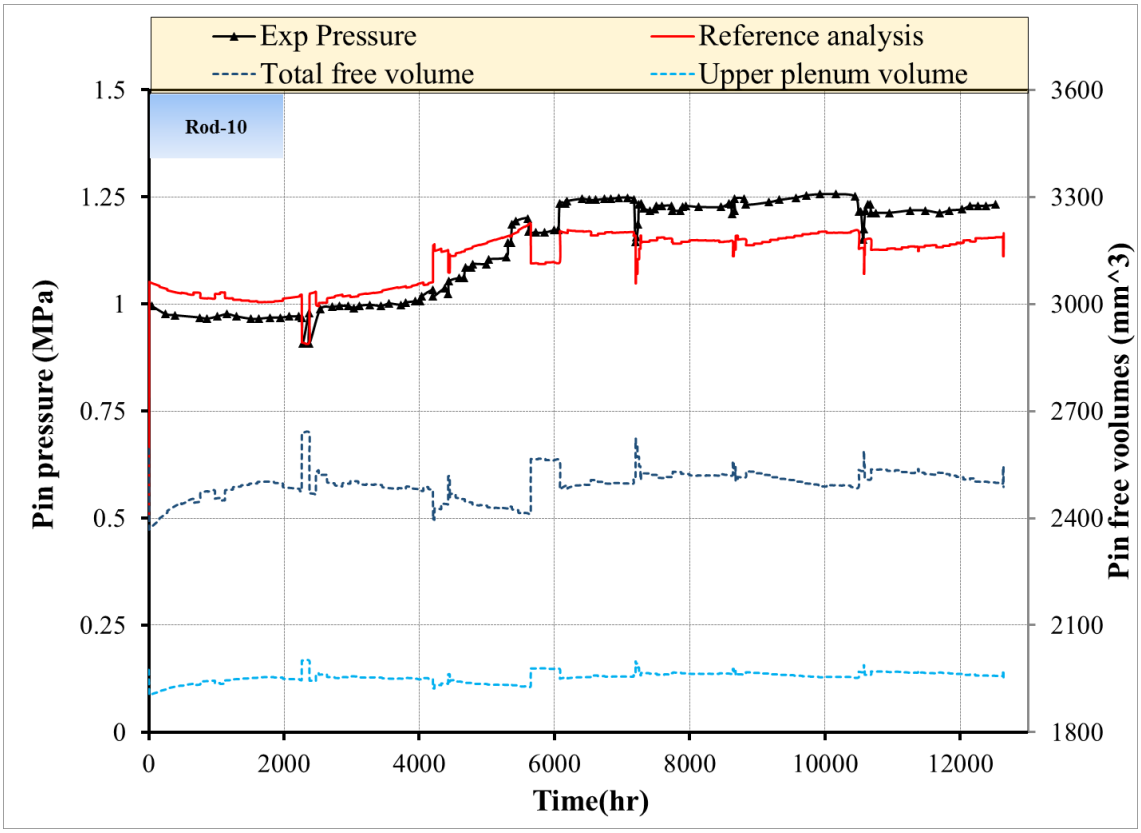

Figure 5-10 Simulation of IFA-597, reference results: pin pressure evolution in rod 10.

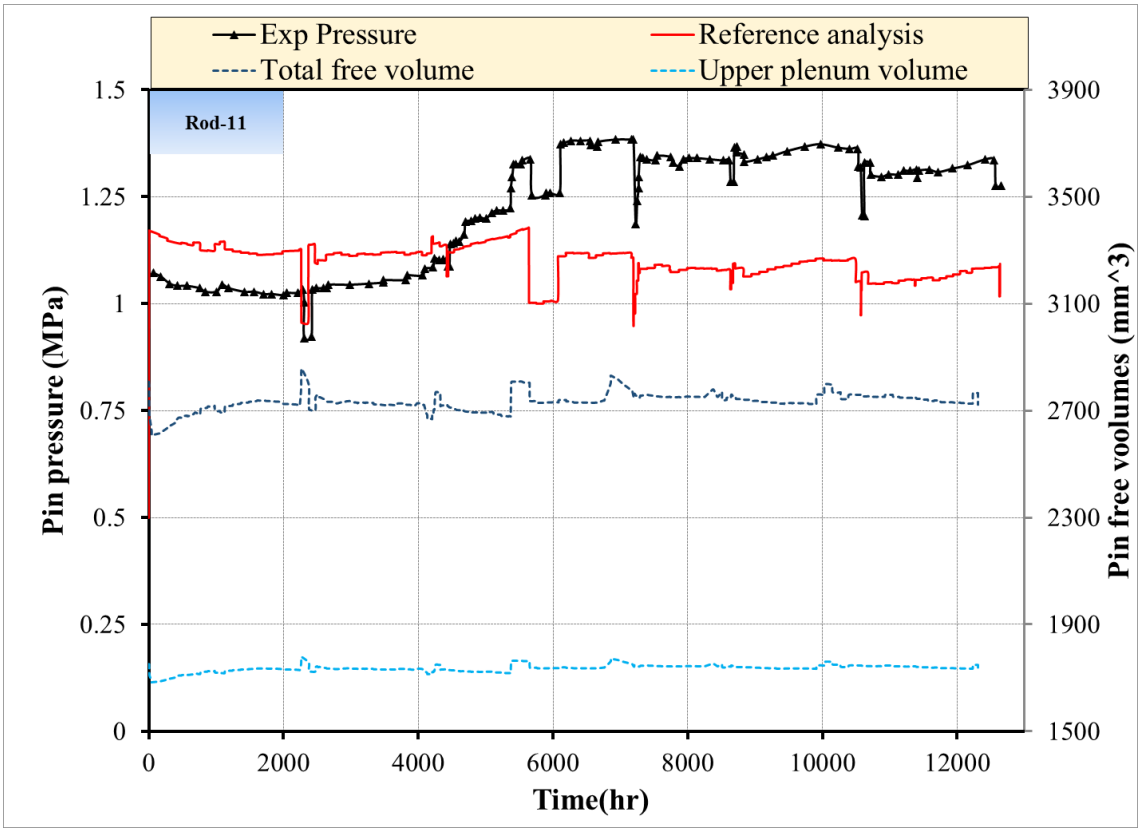

Figure 5-11 Simulation of IFA-597, reference results: pin pressure evolution in rod 11.

5.4 Sensitivity analysis

It is important to conduct sensitivity analysis of the code to the various conditions, correlations and models that are provided as options in the code. This step is helpful in the demonstration of robustness of the calculations, detecting possible reasons for discrepancies between calculations and measurements, and identifying parameters that require higher accuracy in their values in order to be able to get results that are more accurate by the code.

In *Table 5-5*, A list of all sensitivity analyses that were performed during this study could be found and the motivation behind them. The analyses were performed on either parametric design values given by the experiment data, or correlations and models provided by the code. Design parameters are labeled by **(D)**, while correlations are labeled by **(C)** and models labeled **(M)**.

In the next subsections, separate sensitivity analyses of the factors stated in *Table 5-5* are illustrated.

Case	Run	Modification	Objective
Fuel conductivity	**C1.1**	Modfuel(j=6)=31	Investigate the impact of fuel conductivity on fuel temperature, pin pressure and FGR. *Correlation of Van Uffelen & Schubert.*
	C1.2	Modfuel(j=6)=32	Investigate the impact of fuel conductivity on fuel temperature, pin pressure and FGR. *Correlation of Carbajo..*
	C1.3	Modfuel(j=6)=33	Investigate the impact of fuel conductivity on fuel temperature, pin pressure and FGR. *Correlation of Lanning & Beyer.*
	C1.4	Modfuel(j=6)=24	Investigate the impact of fuel conductivity on fuel temperature, pin pressure and FGR. *According to Wiesenack multiplied by a MOX correction factor.*
Pellet fragment relocation	**M1.1**	Ireloc 2	Investigate the impact of fuel relocation on fuel temperature, pin pressure gap size and FGR. *Original KWU-LWR model based on initial gap size only.*
	M1.2	Ireloc 3	Investigate the impact of fuel relocation on fuel temperature, pin pressure, gap size and FGR. *GAPCON-THERMAL-3 based on initial gap size, LHR and burn-up.*
	M1.3	Ireloc 5	Investigate the impact of fuel relocation on fuel temperature, pin pressure, gap size and FGR. *Modified KWU-LWR model, own calibration 1997*
	M1.4	Ireloc 8	Investigate the impact of fuel relocation on fuel temperature, pin pressure, gap size and FGR. *Modified FRACPON-3 model based on the as fabricated gap, the burn-up and the linear heat rate.*
Fuel swelling	**C2.1**	Modfuel(j=4)=18	Investigate the impact of fuel swelling on fuel temperature, gap size, fuel elongation and FGR. *Simple correlation applied: swelling proportional to burn-up.*
	C2.2	Modfuel(j=4)=19	Investigate the impact of fuel swelling on fuel temperature, pin pressure and FGR. *Original MATPRO swelling model considering separate contributions of the solid and gaseous fission products*
	C2.3	Modfuel(j=4)=20	Investigate the impact of fuel swelling on fuel temperature, pin pressure, gap size and FGR. *Implicit formulation of the reference correlation.*
Fission gas release	**M2.1**	Igrbdm 3 FGRmod 4	Investigate the impact of intra-granular and inter-granular models on fuel temperature, pin pressure and FGR. *Inter-granular model according to the modified Koo model and intra-granular model of Matzke and White Tucker.*
	M2.2	Igrbdm 3 FGRmod 6	Investigate the impact of intra-granular and inter-granular models on fuel temperature, pin pressure and FGR. *Inter-granular model according to the modified Koo model and intra-*

			granular diffusion coefficient according to Matzke (thermal) and a constant athermal diffusion coefficient.
	M2.3	Igrbdm 3 FGRmod 9	Investigate the impact of intra-granular and inter-granular models on fuel temperature, pin pressure and FGR. *Inter-granular model according to the modified Koo model and intra-granular model of Turnbull.*
	M2.4	Igrbdm 1 FGRmod 6	Investigate the impact of intra-granular and inter-granular models on fuel temperature, pin pressure and FGR. *Inter-granular model according to the standard model and intra-granular diffusion coefficient according to Matzke (thermal) and a constant athermal diffusion coefficient.*
	M2.5	Igrbdm 2 FGRmod 6	Investigate the impact of intra-granular and inter-granular models on fuel temperature, pin pressure and FGR. *Inter-granular model according to the temperature dependent model and intra-granular diffusion coefficient according to Matzke (thermal) and a constant athermal diffusion coefficient.*
Gap conductan-ce	**M3.1**	Ihgap 0	Investigate the impact of gap conductance models on fuel temperature, pin pressure and FGR. *Gap conductance model according to the standard model*.
	M3.2	Ihgap 3	Investigate the impact of gap conductance models on fuel temperature, pin pressure and FGR. *Gap conductance model according to the Lindsay & Bromley*. *Accommodation coefficients not taken into account.*
	M3.3	Ihgap 4	Investigate the impact of gap conductance models on fuel temperature, pin pressure and FGR. *Gap conductance model according to Tondon & Saxena*. *Accommodation coefficients are taken into account.*
Gap size	**D3.1**	Gap size (+12μm)	Test the impact of increased gap width at the beginning of irradiation on fuel temperature and FGR. Initial value obtained assuming maximum cladding and minimum fuel radii according to design uncertainties.
	D3.2	Gap size (-12μm)	Test the impact of decreased gap width at the beginning of irradiation on fuel temperature and FGR. Initial value obtained assuming minimum cladding and maximum fuel radii according to design uncertainties.
Grain size	**D1.1**	4.4μm	Assess the impact of decreasing grain size to the lower limit defined by the experiment data on FGR and fuel centerline temperature.
	D1.2	6.6μm	Assess the impact of increasing grain size to the upper limit defined by the experiment data on FGR and fuel centerline temperature.
Sintering porosity DENPOR	**D2.1**	+50%	Assess the impact of increasing the sintering porosity on the prediction.
		-50%	Assess the impact of decreasing the sintering porosity on the prediction.
DENBUP	**D3.1**	0 MWD/tHM	Assess the impact of not considering fuel densification on the prediction of CLT.
	D3.2	3000 MWD/tHM	Assess the impact of considering fuel densification lower cutoff burn-up on the prediction of CLT.
	D3.3	10000 MWD/tHM	Assess the impact of considering fuel densification higher cutoff burn-up on the prediction of CLT.

Table 5-5 Simulation of IFA-597, list of correlations, models and design parameters considered in the sensitivity studies.

5.4.1 Linear heat rating uncertainty

Uncertainty in linear heat rating should be investigated to determine its effect on fuel centerline temperature prediction. In this experiment the uncertainty ranged between 5% at the BOL and reached

around 10% at the end of cycle. In this study only the initial 5% uncertainty is taken into account. In *Figure 5-12*, *Figure 5-13* and *Figure 5-14*, the uncertainty limits are tested against the measured temperature, the measured pin pressure and the calculated FGR.

In *Figure 5-15* it can be seen in the beginning of IFA-597.4 and before FGR takes place, that increasing/decreasing the LHR with ±5% leads to uncertainty of temperature of less than 5%. FGR results in feedbacks that affected the pin pressure. At higher LHR by releasing more fission gases the gap conductivity degrades which leads to even higher temperatures and the increase of temperature increases by more than 5% in the rest of the experiment and can reach up to 10 or 15%.[24] The opposite is true at 95% LHR. With the lower temperature, lower FGR is predicted which means that the gap conductance suffers less degradation than in the nominal case. Then the better conduction, the lower the temperature becomes and the feedback of FGR results in a temperature decrease of between 5-10%. FGR does not vary linearly with LHR. Increasing the LHR results in more increase in FGR than the rate of the decrease when the LHR is decreased by the same ratio. The FGR uncertainty affects the pressure in the gap as well. In fact the gap pressure (*Figure 5-16*) is more sensitive to FGR than temperature and can vary between 20 to 30% at IFA-597.5. An over-all effect of this LHR uncertainty is that the code predicts temperatures and pressures that include the experimental measurements within their upper and lower limits.

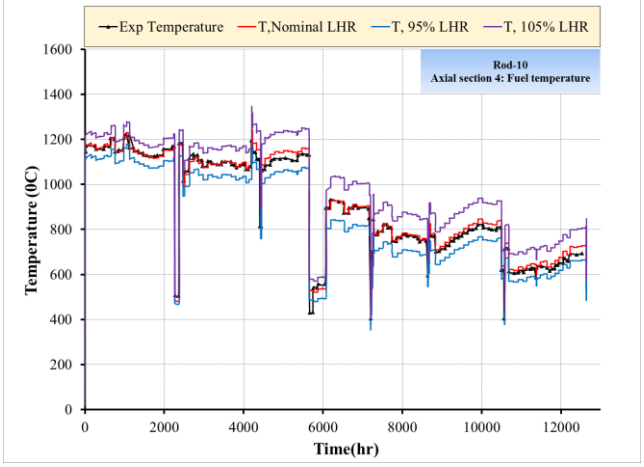

Solid rod (rod-10)

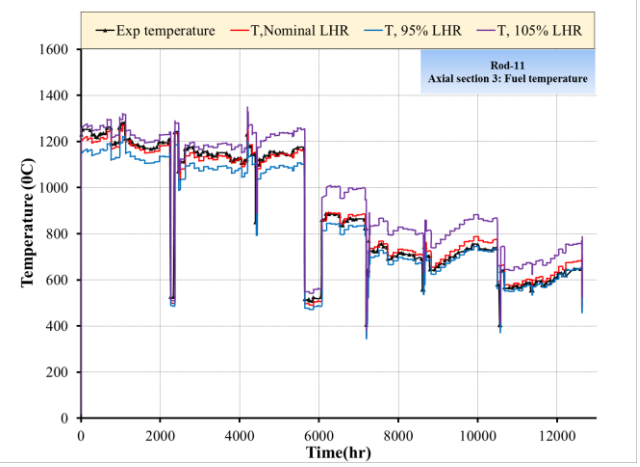

Hollow rod (rod-11)

Figure 5-12 Simulation of IFA-597, sensitivity analysis on LHR, fuel temperature.

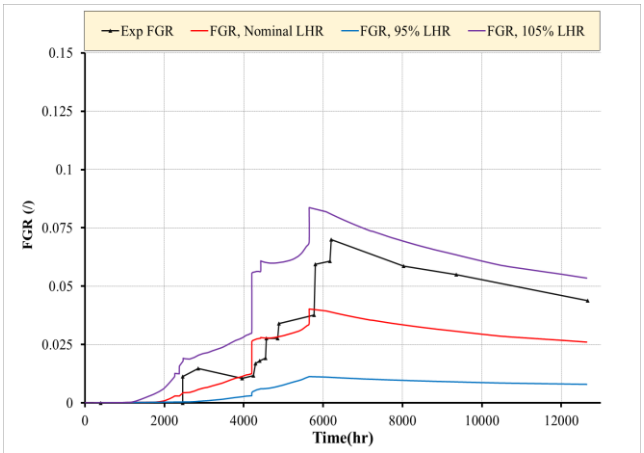

Solid rod (rod-10)

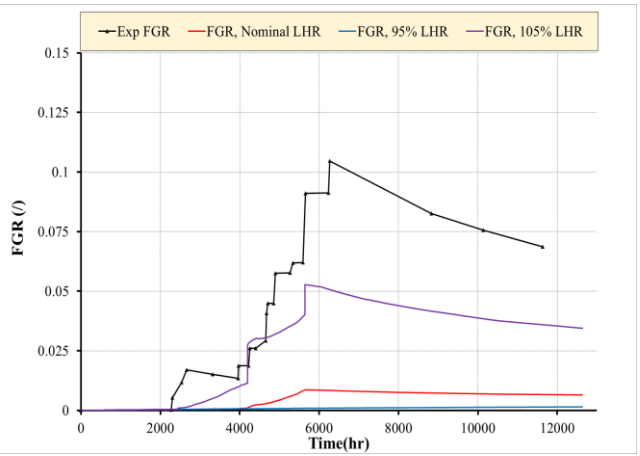

Hollow rod (rod-11)

Figure 5-13 Simulation of IFA-597, sensitivity analysis on LHR, FGR.

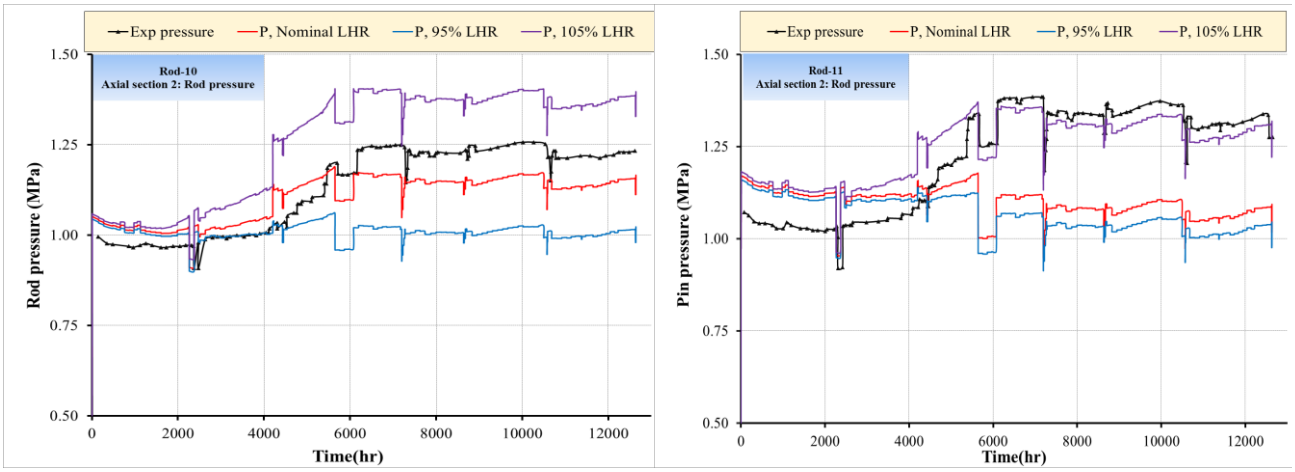

Solid rod (rod-10) *Hollow rod (rod-11)*

Figure 5-14 Simulation of IFA-597, sensitivity analysis on LHR, rod pressure.

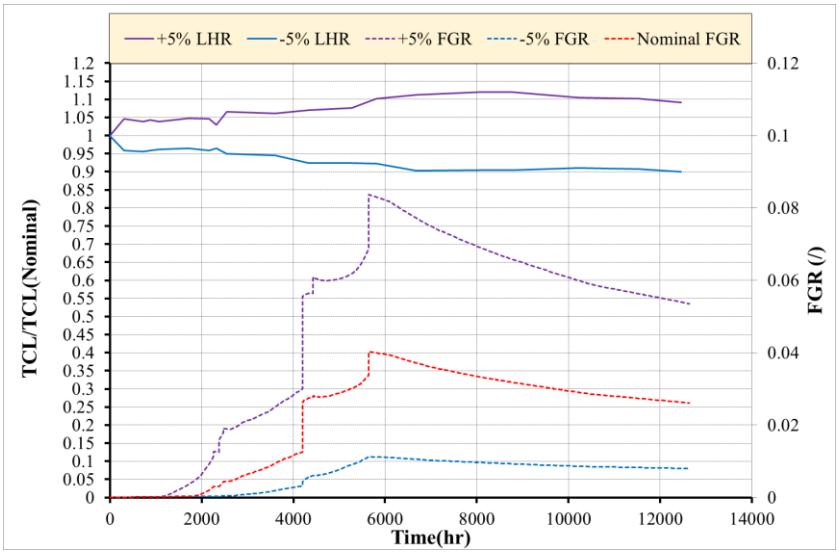

Figure 5-15 Simulation of IFA-597, sensitivity analysis on LHR, variation on fuel centreline prediction of rod-10.

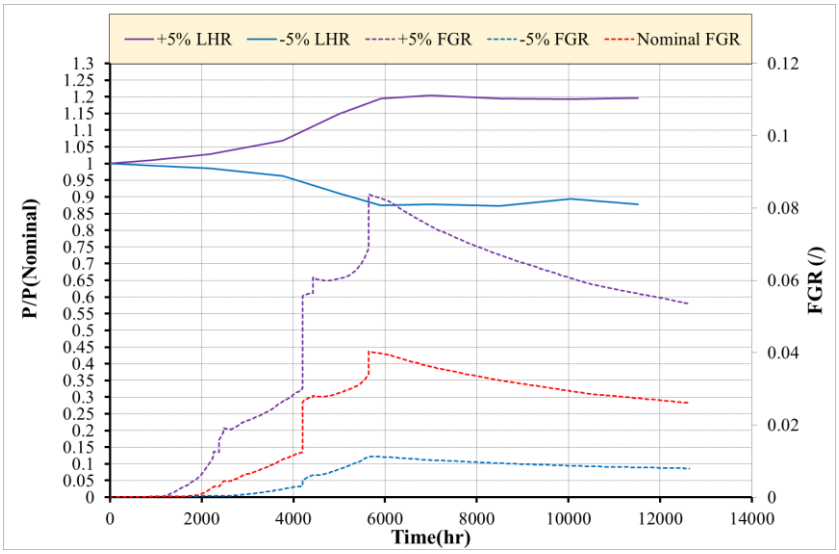

Figure 5-16 Simulation of IFA-597, sensitivity analysis on LHR, variation on rod pressure prediction of rod-10.

5.4.2 Thermal conductivity correlations

The correlations described in section 3.1 are tested in this analysis. *Figure 5-17* and *Figure 5-18* report the influence of the conductivity correlations on the prediction of the fuel temperature and FGR-pin pressurization, respectively.

There is a close match in the predicted temperature by the MOX correlations of Lanning & Beyer (Cond-33) and Carbajo (Cond-32) and the standard correlation of TU of Van Uffelen & Schubert (Cond-31), *Figure 5-17*. Cond-32 predicted temperatures approximately of the same values of the standard correlations except in the beginning of irradiation up to 975 hr where the temperature predicted is higher than the standard correlation. Cond-33 predicted temperature is slightly higher than that of the standard correlation over most of the time span of irradiation. The temperature over-prediction by Cond-33 does not become higher than 20^0C. The correlation of Wiesenack (Cond-34) under-predicted the temperature during the whole range of irradiation. This under-prediction can reach up to 65^0C at some points of time in IFA597.5. This correlation is originally designed for UO_2 fuel and multiplied by a factor of 0.92 as an approximation for MOX fuel. The conductivity of UO_2 is higher than that of MOX fuel. Therefore, the factor taken is not low enough to reduce the thermal conductivity to a value comparable to the rest of the correlations originally designed for MOX. The result of this higher thermal conductivity by Cond-34 is that the prediction of temperature is lower than the standard correlations and experimental data. To conclude, the standard correlation of TU is the one that best captures the experimental measurements. The previous analysis applies for both rods.

For both rods, the correlations predict similar FGR and pin pressures in the first two thirds of IFA597.4. Then the correlations deviate from each other. The values predicted by Cond-34 is the earliest to deviate from the others. The rest begins to show different predictions of the pin pressure and FGR in a later stage. It can be noticed comparing *Figure 5-17* and *Figure 5-18* that the prediction of higher temperature results in a higher prediction of FGR and consequently higher pin pressure. This is obviously connected to the thermally activated mechanisms that take place in the diffusion of fission gases into the grain and accumulation and release of gases from the grain boundaries to the pin free volume.

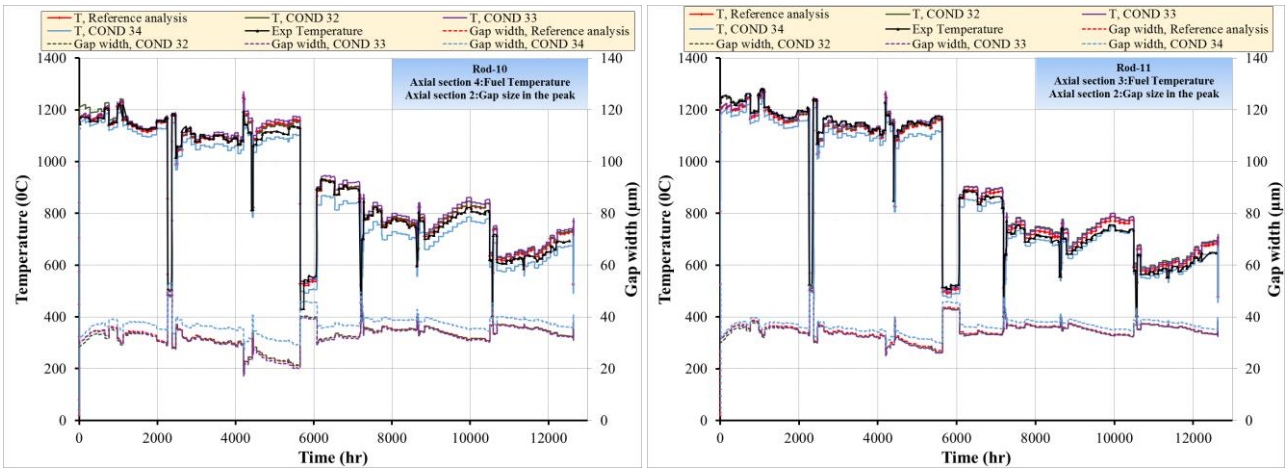

Solid rod (rod-10) *Hollow rod (rod-11)*

Figure 5-17 Simulation of IFA-597, sensitivity analysis on fuel conductivity correlations, temperature prediction.

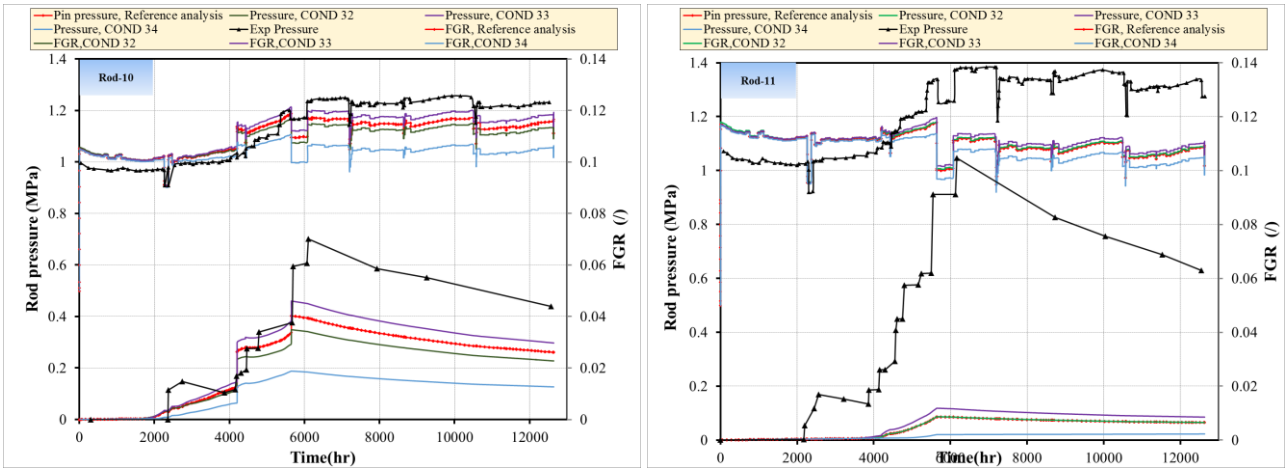

Solid rod (rod-10) *Hollow rod (rod-11)*

Figure 5-18 Simulation of IFA-597, sensitivity analysis on fuel conductivity correlations, rod pressure and FGR prediction.

5.4.3 Relocation models

The direct effect of the pellet fragment relocation models is on the gap width between fuel and cladding. Variations of the size of the gap will result in a variation of the gap conductivity and variation of the prediction of temperature. The reference relocation model is the modified FRAPCON-3 model (RELOC-8). The model depends on the as fabricated gap, the burn-up and LHR. It neither considers axial strain nor can it be applied when the gap is closed[11]. The other models are:

- The original KWU-LWR model (RELOC-2) accounts for the as fabricated gap, for tangential and axial relocation and it is also applied when gap is closed. [23]
- The GAPCON-THERMAL-3 (RELOC-3) accounts for the tangential strain due to relocation depending on the as fabricated gap, the burn-up (exponential function that saturates at 5MWd/kgU), the linear heat rate (a simple function). It does not consider the axial strain and it is also applied when the gap is closed. [23]
- The modified KWU-LWR (RELOC-5) accounts for the tangential and axial strain due to relocation depending only on the as fabricated gap. It is also applied when gap is closed.

Although the models have impact directly on the gap width, this parameter was not measured in the experiment. Therefore, one can compare how much the predicted gap results in an accurate prediction of temperature.

Figure 5-19 analyzes the effect of the relocation models on the fuel temperature, the variation of the gap widths between the various relocation models studied is plotted. For rod-10, IRELOC-8 and IRELOC-2 are consistent with each other and predict temperature values closer to the experimental data. IRELOC-8 gives a closer prediction to the experimental temperature than IRELOC-2. Overall, IRELOC-2 does not predict a temperature difference higher than 25^0C on the whole range of irradiation. The wider gap predicted by IRELOC-5 results in a higher prediction of temperature while the opposite is true for IRELOC-3; the code is more sensitive to the increase of the predicted gap size than the decrease of the gap size. Therefore, IRELOC-5 highlights an increase of temperature that can reach up-to 115 ^{0}C more than the reference case. IRELOC-3 predicts a decrease that reaches a maximum of 75 ^{0}C (compared to the reference case).
Rod-11 highlights similar trends except in the final part of the irradiation in which IRELOC-3 had the best match with the experimental temperature. Based on the results of rod-10, IRELC-2 was not taken into consideration in the analysis of Rod-11.

To conclude, IRELOC-8 is the model that was the closest to the experimental temperatures over the whole range of irradiation for both rods. IRELOC-3 was only better for IFA597.5 for the hollow rod only.

The rod pressure and FGR are analyzed in *Figure 5-20*: they reflect the prediction of temperature. In fact, due to the over-prediction of temperature, IRELOC-5 overestimates the FGR and pin pressure with respect to the experimental data (rod-10).

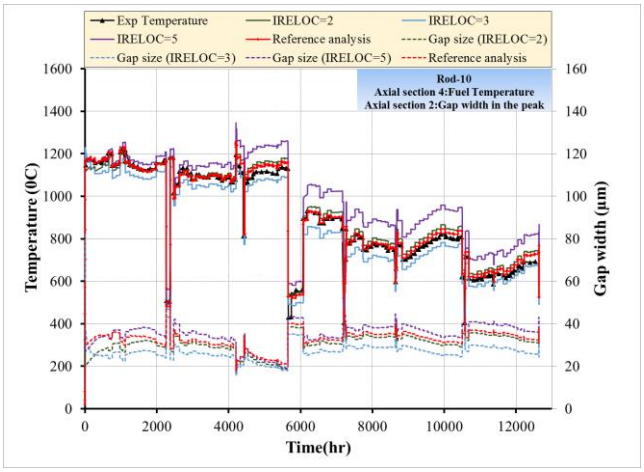

Solid rod (rod-10)

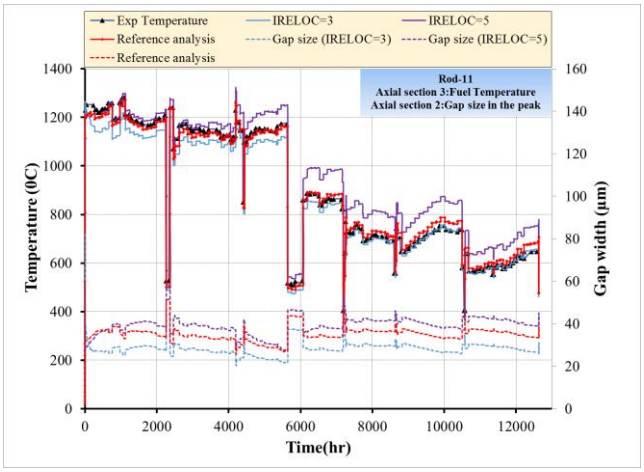

Hollow rod (rod-11)

Figure 5-19 Simulation of IFA-597, sensitivity analysis on relocation models, temperature prediction.

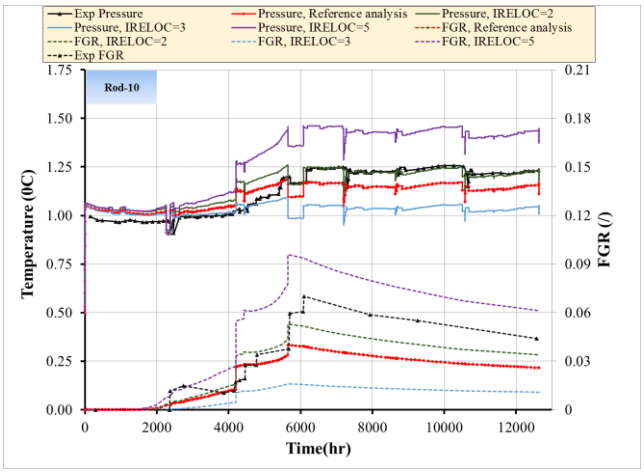

Solid rod (rod-10)

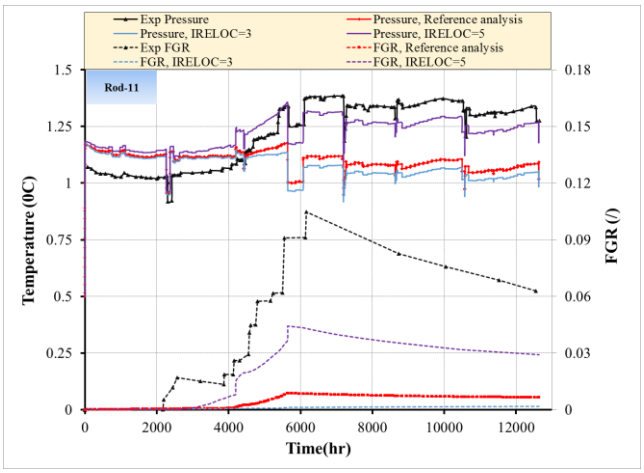

Hollow rod (rod-11)

Figure 5-20 Simulation of IFA-597, sensitivity analysis on relocation models, Pressure & FGR prediction.

5.4.4 Swelling correlations

Swelling occurs in nuclear fuel due to the accumulation of fission products generated during irradiation. The contributions of solid and gaseous FPs to fuel swelling are different from each other. For the gases in solid solution and the small intra-granular gas bubbles, it is estimated that they furnish about 0.056% per MWd/kgU to matrix swelling rate.[23] The contribution of gases to swelling is mainly due to the formation of Xenon and Krypton gases. The formation of bubbles of gases leads to the increase in the volume of the solid. Inter-granular gas bubbles can make the largest contribution to swelling depending on the amount of gas formed and the temperature range of operation. At temperatures high enough, those bubbles can interlink together and form a tunnel path for gases to be

released. Therefore, fuel swelling will affect FGR, gap width between fuel and cladding and thermal conductivity of the fuel. Different correlations modelling fuel swelling will result in variations of thermal conductivity of the fuel element hence temperature prediction and FGR and the sensitivity of those predictions to fuel swelling should be investigated. In this analysis the correlations used are based on oxide fuel since the correlations used for MOX fuel are still under development.

The reference standard model (SWE-20) considers solid swelling as a linear function of burn-up and applies an exponential term that depends on fitting constants, local temperature and local stress to account for gaseous swelling. The remaining models are[13][11]:

- SWE-18: is the simplest model that accounts for solid swelling only
- SWE-19 is the MATPRO swelling model and accounts for both solid swelling and gaseous swelling. This last contribution is linearly dependent on temperature and exponentially dependent on local burn-up.

The results are given in *Figure 5-21* and *Figure 5-22*, It can be seen that the prediction of the standard SWE-20 and SWE-19 of the temperature, pressure and FGR is the same for rod-10. In IFA597.4, the gap width predicted by both correlations is similar. In IFA597.5, the models did not predict the same gap width and there is a wide variation between the gap sizes of both correlations. The discrepancy between the predicted gaps should have affected the other predicted parameters (Temperature, FGR and pressure). This was not the case here, and a higher temperature was associated to a smaller gap width.
SWE-18 correlation is a simple one that takes only the volume change as a simple function of burn-up and does not consider swelling due to fission gases. SWE-18 resulted in a higher prediction of the temperature. It predicted higher FGRs which were comparable to the experimental data. This was a consequence of the higher temperature predicted.
The hollow rod was insensitive to the swelling correlations and no significant difference was detected.

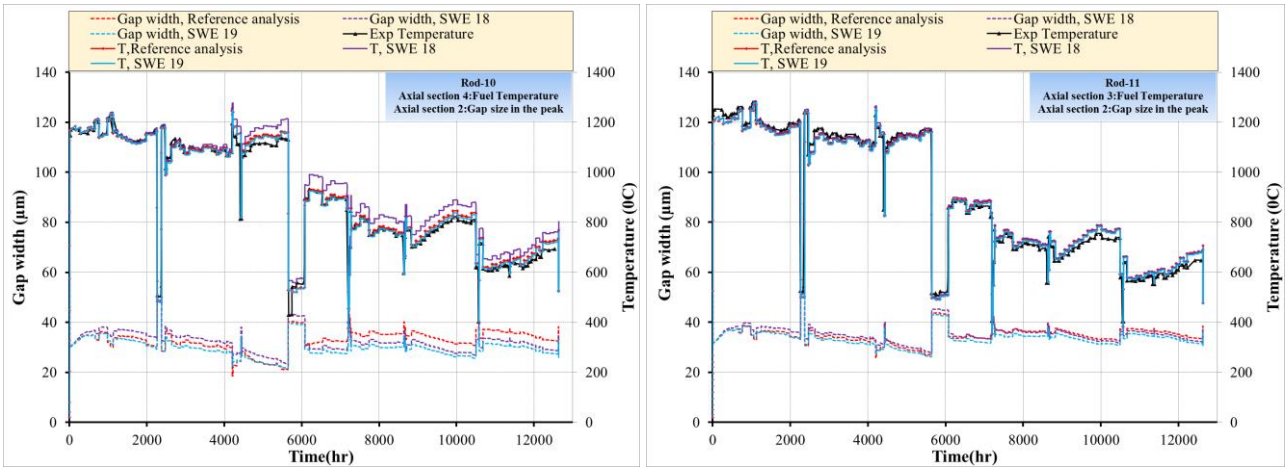

Solid rod (rod-10) *Hollow rod (rod-11)*

Figure 5-21 Simulation of IFA-597, sensitivity analysis on swelling correlations, temperature prediction.

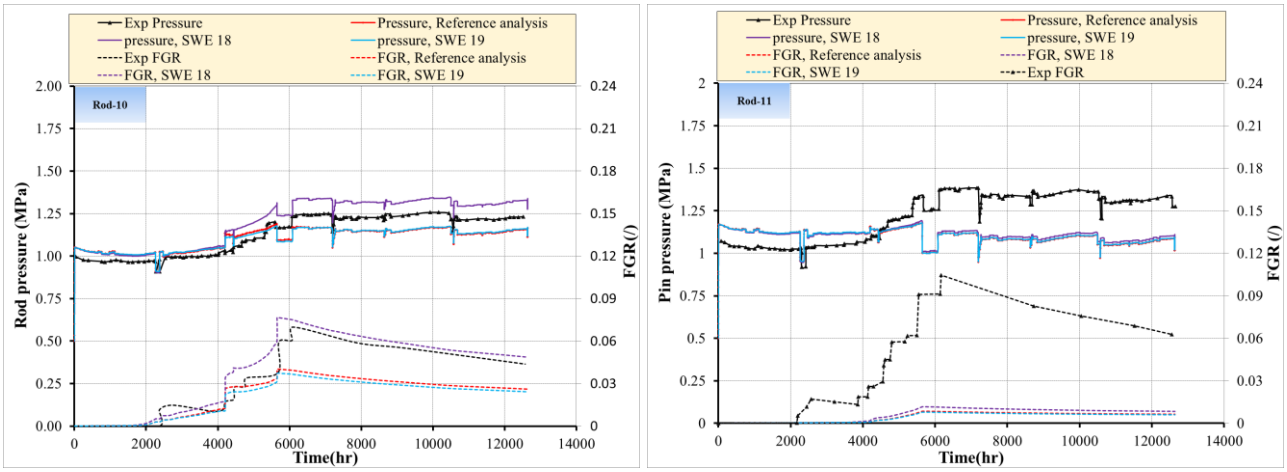

Solid rod (rod-10) *Hollow rod (rod-11)*

Figure 5-22 Simulation of IFA-597, sensitivity analysis on swelling correlations, rod pressure and FGR prediction.

5.4.5 FGR models

Three Intra-granular FGR models were investigated in this study along with three other inter-granular diffusion models. The reference case FGRMOD=6 is based on a model of Matzke for thermal intra-granular diffusion. For athermal diffusion, a model based on ITU data is used. The rest of the models can be found in *Table 5-5*. This model was combined with an inter-granular diffusion model derived from Koo model for a power ramp conditions (it assumes a constant standard value of gas concentration at grain boundaries and it releases the extra part of gas that reaches the boundaries if no ramp conditions are met. If the power variation exceeds 3.5kW/m and local temperature exceeds a burn-up dependent threshold the grain boundaries are completely vented to simulate micro-cracking of grain boundaries).

The intra-granular models analyzed are[11]:

- FGRMOD4 is based on the thermal diffusion coefficient of Matkze and athermal diffusion by White and Tucker.
- FRGMOD9 based on the atomic diffusional coefficient of Turnbull.

In *Figure 5-23*, for IFA597.4, there was no difference in temperature prediction between the models until the last stages of the cycle. This is expected since early in the experiment there were no FGR to cause differences. For rod-10, it can be seen that FGRMOD=4 gave the highest FGR but still not close to the experimental prediction. In IFA597.5, The temperature predicted by that model was slightly higher than the reference case within 15 ^{0}C. Model FGRMOD=9 gave the lowest of the three models. For rod-11, the FGR was not captured at all by all the models and the temperature predicted by them is almost equal and no preference can be made based on that rod.

For the IGRDM analysis, the reference intra-granular model FGRMOD=6 was fixed and the various IGRDM models were analyzed. They are:

- IGRDM1 which is the same as the reference option except the condition of venting in case of power ramps that is not accounted for.
- IGRDM2 that assumes the saturation concentration at grain boundaries to achieve the release of the extra gas as a function of the local temperature.

Again, for rod-11, the models did not predict FGR (*Figure 5-24*). The temperature predicted by IGRDM=2 had the best fit of temperature prediction with the experimental data. Still it had the worst under prediction of FGR. For rod-10, It can be seen that the prediction of temperature that best fits the experimental data is that for IGRDM=1. The FGR is more under predicted than for the reference case but they are still comparable to each other.

To conclude, the reference selection of models (that considers FGR due to micro-cracking) highlights the higher capability to capture both temperature and FGR even if this last parameter remains under-estimated.

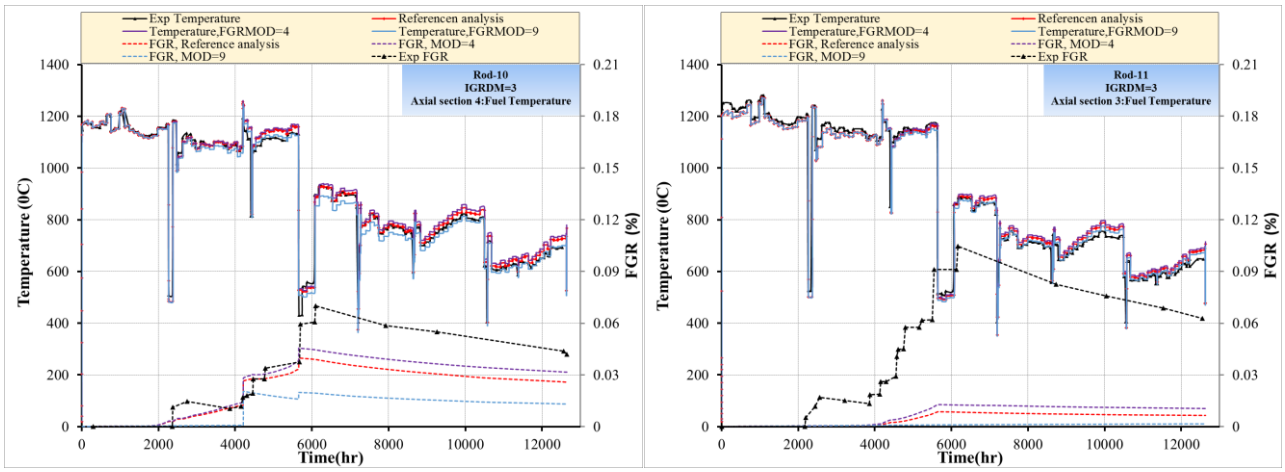

Solid rod (rod-10) *Hollow rod (rod-11)*

Figure 5-23 Simulation of IFA-597, sensitivity analysis on FGR: Intra-granular model coupled with inter-granular model IGRBDM=3, temperature and FGR predictions.

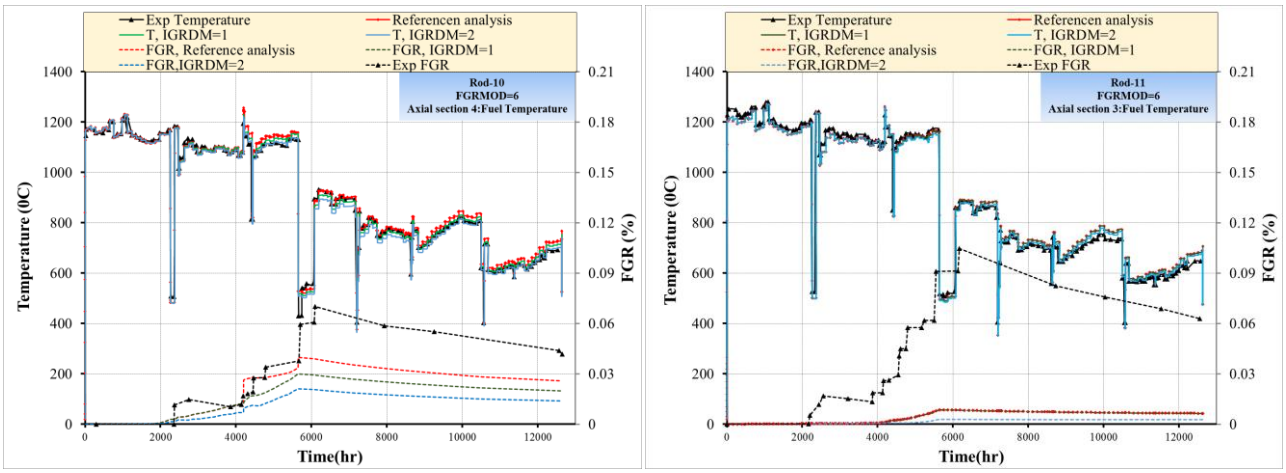

Solid rod (rod-10) *Hollow rod (rod-11)*

Figure 5-24 Simulation of IFA-597, sensitivity analysis on FGR: Inter-granular models coupled with intra-granular model FGRMOD=6, temperature and FGR predictions.

5.4.6 Gap conductance models

The ability to predict the gap conductance will affect the whole thermal resistivity of the fuel rod. IHGAP=0 is the standard model based on thermal conductivity of mixture according to Lindsay and Bromley with accommodation coefficients taken into account.[11] The remaining models are:

- IHGAP 3: as standard option but without considering accommodation coefficients.

- IHGAP 4: thermal conductivity of mixture according to Tondon and Saxena. Accommodation coefficients are taken into account.

Taking accommodation coefficients into account does not result in significant difference from the case when they were neglected, *Figure 5-25*. The difference in temperatures between both cases does not exceed 5 ^{0}C. Based on IFA597, no preference can be made between IHGAP=3 and IHGAP=4. At some parts of the experiment IHGAP=3 fits well with experimental data and at other points IHGAP=4 is better. At some points both models predict the same value. A general conclusion is that the temperature prediction is not significantly sensitive to the different models implemented in TU.

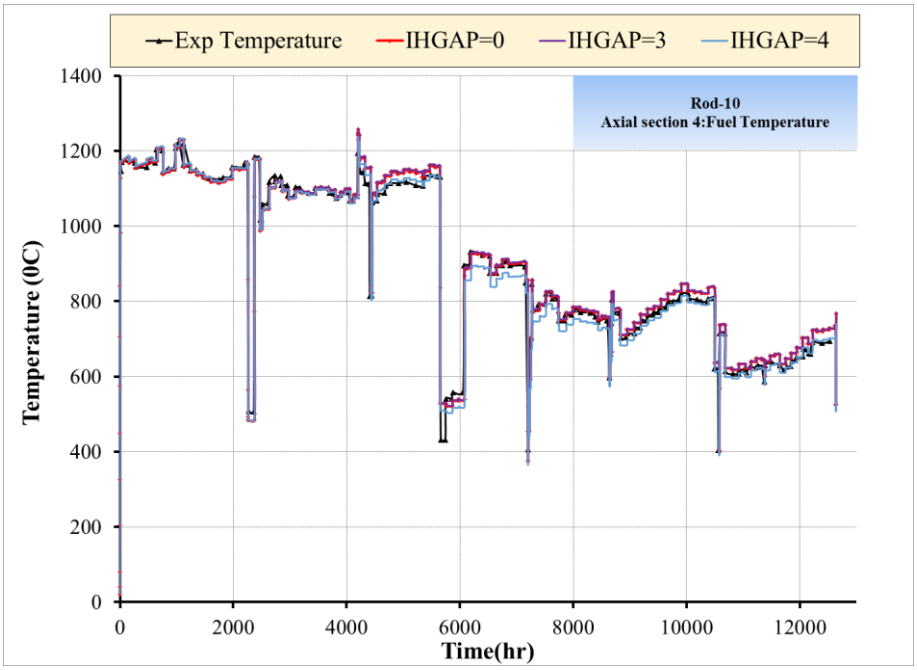

Figure 5-25 Simulation of IFA-597, sensitivity analysis on gap conductance, temperature prediction.

5.4.7 Other parameters

Initial gap width

The initial gap width is a parameter provided by the experimental data. In this study, the nominal initial gap width was assumed to have around 15% uncertainty. 80% percent of this uncertainty was due to uncertainty in the outer fuel radius and 20% was related to the inner cladding radius. The results of the conducted analysis is that the nominal gap width provided by the experimental data lead to a good prediction of the temperature. The temperature prediction is more sensitive to increasing the initial gap width, which leads to higher temperature prediction. A decrease in the initial gap size will lead to a lower prediction of the temperature but the sensitivity of the prediction to that decrease is lower than its sensitivity to the increase in the gap. In general, the initial gap size measurements will affect the whole results of the simulations and it is important to accurately consider it in a parametric analysis.

Grain size DKORN

The grain size of the fuel material is given in the experimental data between a lower and an upper limit. The Grain size parameter (DKORN) was taken as an average value between those two limits. The result of the conducted analysis shows that the nominal average grain size taken in the reference case gave a good estimate of the temperature. The temperature prediction is more sensitive to decreasing the grain size than to increasing it. Smaller grains means as well more probability of fission

gases reaching the grain boundary and with the higher temperature leading to interlinking between fission gas bubbles. This leads to a higher FGR predicted by the code for the lower limit of the grain size.

DENBUP
It is defined as the cut off burn-up above which the densification halts. Fuel densification is important to consider and if it was not, the temperature will be seriously under-predicted to more than 200^0C. If no densification is considered, the gap size will be smaller than when it is considered at the same LHR conditions. This will enhance the conduction through the gap and will lead to significant under prediction. The reference case used here was DENBUP=10000 MWD/tHM. As a sort of sensitivity study, DENBUP was decreased to 3000 MWD/tHM. The densification overall effect was no different from the case when a higher value was taken. Therefore being conservative and taking higher value of densification cutoff will not result in severe effect on the evolution of the temperature temporal profile.

DENPOR
It is defined as a parameter representing the porosity of the fuel rod at the end of sintering. Uncertainties related to the prediction of this parameter should be investigated. There is an uncertainty of around 50% of the data used to fit an equation for this parameter. This equation was verified against the IFA 597 experiment using TU. The nominal data obtained by the equation predicted the best fit of the temperature. The sensitivity to DENPOR parameter is higher with the increase of the parameter while it is less sensitive to its decrease which is consistent with the experimental data upon which DENPOR correlation was fitted.

5.5 Radial analysis

In order to investigate the radial profile of the thermal conductivity during IFA597.4/.5, two points in time were taken at approximately 5 MWD/kgU and 24 MWD/kgU. These points were chosen based on the average burn-up value. The points in time at which these values of burn-ups were reached varied between rod-10 and rod-11 due to the different locations they held in the rig. The exact values of the burn-ups and times can be found in *Table 5-6*.

Those time points were chosen to result in a broad analysis that captures relatively low and medium values of burn-up hence, to capture the influence of this parameter.
The thermal conductivities in both cases were plotted as functions of the temperature profile of the rods at these specific moments taking into consideration the radial variation of the rod conditions (temperature, local burn-up, porosity). O/M ratio did not vary during the experiment. It did not vary also during modelling when a test flight was made to investigate if the code will detect sensible variation of that parameter. This was investigated by choosing the option IOXIRE=1 which allows modelling changes of O/M ratio.
A radial sensitivity analysis was performed to investigate variation between thermal conductivity values and how it would affect the temperature profile of the rods. Not only TU correlations were investigated in this study, also open literature correlations were investigated. The values of thermal conductivities based on TU correlations were captured directly from the code. The open literature correlations were calculated on the discretized radial nodes based on the temperature, plutonium content and porosity radial profiles. Performing this analysis would not result in obtaining a temperature profile by open literature correlations but can give a qualitative idea about how they would predict or deviate from TU correlations if they were applied in TU code. After that, those correlations were compared to experimental data (they were available at zero burn-up only but should

still be comparable with the results at this low burn-up) to check their compatibility with them. The results of these investigations are summarized in the next subsections.

	Rod-10 (Solid pellets)	**Rod-11 (Hollow pellets)**
Axial position	Peak position (section 3)	Peak position (section 2)
Time-1 (hr)	1757.44	1692.6
Burn-up (MWD/kgU)	5.0	5.11
Time-2 (hr)	12633	11647
Burn-up (MWD/kgU)	23.99	23.986

Table 5-6 IFA-597, summary of radial analysis main data.

5.5.1 IFA597.4 Radial analysis (5 MWD/kgU)

The temperature profile at an average burn-up of 5 MWD/kgU at the peak power location in the rods was plotted as function of fuel pin radius, *Figure 5-26*. The temperature varies between 1238 ^{0}C at the center and 490 ^{0}C at the periphery of the rod. Only Wiesenack's correlations (COND-34) deviated from the rest of the correlations and tended to predict a lower temperature profile in most radial regions of the rod.

The thermal conductivities as functions of temperature are given in *Figure 5-27* and *Figure 5-28*. The figures include the correlations given in section 3.2 and experimental data obtained for un-irradiated MOX of similar design (to IFA-597 rods). Regarding open literature correlations, it can be seen that MATPRO and MARTIN's correlations resulted in highly over predicted thermal conductivities. Comethè correlation predicted the thermal conductivity slightly higher than Wiesenck. Baron-Hervè-95 correlation predicts the thermal conductivity similarly to COND34 at the peripheries and center of the rod. In the mid-section of the rod the profile is similar to COND32. In general, one expects it to predict a temperature profile higher than COND34 but lower than the others.

The experimental data-points fit the TU correlations, the Baron-Hervè and the Comethè correlations.

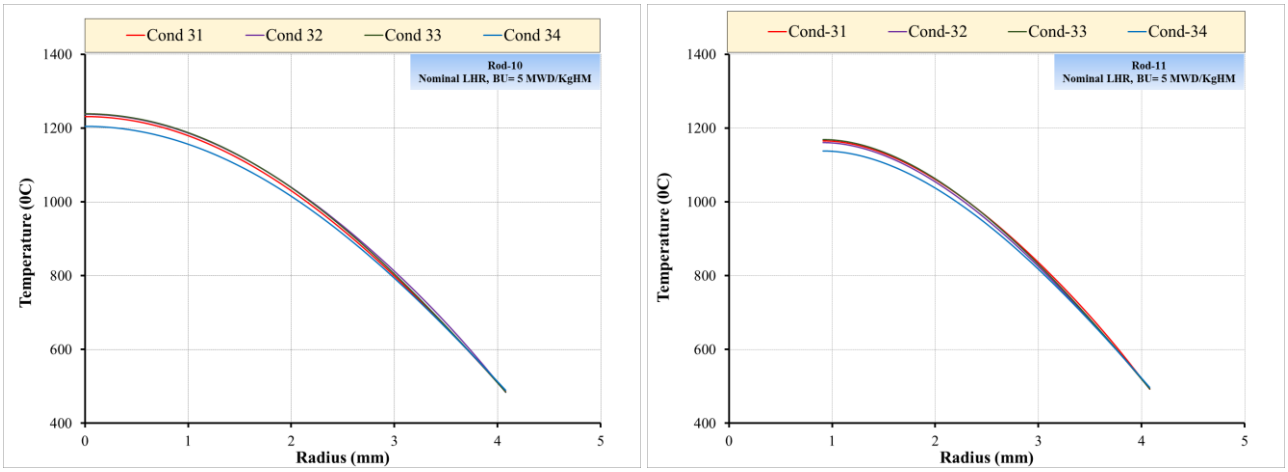

Solid rod (rod-10) *Hollow rod (rod-11)*

Figure 5-26 IFA-597, temperature radial profile at 5MWd/kgHM as function of the conductivity correlation adopted.

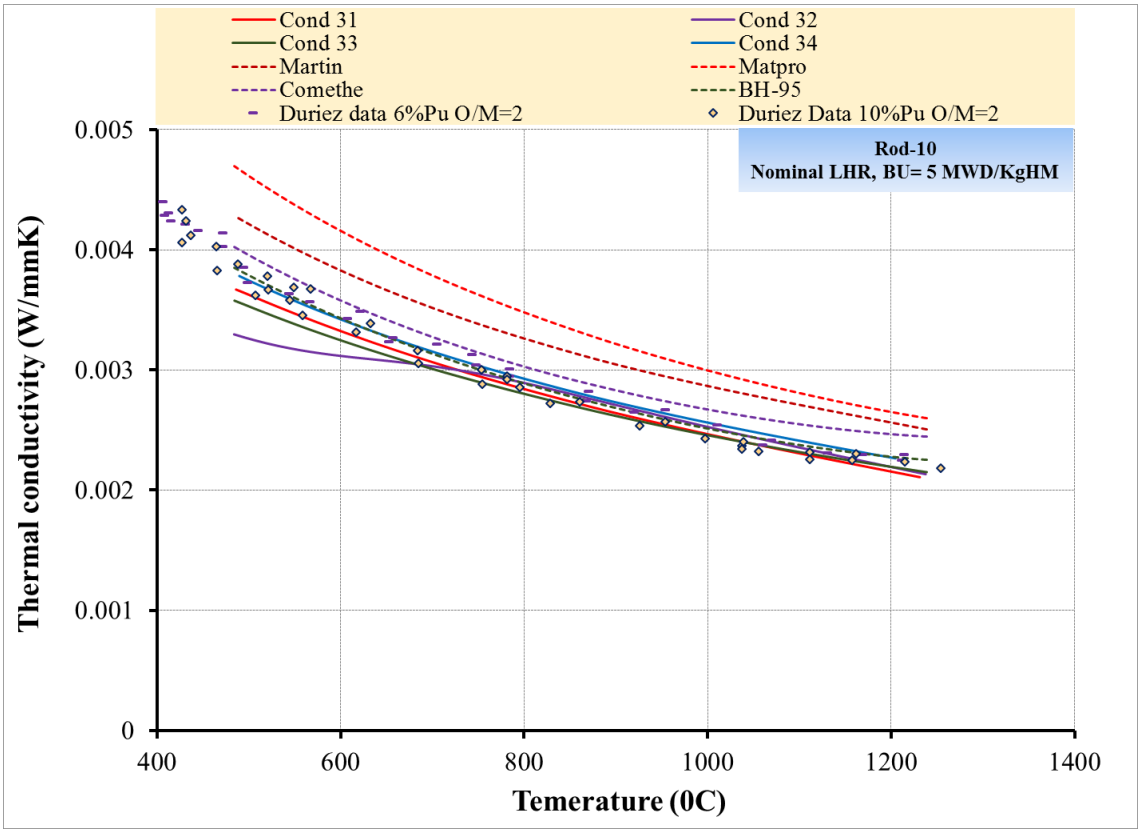

Figure 5-27 IFA-597 at 5 MWd/kgHM, thermal conductivity profiles when applied to rod-10, comparison with open literature correlations and experimental data.

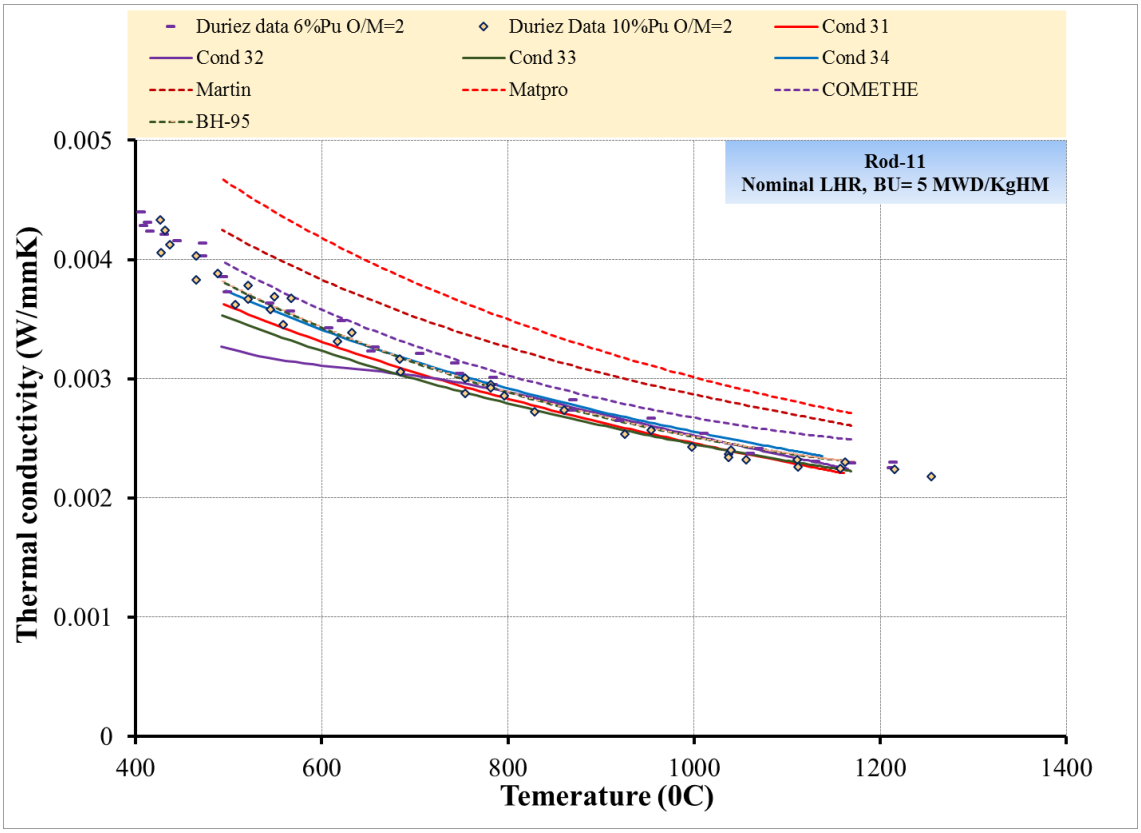

Figure 5-28 IFA-597 at 5MWd/kgHM, thermal conductivity profiles when applied to rod-11, comparison with open literature correlations and experimental data.

5.5.2 IFA597.5 Radial analysis (24 MWD/kgU)

The temperature profile of the solid rod lies between around 800 ^{0}C at the center and around 420 ^{0}C at the periphery of the rod (*Figure 5-29*). The correlation of Wiesenack (COND 34) predicted a temperature that is around 65 ^{0}C lower than the others. The temperature profile predicted by the other correlations have more variability than the previous case but they are still compatible with each others.

The thermal conductivities as functions of temperature are given in *Figure 5-30* and *Figure 5-31*. The figures include the correlations given in section 3.2.
Comparing the thermal conductivities, it can be seen that the studied correlations show greater variability than at 5 MWd/kgU. TU correlations consider burn-up as a factor and the thermal conductivity will degrade with burn-up. It can be seen that TU predicts the lowest thermal conductivity compared to open literature due to the burn-up effect. Open literature correlations are higher and will definitely predict a lower temperature profile. The centerline temperature predicted by TU correlations matches the experimental measurement during IFA597. Therefore, it is an indication that burn-up is an important factor that cannot be neglected when modelling thermal conductivities of MOX.

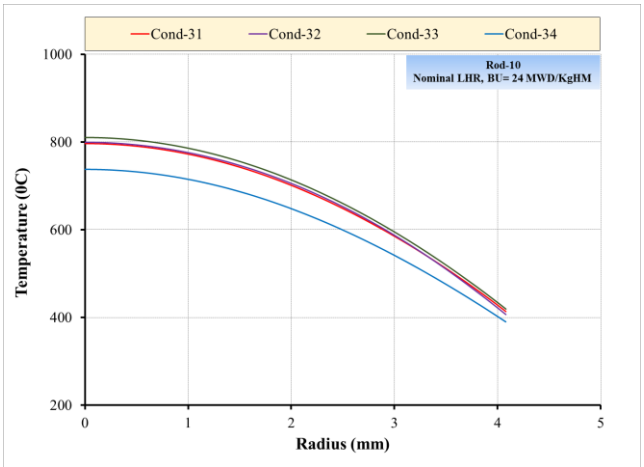

Solid rod (rod-10)

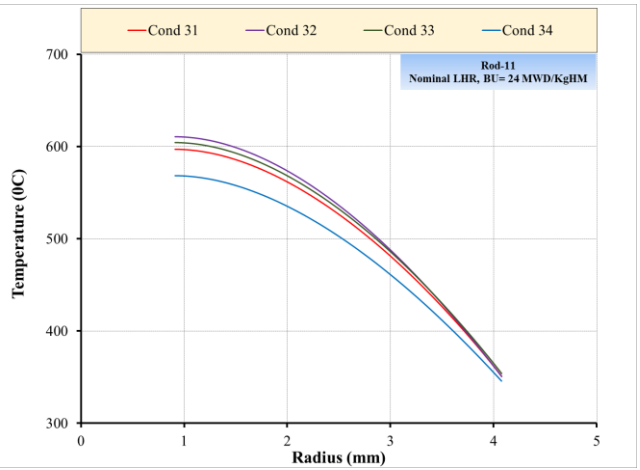

Hollow rod (rod-11)

Figure 5-29 IFA-597, temperature radial profile at 24MWd/kgHM as function of the conductivity correlation adopted.

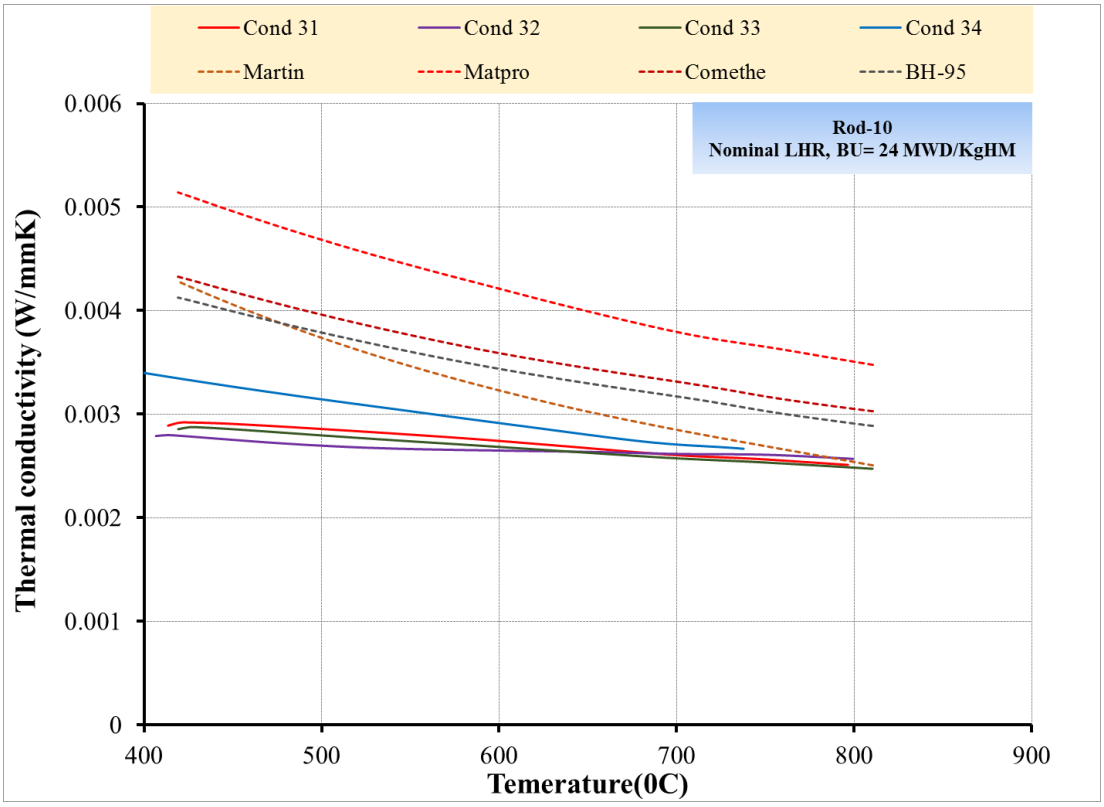

Figure 5-30 IFA-597 at 24 MWd/kgHM, thermal conductivity profiles when applied to rod-10, comparison with open literature correlations and experimental data.

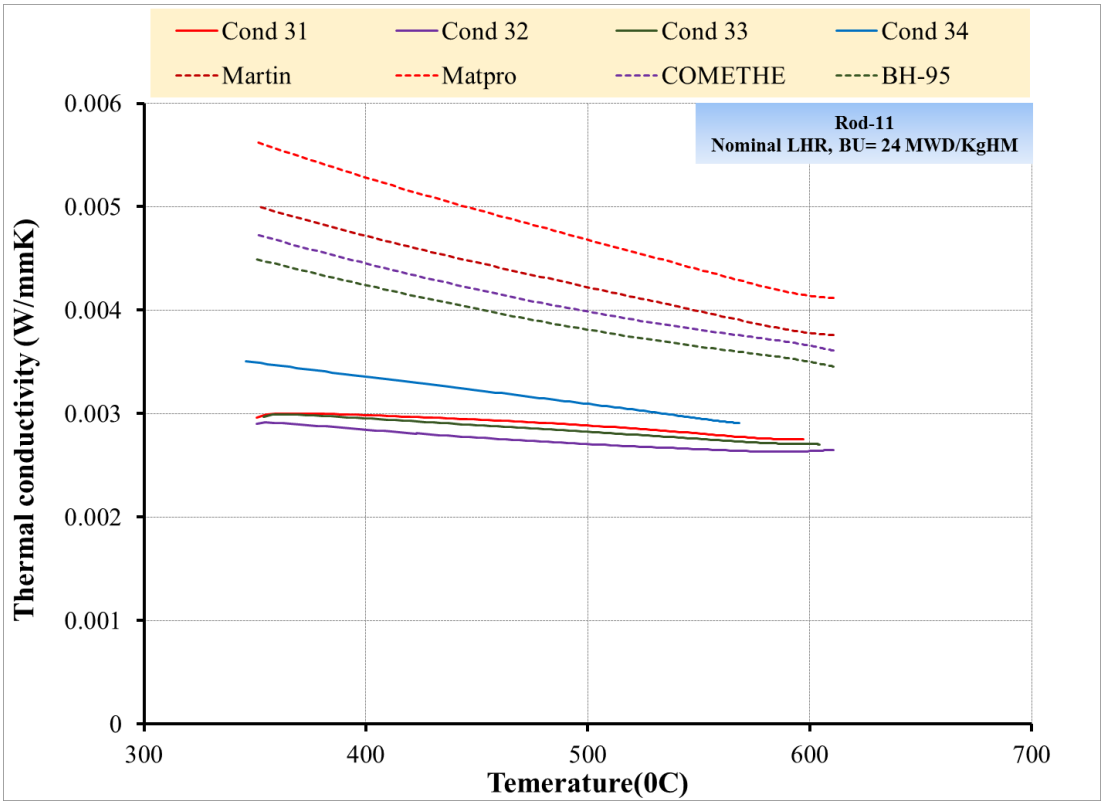

Figure 5-31 IFA-597 at 24 MWd/kgHM, thermal conductivity profiles when applied to rod-11, comparison with open literature correlations and experimental data.

.

6 Analysis of FR MOX: HEDL P-19 experiment

6.1 Description of the experiment

6.1.1 Background and objective of the experiment

The purpose of the HEDL P-19 experiment was to investigate the effect of as-fabricated fuel to cladding gap from 0.086 to 0.25 mm on the linear power needed to cause incipient melting Q'm.[3] The normalized linear power to the peak is plotted in *Figure 6-1*. The MOX fuel used was 25% PuO_2-75%UO_2 rods. The experiment consisted of a subassembly containing nineteen encapsulated pins representative of the Fast Flux Test Facility (FFTF) fuel design. Sixteen of them were fresh fuel pins, three pins were pre-irradiated before the experiment. The cladding outer diameter of half of the fresh pins is 5.84 mm. The other half is 6.35 mm. The pins were filled with pure helium and cladded with 316 stainless steel (20% cold worked). The main design data can be found in Table 6-1.

The experiment aimed to simulate fast start-up situations of FBR. The power history of the P-19 experiment is plotted in *Figure 6-2*. The experiment began with a slow increase of power to a pre-determined steady state level. This steady state power was then kept for an hour after which the power was rapidly ramped with a 15% increase. This higher power was kept for 10 minutes to test the power resulting in fuel melting. The reactor was then scrammed to quench the fuel structure so that further neutron radio-graphical analysis will be informative. This radio-graphical investigation was aimed at determining if melting occurred inside the rods and the melting heights in the rods that propagated melting. The radio-graphical analysis confirmed no partial melting of any pin with cladding outer diameter of 5.84 mm with gap width of less than 0.14 mm. The rest of the pins developed melting regions with different extents.

Transverse fuel ceramographic samples were used to measure fuel restructuring radii, residual gap widths and radial extent of melting at the peak power position. There is uncertainty regarding the power to melt due to the uncertainty of the effect of the relocated molten fuel on the local power. Also, the central void formation is uncertain due to melting that obliterated the formed central void. Since most of these peak power regions operated at much higher powers than Q'm, melting is extensive even in adjacent fuel.[26] The axial extents of melting, as determined from longitudinal ceramographic sections, offered the best data for determining Q'm since these sections were actually located where incipient melting occurred and experienced the least power variation due to molten fuel relocation. The main data for the two rods of interest in this analysis (P-19-2 & P-19-5) from PIE are given in *Table 6-2* and *Table 6-3*.

Rod N°		1	2	3	4	5	6	7	8	9	10	11	12	13	14	15	16
Rod Id.		P 19 2	P 19 3R	P 19 5	P 19 6	P 19 7R	P 19 8	P 19 13	P 19 20	P 19 24R	P 19 25R	P 19 26R	P 19 27R	P 19 28	P 19 30	P 19 33	P 19 35
Gap µm		99	127	72.5	49.5	79	122	99	123	127	101.5	76	51	43	89	62.5	91.5
%TD	90.75	X		X	X		X	X	X							X	X
	92.40		X			X				X	X	X	X	X	X		
Clad OD mm	5.84	X		X	X		X	X	X							X	X
	6.35		X			X				X	X	X	X	X	X		
Fuel		25% PUO_2 - 75% UO_2															
Cladding		316 stainless steel (20% cold worked)															
Filling gas		98% He at 1 bar															
O/M		1.96															
Active length		343 mm															
Na inlet temp.		371 °C															
Max LHR kW/m		54.5	64	56.1	56.1	66.6	53.8	54.5	54.1	64.6	66	66.9	66.9	67.9	65.6	55.1	54.1

Table 6-1 HEDL P-19, design data. [3]

Rod Id	Peak Power [kW/m]	EXP Bottom axial Melting extent			EXP Top axial Melting extent		
		Location [cm]	Local power [kW/m]	Coolant Temp [°C]	Location [cm]	Local power [kW/m]	Coolant Temp [°C]
P-19-2	54.5	72.1	51.8	386	248.4	50.5	426
P-19-5	56.1	--	--	--	--	--	--

Table 6-2 HEDL P-19, axial extension of fuel melting at the end of the experiment. [3]

Rod Id	Id	Location [cm]	Central void radii [mm]	Molten radii [mm]	Columnar grain radii [mm]	Diametric gap [mm]
P-19-2	**1**	15.5	0.64	0.94	1.80	0.142
	2	19.1	0.58	0.79	1.73	0.142
P-19-5	**1**	15.5	0.46	0.00	1.68	0.102
	2	18.5	0.48	0.00	1.65	0.147
	3	20.3	0.43	0.00	1.55	0.102
	4	21.6	0.46	0.00	1.60	0.122

Table 6-3 HEDL P-19, measurements of central void, columnar grain radius and TD at pellet center at the end of the experiment. [3]

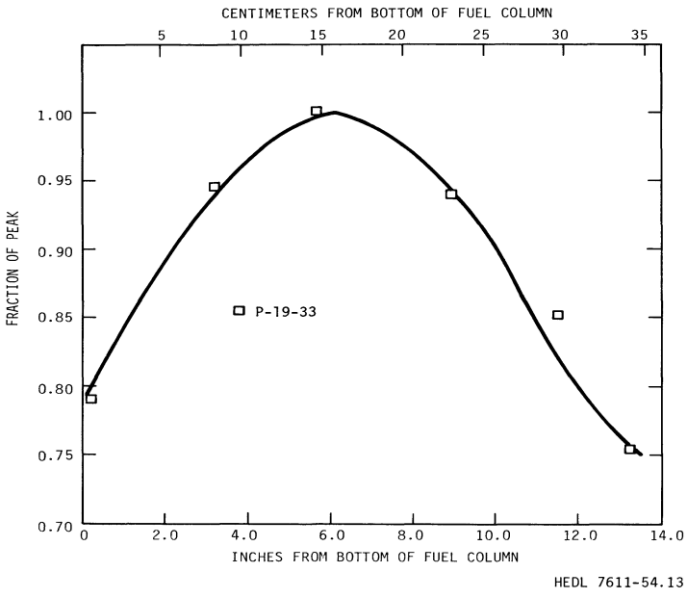

Figure 6-1 HEDL P-19, pin power axial profile.[3]

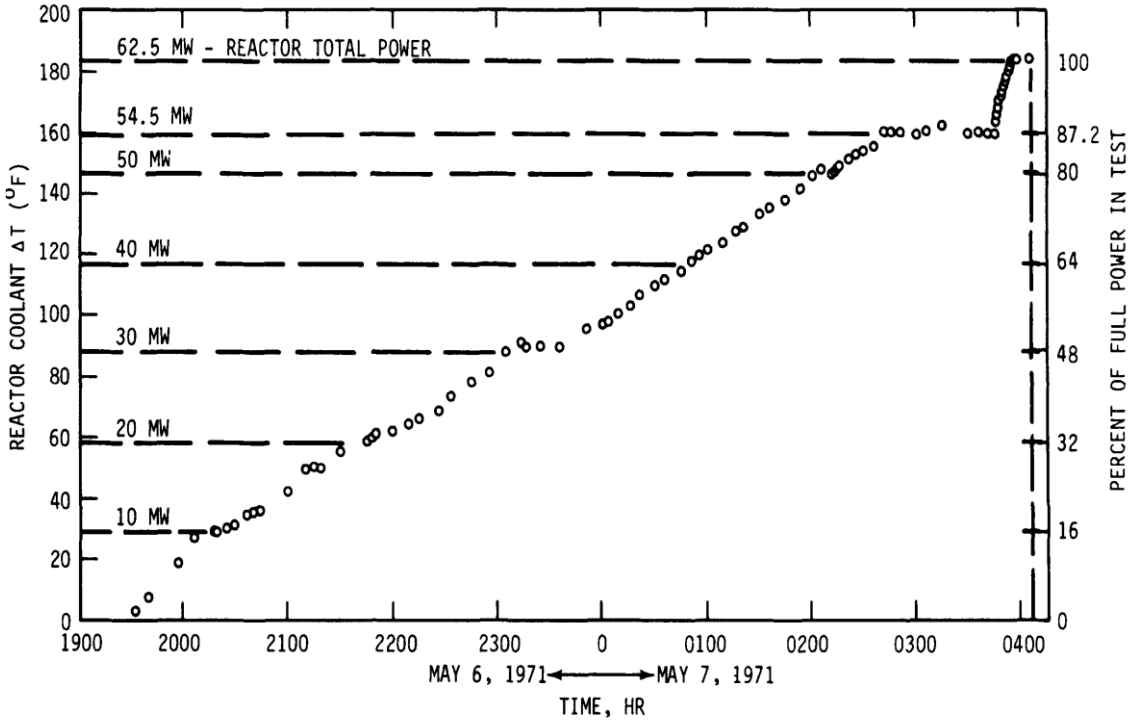

Figure 6-2 HEDL P-19, EBR-II power history during the experiment.[3]

6.1.2 Experimental breeder reactor #2 (EBR-II)

EBR-II is a sodium cooled reactor that was designed and operated by Argonne National Laboratory. It was shut down in 1994. The reactor was operated with thermal power of 62.5 MW_t (20 MWe). The reactor was intended as a FBR accompanied with an on-site reprocessing facility. During the first five years of the reactor life, (1964-1969), 35000 fuel elements were reprocessed. The reactor was then transformed to a burner and its aim was shifted to testing fuel materials for future sustainable LMFBR. The reactor operated as an integral fast reactor prototype that cost more than US$32 millions starting from 1964 to 1994. 30000 irradiation tests took place in the reactor during its 30 years lifetime. Two billion KWh_e were generated from the reactor that were used as electricity and heat source for ANL facilities.[27]

The pool type design of the reactor assured the passively safe reactor concept. In case of failure of scramming the reactor by the operator, the reactor will shut down spontaneously without external assistance. That helped developing many safety tests that involved loss of flow accidents. The accidents were simulated with normal shutdown systems disabled and no excessive temperatures were reached.[28]

A schematic diagram of the plant system is sketched in *Figure 6-3.* The primary system contains the reactor system, the sodium coolant primary cycle, and the heat removal systems. They dwell in the containment building designed to accommodate any release during transient or accident situations. The fuel handling system was submerged in Sodium contained in the primary tank. The sodium is withdrawn from the bulk sodium and pumped into the reactor to flow upwards in the reactor through the subassemblies cooling the fuel and the blanket. Two lines are used to cool the reactor. One high-pressure line for the subassemblies and the inner blanket side. Another low-pressure line is used to cool the outer side of the blanket. Afterwards, Sodium is driven to a heat exchanger to be cooled and returned back to the Sodium bulk. The reactor is geometrically close-packed due to the existence of single size of the subassemblies. The hexagonal subassembly tube was 2.290 inches across external

flats of 0.040-inch wall thickness. The subassemblies were spaced on a triangular pitch of 2.320-inch center distance.[29]

The secondary system consists of four main components, Sodium circulating pump, heat exchanger, steam super-heater and steam evaporator. It is used as a mediator containing non-radioactive Sodium that transfers heat from radioactive Sodium on the primary side to a steam system. Flow rate on the secondary side is 2.5 x 10^6 pounds per hour. Super-heated steam is driven to a turbine at 850 ^{0}F with a rate of 1250 pounds per inch^2.

The Power Plant contained the turbine generator and associated equipment and the control room for the reactor and power cycle. It was interconnected to the Reactor Plant by means of one air lock to permit personnel access to the Reactor Plant. The building was of conventional construction. The Fuel Cycle Facility contained two shielded cells for disassembly, processing, and manufacture of fuel elements and subassemblies, and supporting facilities for these operations. It also contained the inert-gas storage facilities, the sodium equipment cleanup cell, and exhaust ventilation system and the stack for the exhaust from the Fuel Cycle Facility and Reactor Plant.

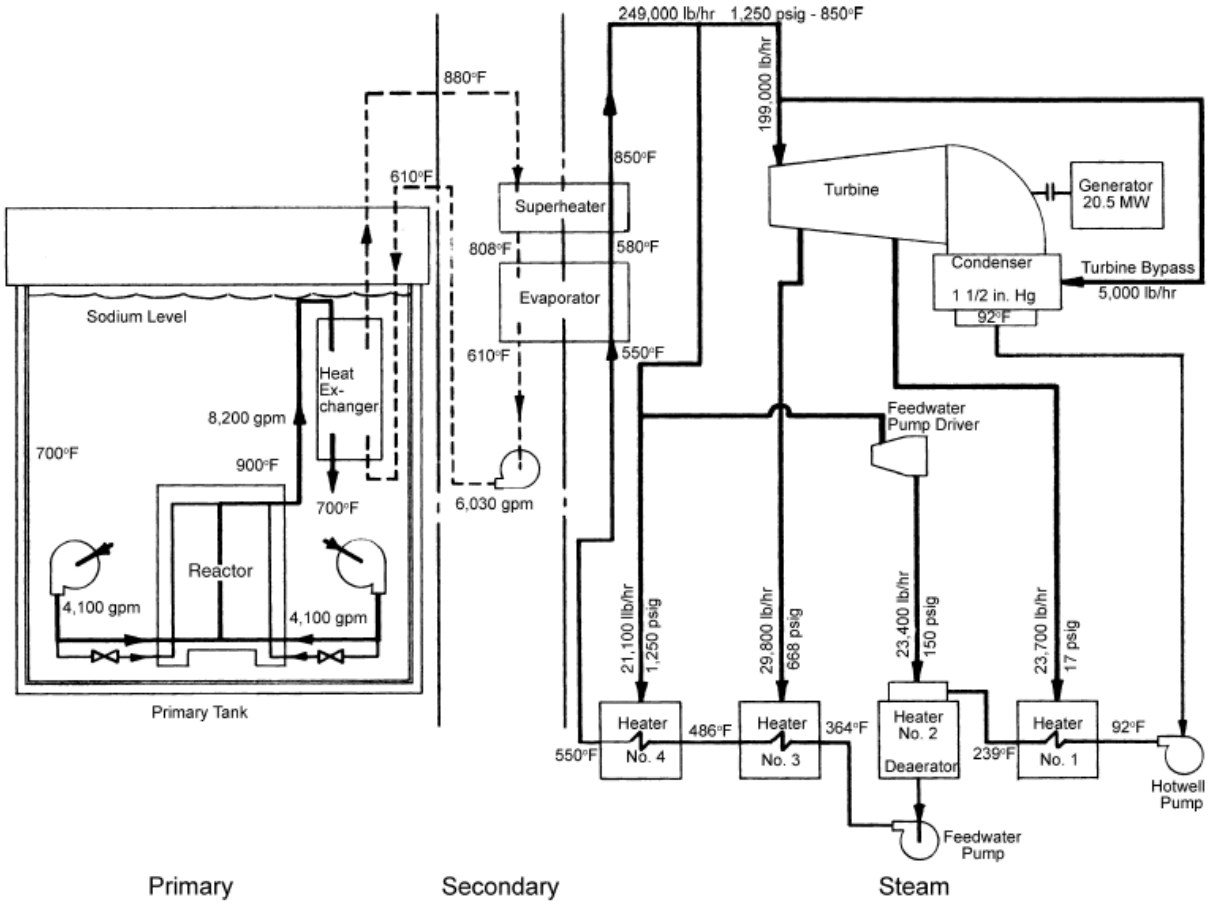

Figure 6-3 Schematic diagram of EBR-II plant. [29]

6.2 Modelling HEDL P-19 with TU

6.2.1 Development of TU input file

The fuel rods were modelled using TRANSURANUS code, version "v1m1j12", with the deterministic option, steady state thermal and mechanical analysis. The version of the manual is "v1m1j12". The boundary conditions were prepared using a program prepared using PERL language. An input deck was prepared according to the information available in the manual of the code. Most of the models used in the reference analysis were the standard recommended models by the code developers. Some deviations occur when needed. For EBR-II the melting model used is the one used for Uranium nitride fuel MODFUEL(16)=15. This is due to the fact that this model gives the melting temperature as a constant value (2760^0C) which fits better with the conditions of P-19 experiment. Other melting temperature models that use the plutonium content, O/M and burn-up will be later investigated as a sort of sensitivity analysis in section 6.4.3. The average grain diameter was assumed to be 22 μm while the upper plenum was taken to be 300 mm (comparable to the active length of the rod). The main models that were expected to affect the measured parameters of the rods and the prediction of fuel temperature are summarized in *Table 6-4*. Most of the models used in this analysis are the ones recommended by TU. For various reasons other models were chosen. In section 6.4, a sensitivity analysis of the results to some of the models or correlations that were not chosen in the reference case will be presented.

HEDL P-19 Reference input decks			
Parameter	**Reference Option**	**Description**	**Other options**
Fuel conductivity	Correlation 31 (recommended)	Standard correlation of the thermal conductivity of MOX fuel (best estimate) according to Van Uffelen and Schubert, based on experimental data obtained by Duriez et al. for fresh MOX fuel and laser flash measurements of irradiated MOX fuel at ITU. It is extended by an ambipolar term recommended by Ronchi et al.	32,33, 34,35
Pellet fragment relocation	Model ireloc 8	Modified FRAPCON-3 model. It considers the as fabricated gap size, the burn-up and the linear heat rate.	2, 3, 4, 5, 6
Fuel grain growth	Model igrnsz 1 (recommended)	Grain growth model of Ainscough and Olsen. It computes the grain radius increase as function of the fuel local temperature assuming a maximum grain radius for each temperature.	--
Fuel densification	Model idensi 2 (recommended)	Empirical model for LWR and FBR. This model needs the input of the minimum porosity DENPOR at the end of thermal and irradiation induced densification and the time constant DENBUP (burn-up in MWd/tU, at which irradiation induced densification is terminated).	3, 7
Gap conductivity	Model ihgap 0 (recommended)	Standard Option: gas Bonding thermal conductivity of mixture according to Lindsay and Bromley. Accommodation coefficients are taken into account.	1, 3, 4,5
Solidus and Liquidus Melting Temperatures	***Correlation 15***	The correlation is recommended in the Gmelin handbook. It is used for Nitride and mixed nitride fuel $T_{Liquidus}$ =3035 K (2762^0C).	10,11,13

Table 6-4 Simulation of HEDL P-19, summary of models and correlations that might affect the prediction of thermal conductivity of the rods.

6.2.2 Boundary conditions

The boundary conditions used are:

- Linear heat rate at 17 axial position;
- Fast neutron flux (>1 MeV);
- Sodium bulk Coolant temperature
- Coolant pressure.
- Heat transfer coefficient at the cladding outer surface

Linear heat rate (LHR) increase/decrease with a rate of 6 (kW/m.h) for any change between different values of LHR. This transition rate and the time needed for the LHR to be changed is calculated based on the LHR in the peak position. During the ramp the rate of the change of the power was taken as 500 KW/m.h, this is typically used during power ramp tests. The linear heat rate was calculated at 17 positions of the rods. The axial positions of the calculations can be seen in *Table 6-5*. Those positions were chosen based on the power profile that can be seen in *Figure 6-1*.

The fast neutron flux is given as a constant rate of $1x10^{14}$ n/cm^2.s. The coolant pressure is given as a constant over the whole period of the experiment with a value of 0.1 MPa (open pool condition). The coolant temperature is given on the same axial positions of the linear power and its evolution is calculated based on the experimental report.

The trend of the linear power and coolant temperature applied to rod P19-2 can be seen, respectively, in *Figure 6-4* and *Figure 6-5.* The active part of the fuel was considered in this study. The rods are divided into a number of m_3 slices that are determined by the number of boundary condition points given in the experiment data. The sectional option was chosen in this analysis. Thus, the total number of points taken is m_3 +1.

Axial node	Position-Rod (mm)
1	0
2	18.533
3	33.7837
4	54.1279
5	73.9818
6	92.3147
7	110.668
8	126.489
9	145.392
10	163.815
11	180.717
12	211.498
13	238.207
14	255.199
15	275.263
16	296.348
17	335.775

Table 6-5 Simulation of HEDL P-19, axial discretization of the fuel rods.

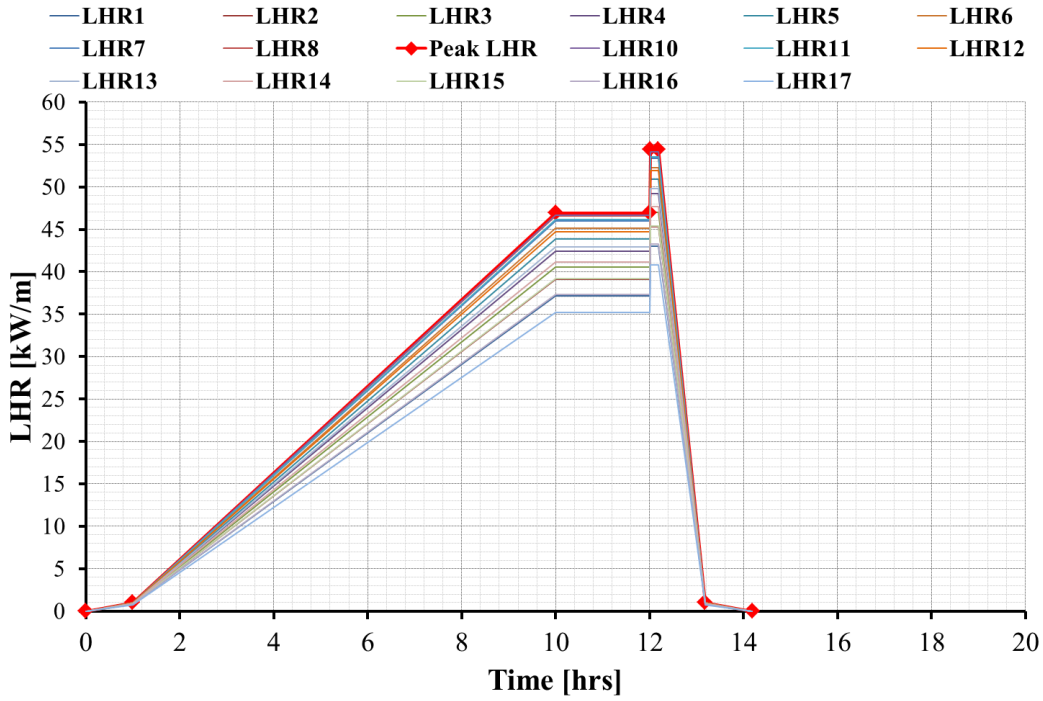

Figure 6-4 Simulation of HEDL P-19, rod P19-2, LHR at 17 axial elevations.

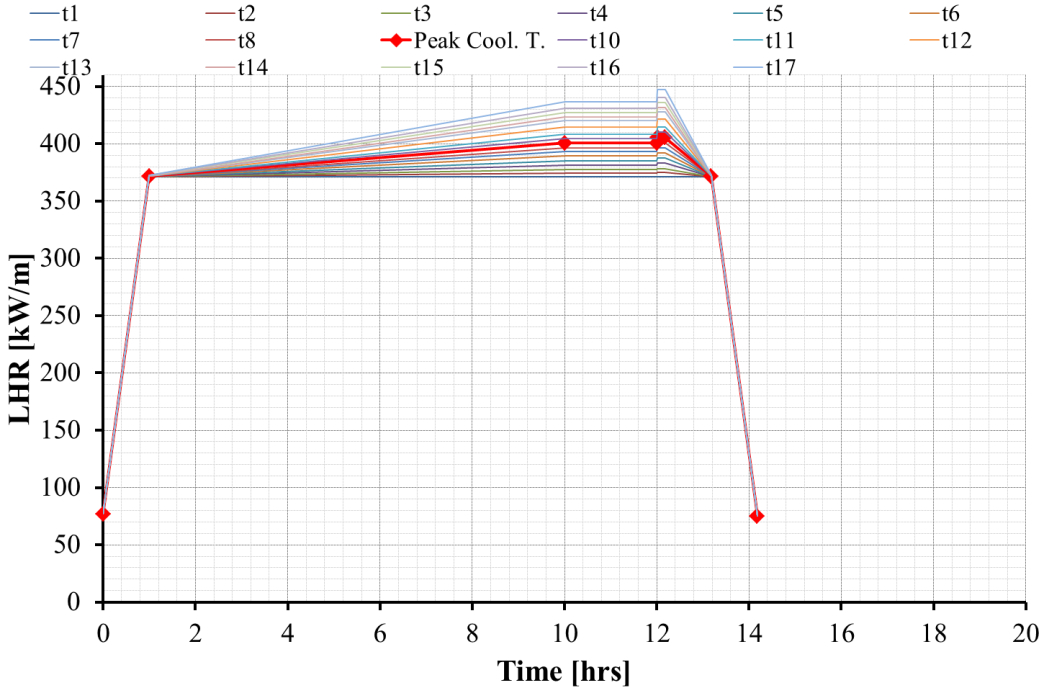

Figure 6-5 Simulation of HEDL P-19, rod P19-2, coolant temperature at 17 axial elevations.

6.3 Reference analysis of HEDL P-19 rods

6.3.1 Temperature prediction

The evolution of the centerline fuel temperature in the peak power position is given in *Figure 6-6* and *Figure 6-7*. The temperature profile increases gradually with the LHR up to 10 hours. At that time the LHR and temperature are kept constant for two hours. During that time it can be seen that the code

predicted that the maximum temperature in the rods was almost equal to the melting temperature marked by the horizontal line. This means that any slight increase in LHR will lead to the beginning of melting of both rods. That was predicted for both rods by the code as the LHR increases to a level where melting can happen, both rods temperatures increase beyond melting temperatures up to 3220 ^{0}C for rod P-12-2 and a lower temperature 3122 ^{0}C for rod P-12-5. Both temperatures are predicted at the Peak LHR positions. Since this experiment was a melting experiment, there was no temperature measurement attempted. Therefore, there is no direct comparison between the temperature predicted by the code and the experiment, rather integral comparison of the melting heights is done here. Neutron radiography showed that rod P-12-5 did not suffer melting at all. This means that temperature in this rod did not exceed the melting temperature during the ramp phase of the experiment. This leads to a conclusion that the code over-predicted the temperature in that rod even though it cannot be said quantitatively to what extent the temperature was over-predicted but it is not less than 350^{0}C.

The radial temperature profile at a moment prior to the reactor scram is investigated in *Figure 6-8* and *Figure 6-9*. The radial temperature distribution is reported for the fuel and the cladding. It can be seen that for rod P-19-2, at a radius of 0.92 mm the temperature increases beyond the melting temperature. For rod P19-5, the temperature increases beyond melting point at 0.73 mm.

6.3.2 Gap width

The gap width was modelled by TU using standard relocation model (IRELOC-8, briefly introduced in section 5.4.3). The code was able to capture the experimental measurements that were done at the end of the experiment. For P-19-2 the code was able to capture the gap width at the two measurement positions, see *Figure 6-10*. For P-19-5 the code was able to capture two points out of the four measurements locations, see *Figure 6-11*. This correlation resulted in the best prediction of the gap size for the other rods in P-19 experiment with some exceptions.[26]

Assuring an accurate prediction of the gap width is a first step in assuring that the prediction of the melting height of the rod is related to the prediction of the temperature in the fuel rod itself, which is directly dependent on the MOX thermal conductivity correlations.

6.3.3 Central void

The code under-predicts the central void size at the end of the experiment (*Figure 6-12* and *Figure 6-13*). The predictions were much smaller than the experimental measurement. However, at least for rod P-19-2, only qualitative comparisons are possible since the measured void is uncertain because it is affected by the relocation of the melted fuel that would obliterate the formation of central void.

6.3.4 Columnar grains

The columnar growth of the grains did not start until the power increased more than 36 kW/m 8 hours after the beginning of the experiment. The grains kept growing up to the end of melting when the reactor was scrammed. The growth then ceased and the radius of the columnar zones remained constant for the last two hours after the scram. The code was able to predict the columnar growth with minor deviations (*Figure 6-14*, *Figure 6-15*). The predicted radius was lower than the experimental values at the end of the experiment of about 0.1-0.2 mm in radius.

6.3.5 Melting radius

The melting radius of the fuel is not given directly from TU code. Still, it can be inferred for each axial segment of the rod by checking the radial distribution of the thermal conductivity and considering the maximum radius where the thermal conductivity is constant (1.5 J/m.K) as the molten radius of that segment. That was done for the 17 segments of the fuel and plotted in *Figure 6-16* and

Figure 6-17. The code was able to accurately capture the molten radius of rod P-19-2. For P-19-5, the code predicted melting while the examination of the rod showed that it did not melt at all. This means that the melting radius should be zero.

6.3.6 Melting elevation

The prediction of the melt front is the main task in this analysis since it is the reference for which an inference about temperature prediction of TU can be made. Rod P-19-2 is analyzed in *Figure 6-18*: the melt front is over predicted when compared to the experimental examination. This longer axial melting leads us to draw a conclusion that there is an overall over prediction of the temperature inside the rod. The fact that the gap width between the fuel and the cladding is accurately predicted corroborates the idea that TU code under-predicts the fuel conductivity (at least in the high temperature regimes). The same conclusion is valid for rod P-19-5 (*Figure 6-19***)** which did not propagate melting while the code predicted considerable axial melting in the rod which can be related as well to the under prediction of the heat conduction in the rod. Even if the code behaves in a conservative way, the reasons for this over prediction of the melting heights should be thoroughly investigated by checking its sensitivity to the various phenomena that occur in the rod and the different ways of modelling them.

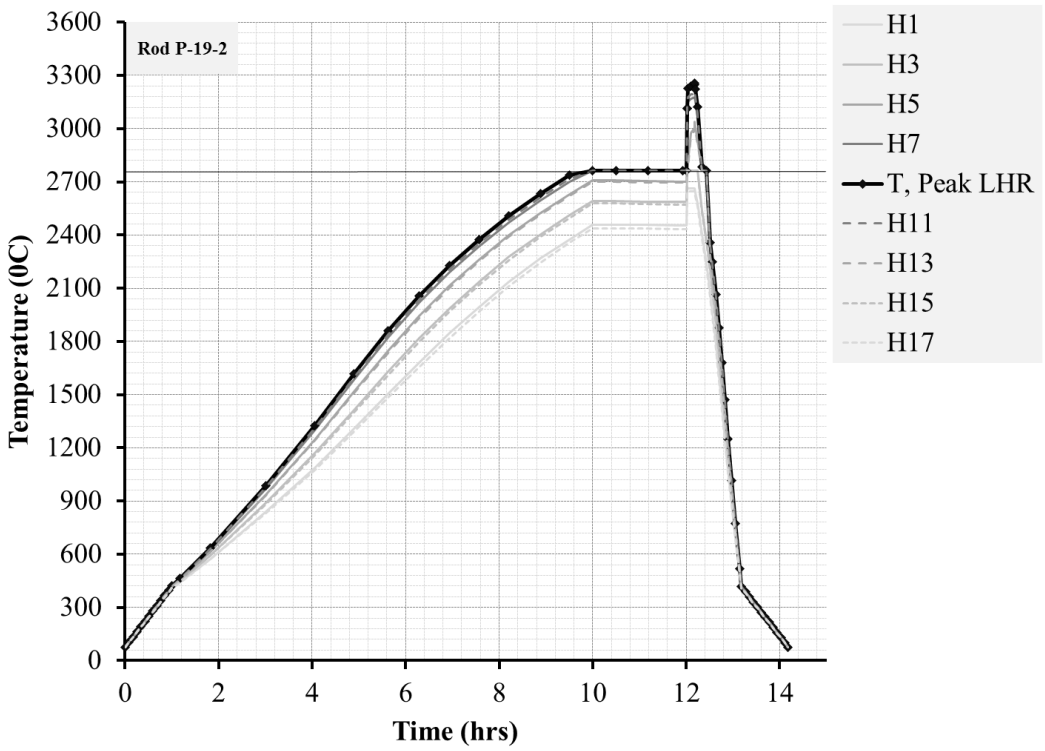

Figure 6-6 Simulation of HEDL P-19, rod P19-2, reference analysis, centreline temperature.

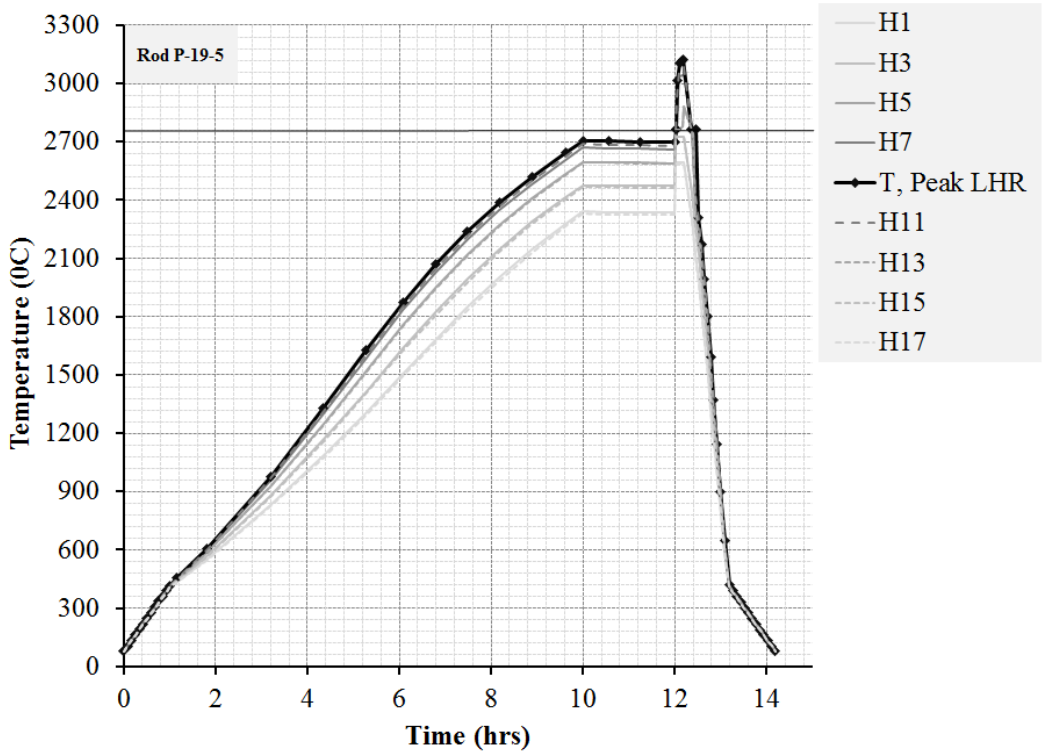

Figure 6-7 Simulation of HEDL P-19, rod P19-5, reference analysis, centreline temperature.

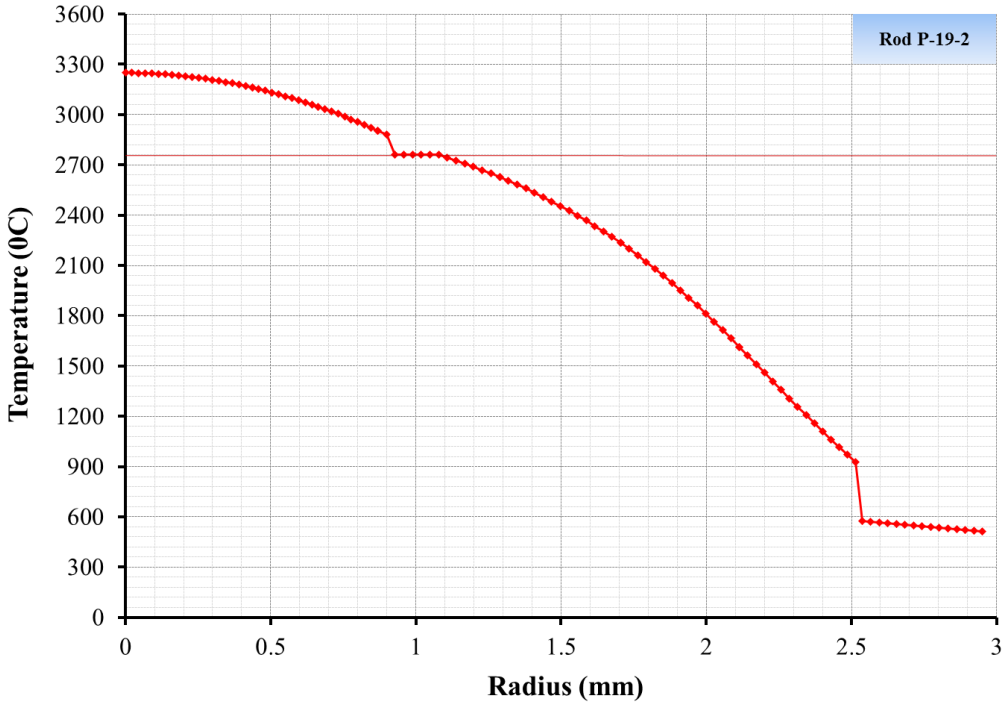

Figure 6-8 Simulation of HEDL P-19, rod P19-2, reference analysis, radial temperature profile at the end of the ramp.

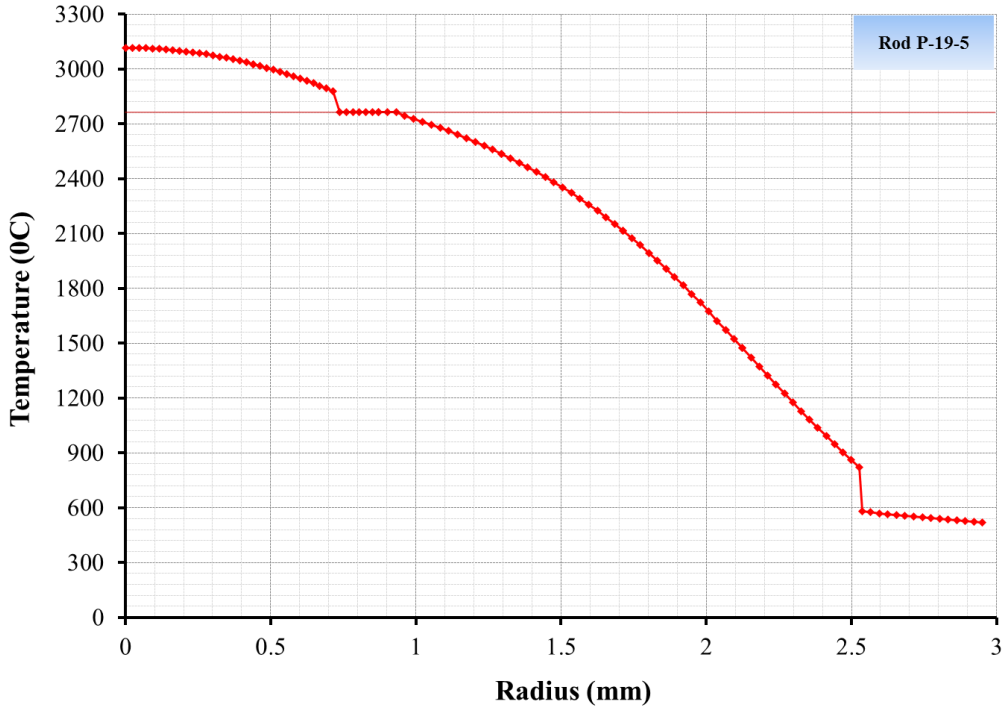

Figure 6-9 Simulation of HEDL P-19, rod P19-5, reference analysis, radial temperature profile at the end of the ramp.

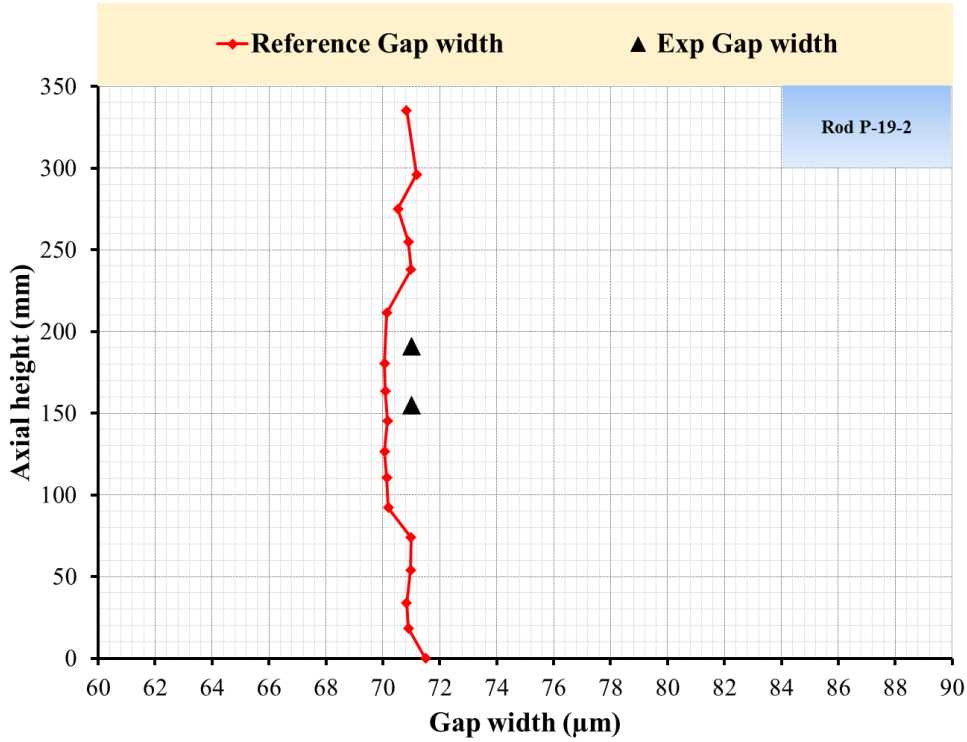

Figure 6-10 Simulation of HEDL P-19, rod P19-2, reference analysis, prediction of gap width at the end of the experiment.

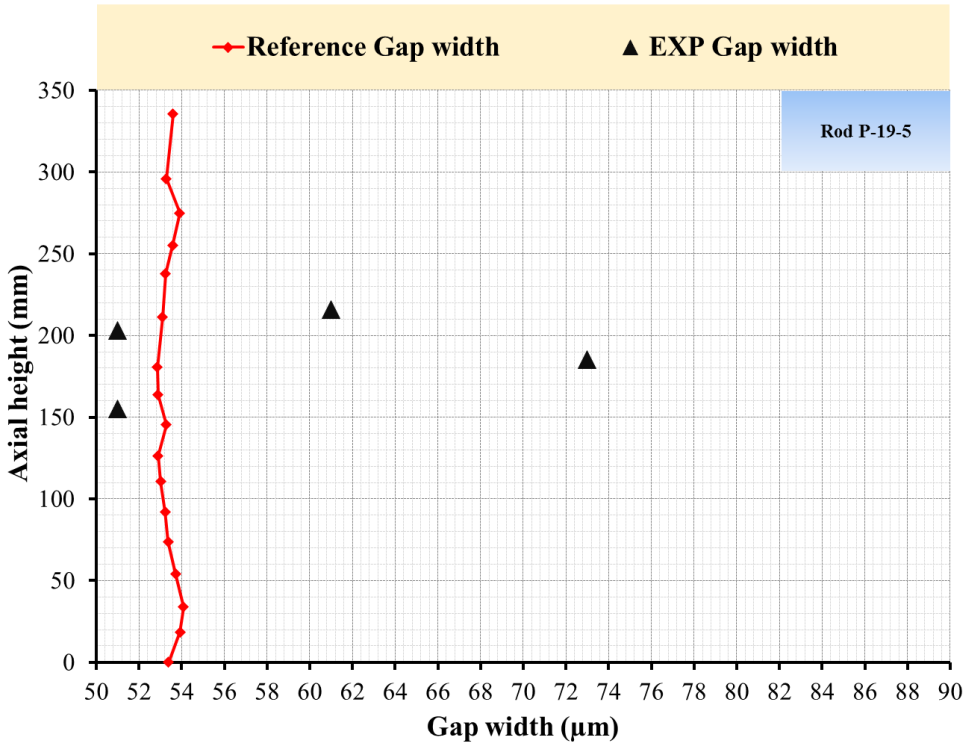

Figure 6-11 Simulation of HEDL P-19, rod P19-5, reference analysis, prediction of gap width at the end of the experiment.

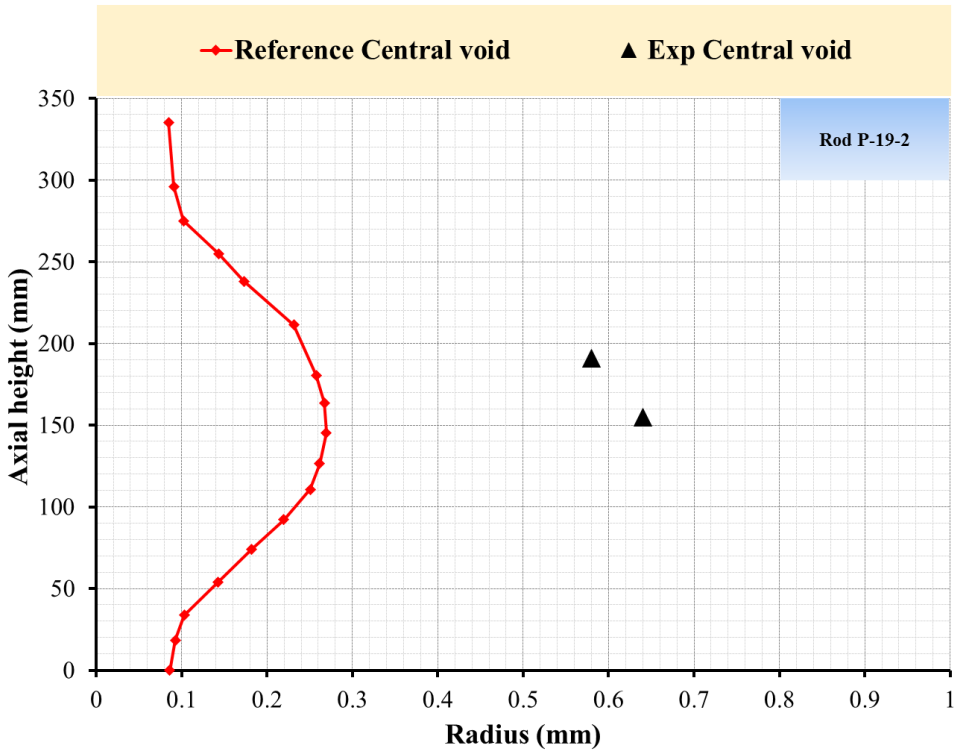

Figure 6-12 Simulation of HEDL P-19, rod P19-2, reference analysis, prediction of the central void at the end of the experiment.

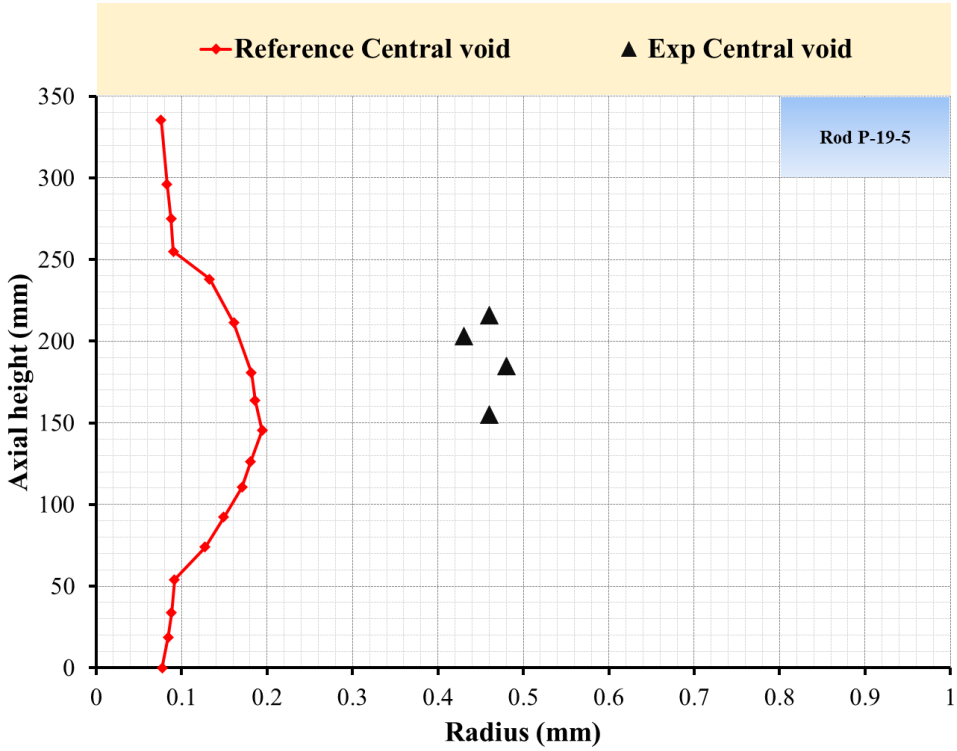

Figure 6-13 Simulation of HEDL P-19, rod P19-5, reference analysis, prediction of the central void at the end of the experiment.

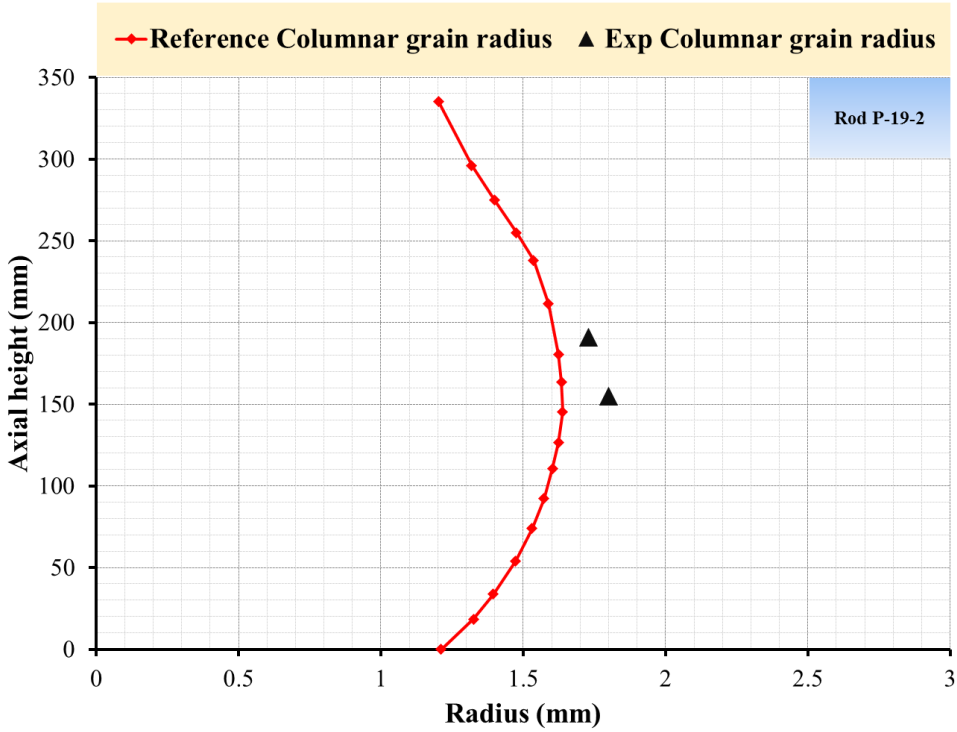

Figure 6-14 Simulation of HEDL P-19, rod P19-2, reference analysis, prediction of the columnar grain radii at the end of the experiment.

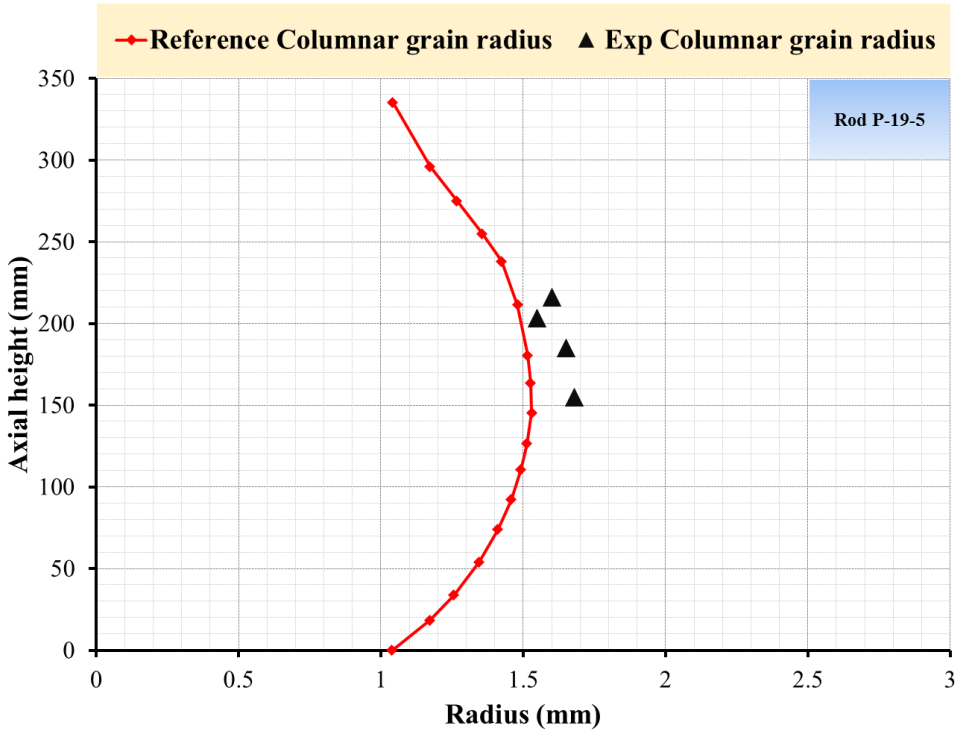

Figure 6-15 Simulation of HEDL P-19, rod P19-5, reference analysis, prediction of the columnar grain radii at the end of the experiment.

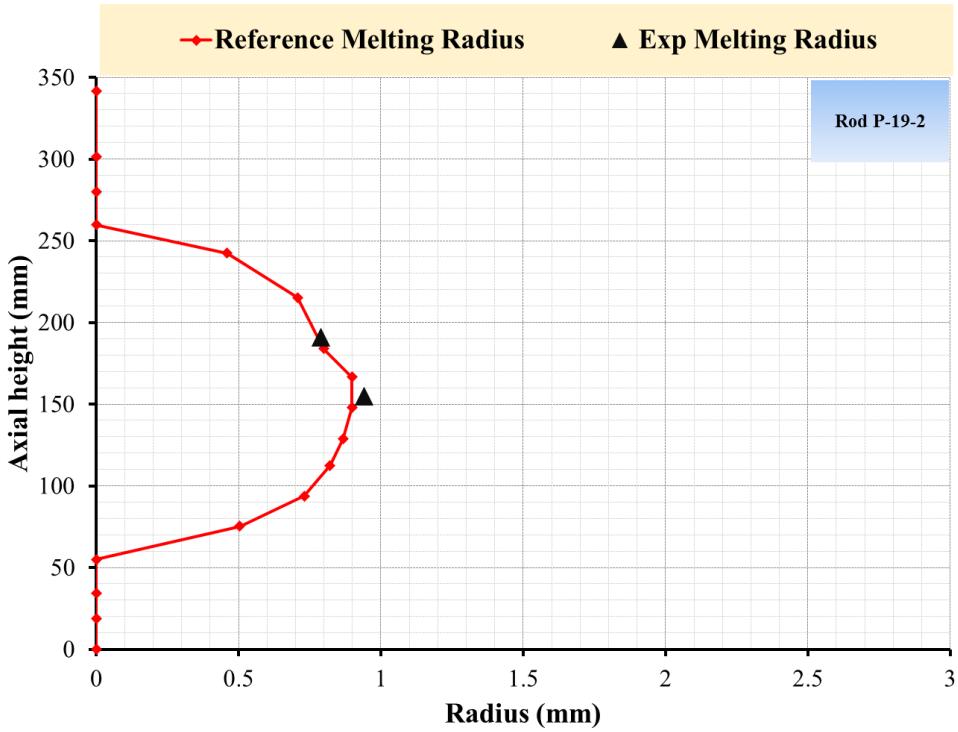

Figure 6-16 Simulation of HEDL P-19, rod P19-2, reference analysis, prediction of the melting radius.

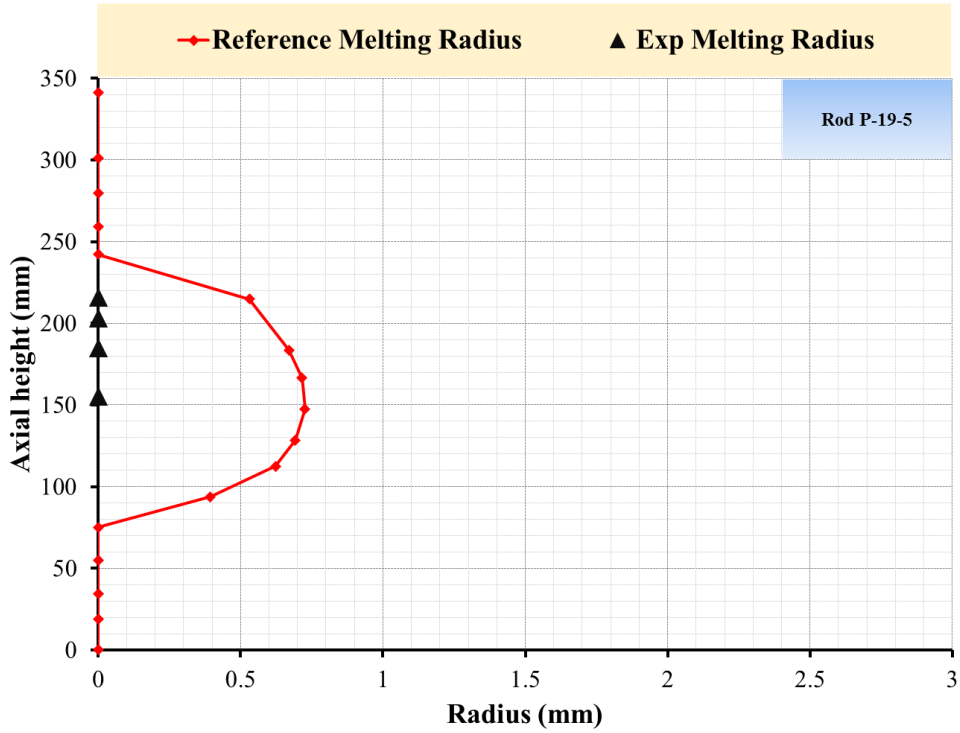

Figure 6-17 Simulation of HEDL P-19, rod P19-5, reference analysis, prediction of the melting radius.

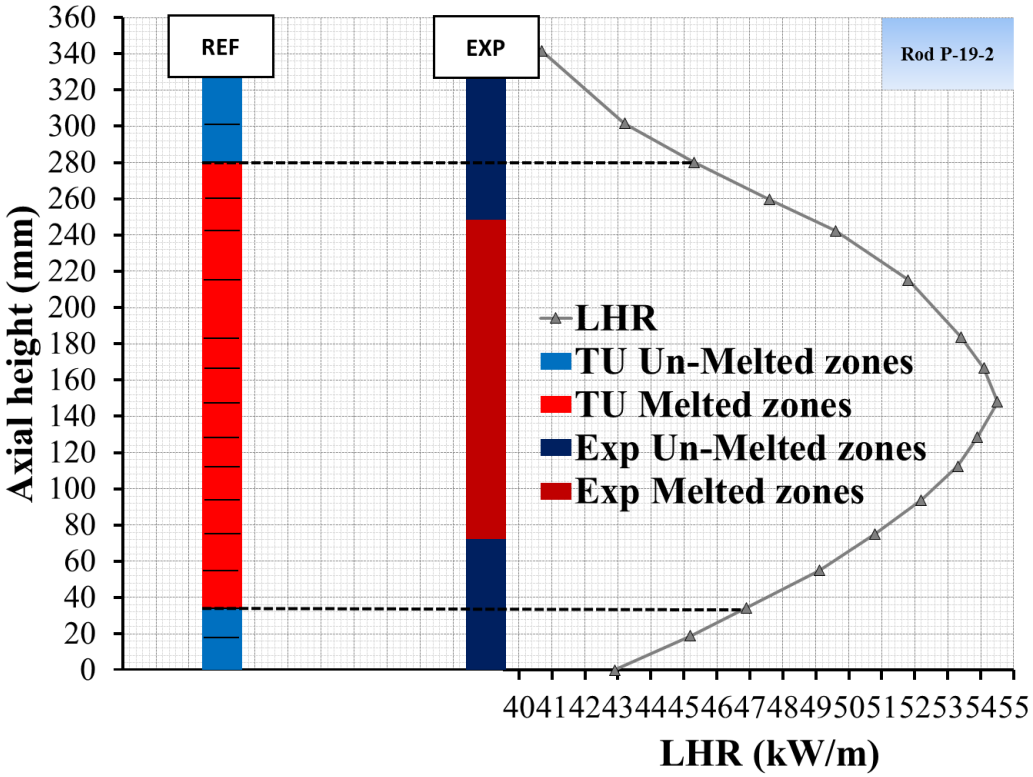

Figure 6-18 Simulation of HEDL P-19, rod P19-2, reference analysis, prediction of melting height.

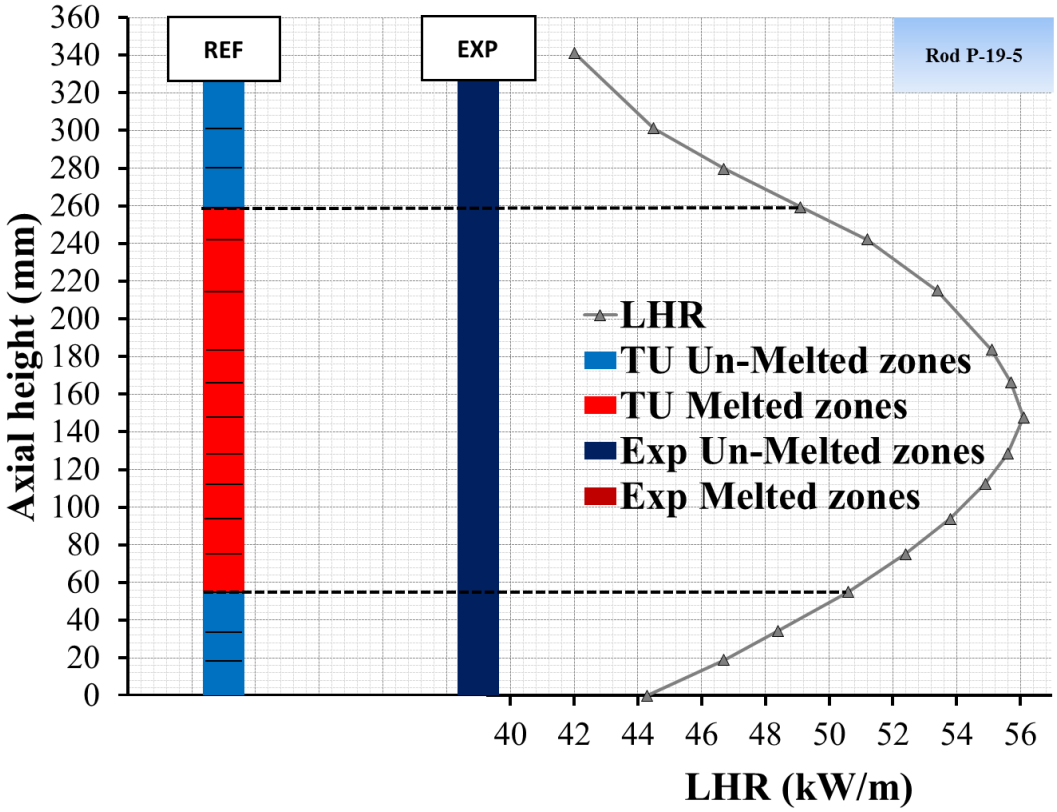

Figure 6-19 Simulation of HEDL P-19, rod P19-5, reference analysis, prediction of melting height.

6.4 Sensitivity analysis

The list of the sensitivity analyses that were performed for HEDL P-19 rods during this study could be found in *Table 6-6* and the motivation behind them. The analysis was performed on either parametric design values given by the experimental data, correlations or models provided by the code. Design parameters are labeled by **(D)**, while correlations are labeled by **(C)** and models labeled **(M)**. In the next subsections, separate sensitivity analyses of the factors stated in *Table 6-6* are going to be illustrated.

Case	Run	Modification	Objective
Fuel conductivity	**C1.1**	Modfuel(j=6)=31	Investigate the impact of fuel conductivity on melt front, gap width, central void and columnar. *Correlation of Van Uffelen & Schubert.*
	C1.2	Modfuel(j=6)=32	Investigate the impact of fuel conductivity on melt front, gap width, central void and columnar. *Correlation of Carbajo..*
	C1.3	Modfuel(j=6)=33	Investigate the impact of fuel conductivity on melt front, gap width, central void and columnar. *Correlation of Lanning & Beyer.*
	C1.4	Modfuel(j=6)=24	Investigate the impact of fuel conductivity on melt front, gap width, central void and columnar. *According to Wiesenack multiplied by a MOX correction factor.*
Pellet fragment relocation	**M1.1**	Ireloc 2	Investigate the impact of fuel relocation on gap width and melt front. *Original KWU-LWR model based on initial gap size only.*
	M1.2	Ireloc 3	Investigate the impact of fuel relocation on gap width and melt front. *GAPCON-THERMAL-3 based on initial gap size, LHR and burn-up.*

	M1.3	Ireloc 4	Investigate the impact of fuel relocation on gap width and melt front. *Operational relocation model according to Eberle and Stackmann, own calibration 1997, explicit formulation*.
	M1.4	Ireloc 6	Investigate the impact of fuel relocation on gap width and melt front. Operational relocation model according to Eberle and Stackmann, own calibration 1997, implicit formulation.
	M1.5	Ireloc 8	Investigate the impact of fuel relocation on gap width and melt front. *Modified FRACPON-3 model based on the as fabricated gap, the burn-up and the linear heat rate.*
Fuel restructuring models	**M2.1**	Istzne 2	Investigate the impact of fuel restructuring on melt front, gap size, and columnar growth. *Original model of Olander.*
	M2.2	Istzne 5	Investigate the impact of fuel restructuring on melt front, gap size, and columnar growth. *Fuel restructuring zones are calculated from boundary temperatures.*
	M2.3	Istzne 6	Investigate the impact of fuel swelling on fuel temperature, pin pressure and FGR. *Fuel restructuring zones are calculated from boundary grain sizes.*
solidus–liquidus melt temperature	**C2.1**	Modfuel(j=16)=10	Investigate the impact of solidus-liquidus melt temperature on the development of the melt front and the central void. *Correlation of Többe.*
	C2.2	Modfuel(j=16)=13	Investigate the impact of solidus-liquidus melt temperature on the development of the melt front and the central void. *Correlation by Pesl et al.*
	C2.3	Modfuel(j=16)=15	Investigate the impact of solidus-liquidus melt temperature on the development of the melt front and the central void. *Correlation is recommended in the Gmelin handbook.*
Gap size	**D1.1**	Gap size (+15μm)	Investigate the impact of uncertainty in the initial gap width on the evolution of the gap width and on the melt front formation. Initial value obtained assuming maximum cladding and minimum fuel radii according to design uncertainties.
	D1.2	Gap size (-15μm)	Investigate the impact of uncertainty in the initial gap width on the evolution of the gap width and on the melt front formation. Initial value obtained assuming minimum cladding and maximum fuel radii according to design uncertainties

Table 6-6 Simulation of HEDL-P19, list of correlations, models and design parameters considered in the sensitivity studies.

6.4.1 Thermal conductivity correlations

The conductivity correlations are assessed to highlight their influence on the prediction of the experimental data. The experimental melting height along with the prediction of the available TU correlation are depicted in *Figure 6-20*. TU correlations over-predicted the melting height of the rod except for COND-34 where the melting is under-predicted. This is consistent with the results obtained for the LWR MOX in section 5.4.2 and gives an indication of a trend of this correlation to under-predict the temperature of MOX fuel. COND-33 (Lanning and Bayer) fit the melting height of Rod P-19-2 in the best way relative to the other correlations. For rod P-19-5, the TU correlations predicted considerable melting of the rod except COND-34 that did not predict melting at all. A general conclusion is the tendency of TU thermal conductivity correlations to under-predict the thermal conductivity. The correlations were verified against LWR rods and in their operational regime. Their ability to predict the FBR rods behavior especially at high temperature close to melting is not completely checked. No major differences are observed when analyzing their influence on the prediction of the gap size, *Figure 6-21*. The correlation of Carbajo (COND32) highlights an improvement in the prediction of the central void (*Figure 6-22*) and on the columnar grain radius (*Figure 6-23*). However, it can be seen that the columnar grain radii are proportional to the prediction

of the temperature. Higher predicted temperatures results in higher columnar growth radii. Thus, this correlation further overestimates the melting height and the molten fuel radius (*Figure 6-24*).

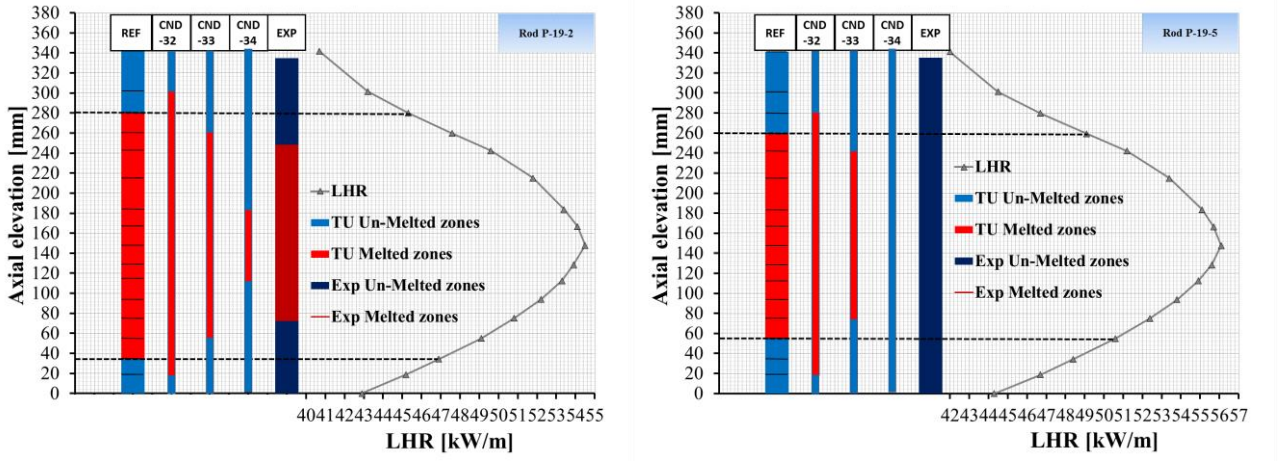

Rod P 19-2 *Rod P 19-5*

Figure 6-20 Simulation of HEDL-P19, sensitivity analysis on thermal conductivity correlations, prediction of melting height.

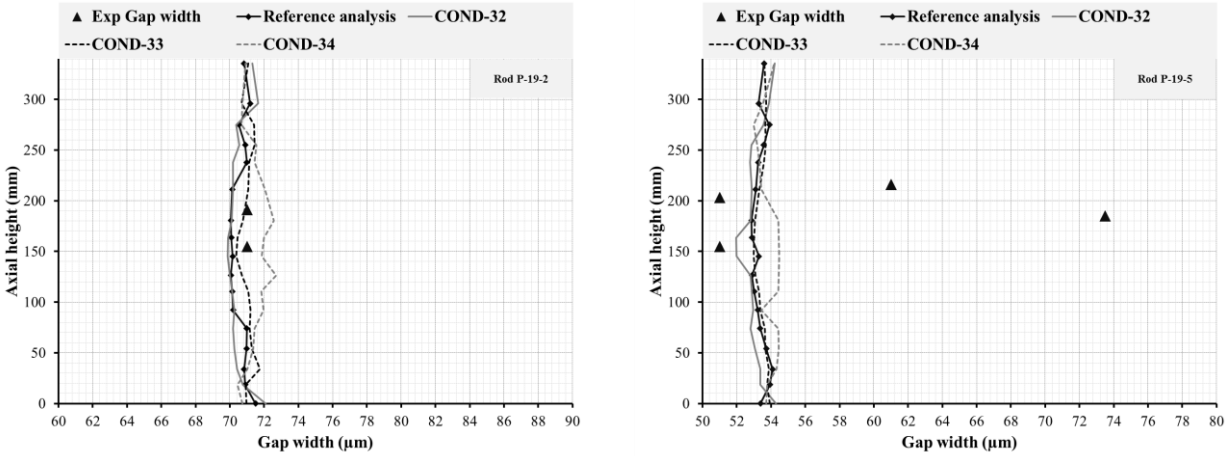

Rod P 19-2 *Rod P 19-5*

Figure 6-21 Simulation of HEDL-P19, sensitivity analysis on thermal conductivity correlations, prediction of gap width at the end of the experiment.

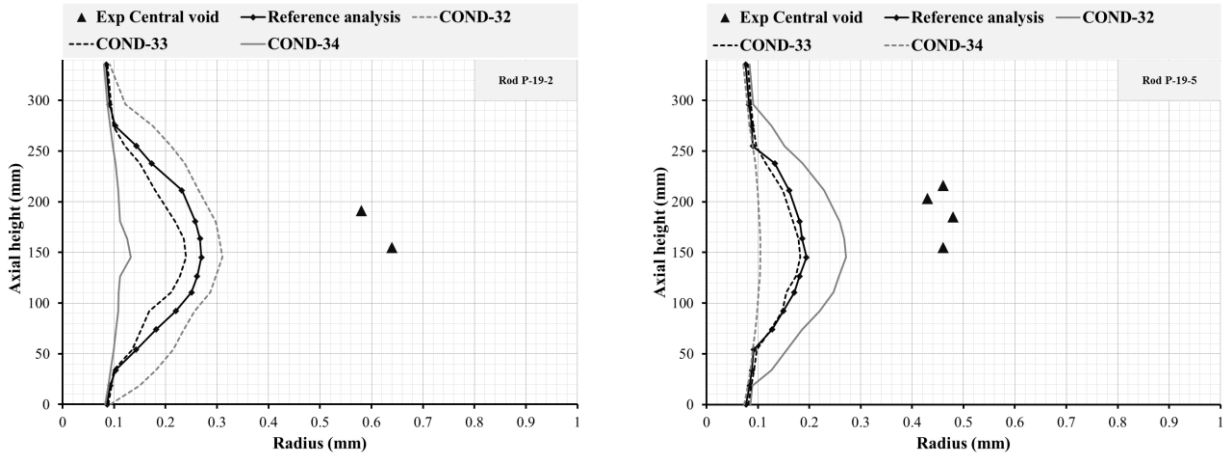

Rod P 19-2 *Rod P 19-5*

Figure 6-22 Simulation of HEDL-P19, sensitivity analysis on thermal conductivity correlations, prediction of central void at the end of the experiment.

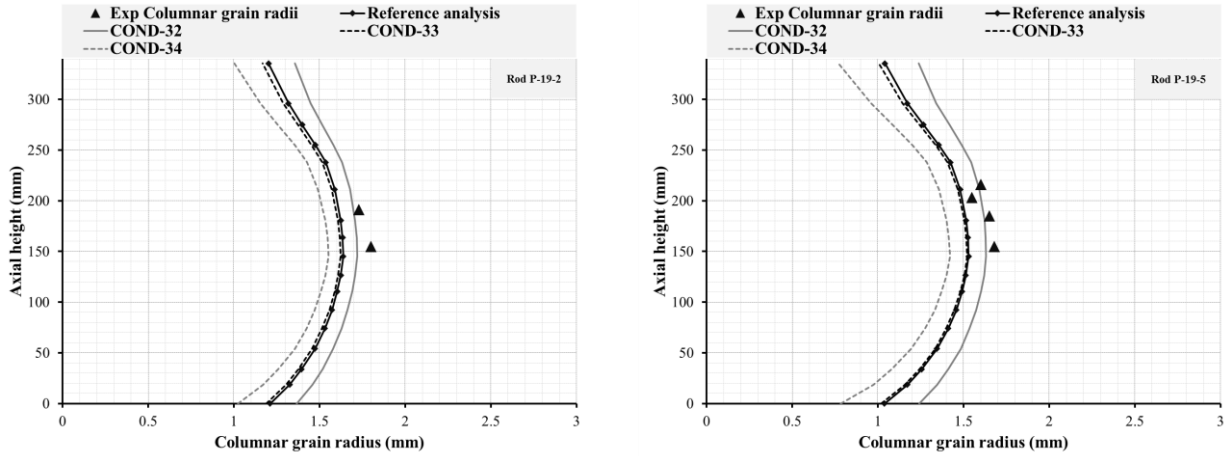

Rod P 19-2 *Rod P 19-5*

Figure 6-23 Simulation of HEDL-P19, sensitivity analysis on thermal conductivity correlations, prediction of columnar grain radius at the end of the experiment.

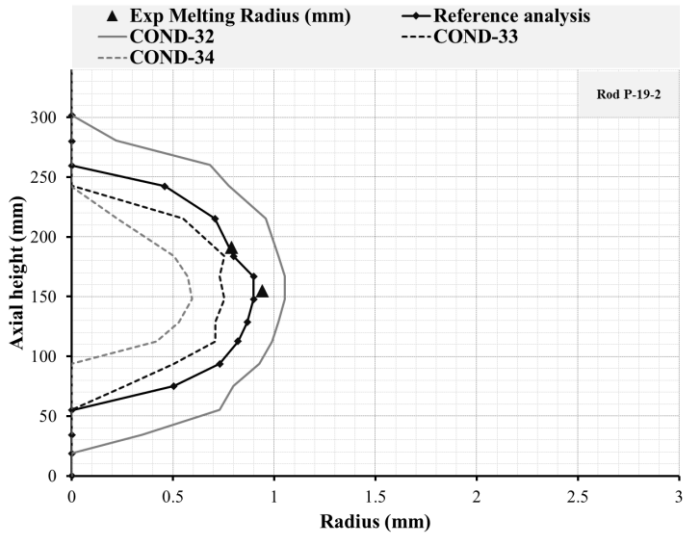

Figure 6-24 Simulation of HEDL-P19, sensitivity analysis on thermal conductivity correlations, prediction of melting radii.

6.4.2 Relocation models analysis

The gap widths predicted by relevant pellet fragment relocation models are plotted in *Figure 6-25*. It is noticed that the variability in gap widths is higher for P-19-2 than P-19-5 that did not experience melting. The reference model IRELOC=8 is the one that is more close to the experimental data. This did not result in different melting heights, see *Figure 6-26*. This can be related to the higher mesh in the discretization of the fuel rod. Still, the melting ratio of the fuel is variable between the models even if the melting heights are the same.

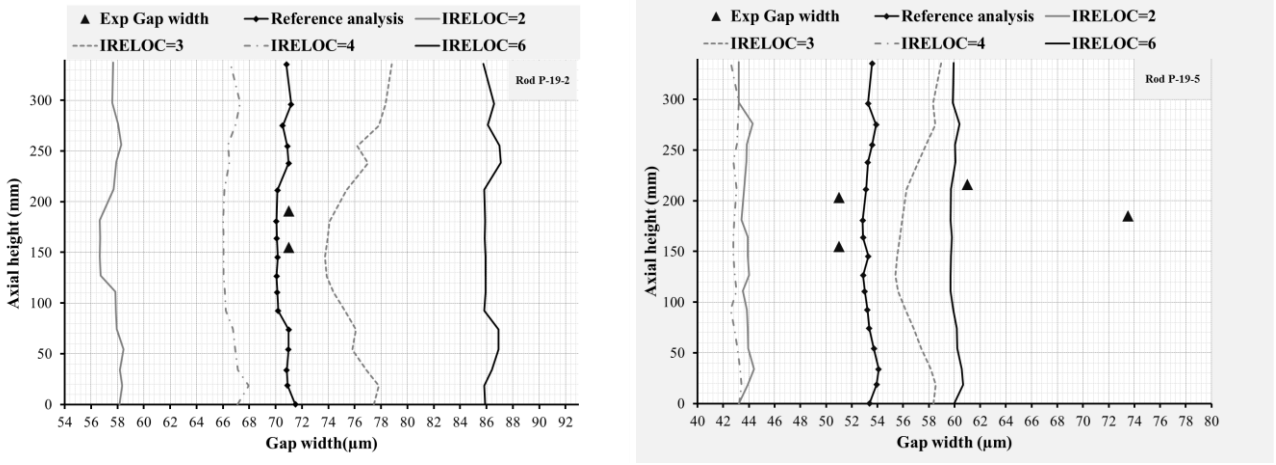

Rod P 19-2 *Rod P 19-5*

Figure 6-25 Simulation of HEDL-P19, sensitivity analysis on relocation models, prediction of gap width at the end of the experiment.

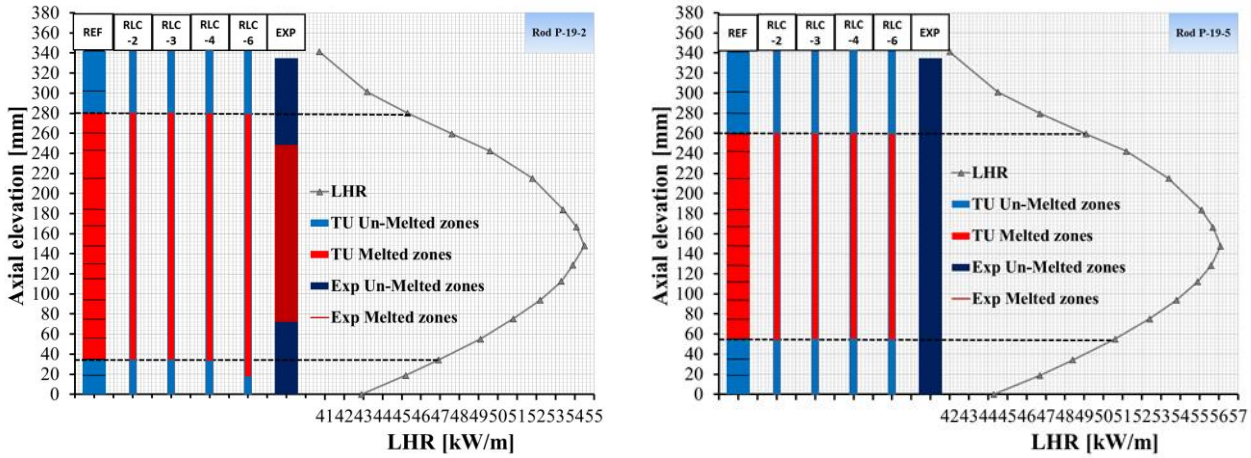

Rod P 19-2 *Rod P 19-5*

Figure 6-26 Simulation of HEDL-P19, sensitivity analysis on relocation models, prediction of melting height.

6.4.3 Solidus-liquidus melting models

The models available in the code to simulate MOX fuel melting consider the melting temperature as a function of burn-up, O/M ratio and Pu content. The reference model was a constant value (similar to those experimentally measured in HEDL-P19). The models resulted in noticeable variations of the central void prediction and the melting height: *Figure 6-27*, *Figure 6-28*. The rest of the experimental parameters were not significantly affected. The reference model predicted the highest void formation for both rods.

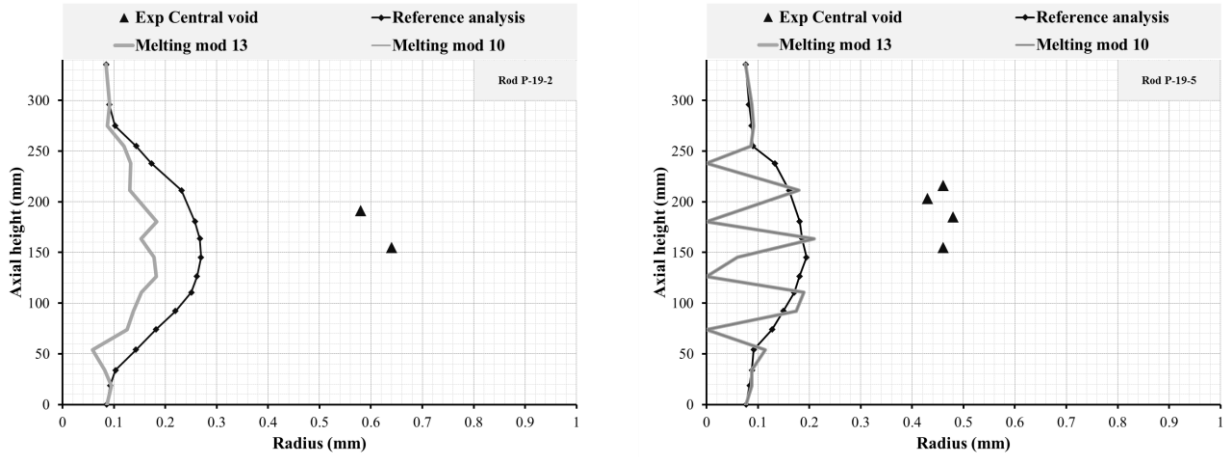

Rod P 19-2 *Rod P 19-5*

Figure 6-27 Simulation of HEDL-P19, sensitivity analysis on melting models, prediction of central void at the end of the experiment.

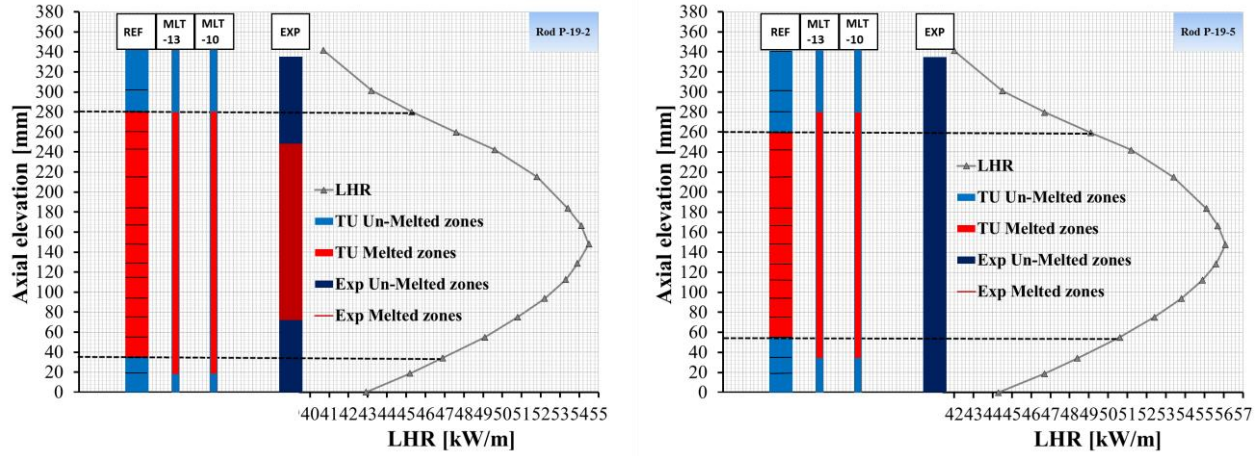

Rod P 19-2 *Rod P 19-5*

Figure 6-28 Simulation of HEDL-P19, sensitivity analysis on melting models, prediction of melting height.

6.4.4 Fuel restructuring models

The fuel restructuring models did not affect any of the measured parameters in the rod except the outer radius of columnar grain zone, see *Figure 6-29*. The melting heights predicted by the models were the same. The prediction of the formation of the columnar zone by Istzne-2 was the smallest while the reference case captures the columnar growth in the rod in a good way.

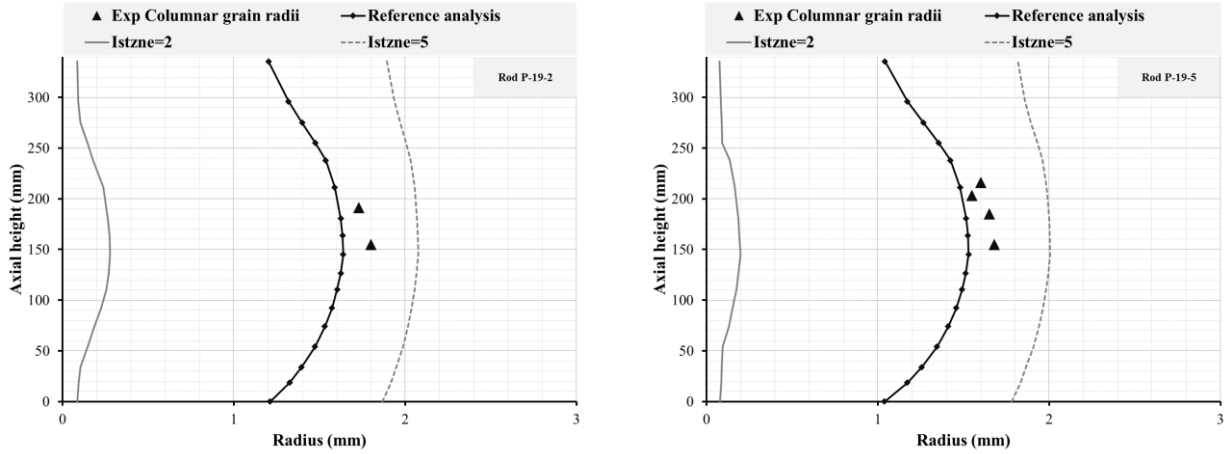

Rod P 19-2 *Rod P 19-5*

Figure 6-29 Simulation of HEDL-P19, sensitivity analysis on restructuring models, columnar grain radii prediction.

6.4.5 Initial gap width

Initial gap width is a parameter provided by the experiment. In this study, the nominal initial gap width was assumed to have around 15% uncertainty. 80% percent of this uncertainty was due to uncertainty in the outer fuel radius and 20% was related to the inner cladding radius.

Uncertainty in the initial gap width affects all the measured parameters of the rod. It is a critical factor to be precisely measured. Increasing the initial gap size results in a degradation of thermal conductivity and as a result higher temperatures inside the rod are expected. This affects everything else and results in wider central void and melting radius and more columnar grain growth inside the rod. The final result is a longer melting height inside the rod, *Figure 6-30*. The opposite is true when the initial gap size is reduced, better heat transfer will occur inside the rod and the temperature and melting heights will decrease. However, the nominal initial gap width resulted in the best predicted value of the gap width at the end of the experiment, *Figure 6-31*. Therefore the analysis was continued with belief that the initial gap width measurement was not a source of significant error in the results and any bias of the results in the over prediction of the temperature is not related to an error in the initial gap determination by the experimenter.

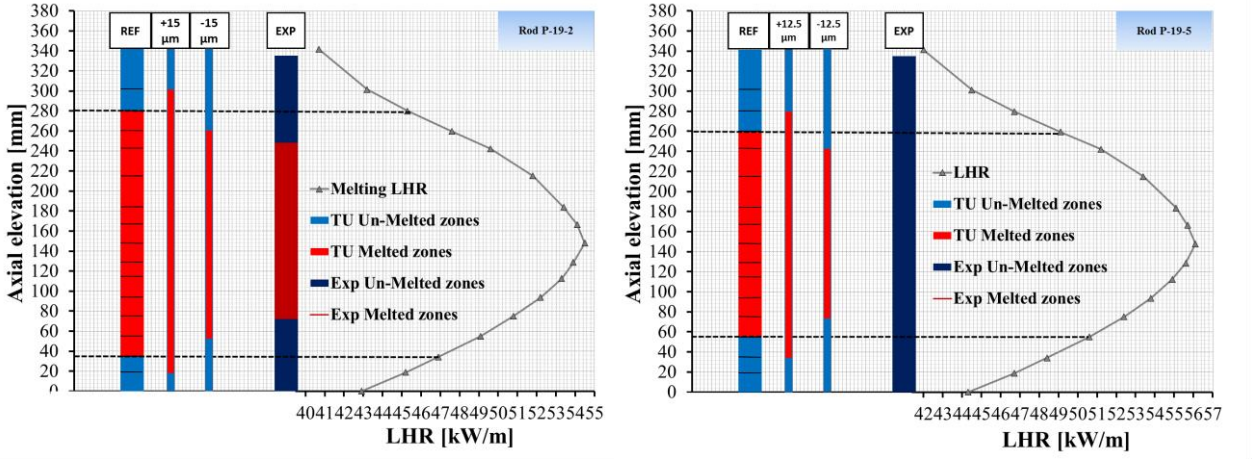

Rod P 19-2 *Rod P 19-5*

Figure 6-30 Simulation of HEDL-P19, sensitivity analysis on initial gap size, prediction of melting height.

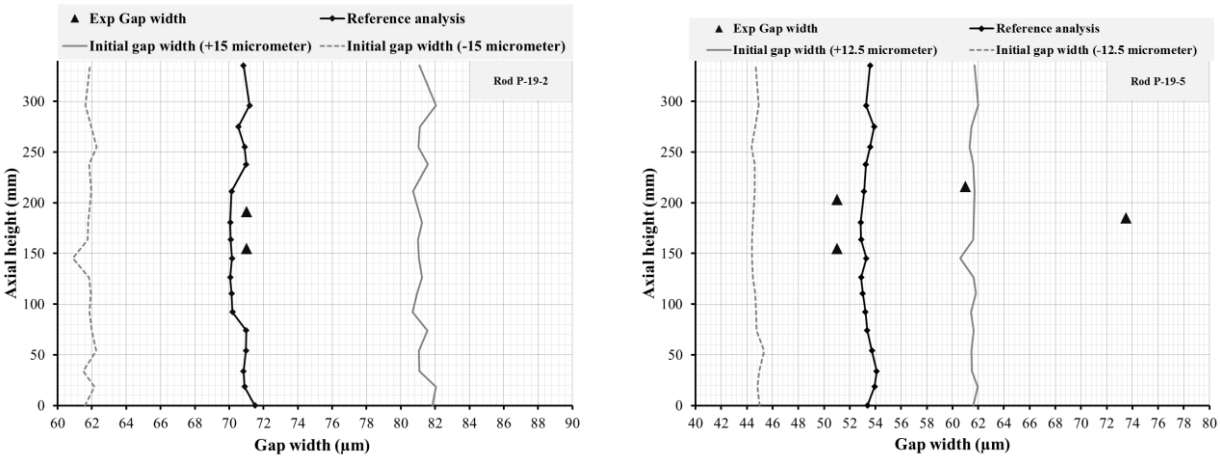

Rod P 19-2 *Rod P 19-5*

Figure 6-31 Simulation of HEDL-P19, sensitivity analysis on, prediction of gap width at the end of the experiment.

6.5 Radial analysis

Two separate approaches were used for each P-19 rod because of the difference in the post-irradiation conditions. Radial analysis for rod P-19-2 was done at the end of melting at the moment when the melt fraction and the melting height reached their maximum values. For rod P-19-5, the analysis was done prior to power ramp to induce melting. The reason behind this is that the rod did not experience any melting as confirmed by the radio-graphical investigation. The temperature during the power ramp should be lower than the melting temperature (2762 ^{0}C). It is not known how low the real temperature was below the melting value. TU predicted melting inside the rod. Considerable melting heights were predicted by the code which indicates a temperature much higher than the melting temperature. Therefore, the comparison was done before the power ramp where melting did not occur neither experimentally nor by TU prediction. Open literature correlations were plotted as well in the same manner and for the same purposes in section 5.5.

Rod P-19-2 experienced melting height between the upper and lower boundaries mentioned in *Table 6-2*. The thermal conductivity correlations of TU resulted in an over-prediction of the melting height which can lead to a conclusion of under predicted thermal conductivities. Predicting lower thermal conductivity would result in code prediction of higher melting heights than the actual height except for COND-34 that under-predicted the melting height. During melting the thermal conductivity is assumed to be 1.5 W/mK for COND-31, COND-33, and COND-34. COND-32 assumed a thermal conductivity beyond melting of 2.5 W/mK.

In *Figure 6-32* various TU and OL correlations are plotted together for comparison among themselves and with fitted experimental data. As expected from the previous analysis (section 6.4.1), COND-34 predicted the highest thermal conductivity on the whole range of temperatures in the rod. That range of thermal conductivity resulted in the smallest melting height. This is an indication that the thermal conductivity, especially in the high temperature range should be lower than COND-34 but still should be higher than the rest of the other correlations. COND-32 predicted the lowest thermal conductivity on the whole range of temperatures except in the part where melting is predicted. The thermal conductivity is higher since it is modelled as a constant of choice of the developer of 2.5 W/m.K while for the rest of the correlations a melting thermal conductivity was chosen to be of 1.5 W/mK. COND-33 predicted lower melting height than COND-31 and closer to the experimental measurements. In fact, the thermal conductivity predicted by COND-33 in most of the ranges of temperatures prior to melting is higher than COND-31. Only near the periphery of the rod where T <1400^{0}C, the thermal

conductivity of COND-31 is slightly higher but at that location it would not cause much difference in the temperature profile.
The open literature correlations are compared only prior to melting since thermal conductivity during melting is modelled as constant. Matpro correlation predicted higher thermal conductivity than the rest of the correlations up to 2270^0C where they become lower than COND-34 up to melting. Thermal conductivity according to Martin predicted thermal conductivities comparable to the standard correlations COND-31 up to 2000^0C where they become lower than COND-32. The correlation is expected to result in a higher prediction of temperatures and melting heights similar to COND-32. Comethè correlation predicted a thermal conductivity higher than COND-33 up to 2080^0C where it becomes lower than it. It predicts also a thermal conductivity higher than COND-31 up to 2550^0C where it becomes slightly lower than it. Comethè correlation might give similar prediction to COND-31. Baron-Hervè correlation predicted higher thermal conductivity than COND-31 on the whole range prior to melting. It predicts higher thermal conductivity than COND-31 except in the mid section of the rod where (1600^0C<T<2300^0C). In general, Baron-Hervè-95 has a potential of predicting better melting heights and is investigated later.
Special preparations were taken to compare the experimental data with the studied correlations. The experimental data available were taken from the work of Duriez et.al[10]. The sample used in this study was a fresh MOX with homogeneous Pu 21.4wt% and O/M ratio 1.982, and theoretical density 95.6% up to 1850^0C. In order to be able to use this sample for comparison with the studied correlations, the similarities between the sample and the P-19 pins were closely examined. The plutonium content in the studied P-19 pins, was around 22 wt% and can be considered to be homogeneous. It is a value close to the one of the sample and no modification was done to it. Examining the theoretical densities, the studied pins had a smeared density in the mid-section and peripheries of around 91.4%TD. In order to be able to compare the MOX sample to the P-19 pins, the experimental data were rescaled to the porosity level of the pins using Lucuta's formula. That is the formula used as a porosity correction for COND-33[11]. Since there is no formula to rescale the O/M ratio, the sample was added for comparison at the original level (1.982) and it was used only for qualitative comparison with the models.
It can be seen that the data are closer and have the same trend as that of COND-33 in the low temperature range up to 1400^0C. Above that value, it can be seen that the experimental data of thermal conductivity shows ascending pattern with temperature with a higher rate than that of COND-33 and is going along side with COND-34 up to 1800^0C. What can be induced from this point up in temperature is that there is a visible trend of the experimental data to increase above all TU correlations except COND-34. At higher temperature, the effect of deviation from stoichiometry decreases. At 2000 K (1727^0C) the change of thermal conductivity due to a change of O/M from 2 to 1.95 does not exceed 8%. Therefore, a change of the experimental 1.98 value to 1.96 of the pins is not expected to decrease the scale of the experimental data with more than 3%. Practically this value would be even lower since the temperature exceeds the melting temperature (2762^0C) which means much lower effect of deviation from stoichiometry on the thermal conductivity.
What can be concluded from this comparison is that the thermal conductivity of TU correlations is under-predicted relative to the experimental data. To what extent this under prediction is cannot be determined exactly without obtaining more experimental data on high temperature, high Plutonium content MOX fuel since the work of Ronchi (which is the basis for the high temperature terms of COND-31 and COND-33) was intended for LWR grade of MOX fuel.
The same analysis applies for rod P-19-5 and can be seen in *Figure 6-33*. As expected there is no much change from the previous comparison for P-19-2 since the plutonium content, porosity, O/M ratio are the same for both rods. The figure is similar to that of rod P-19-2 except that it is on a lower scale since the analysis was done prior to the ramp conditions and no prediction of melting was done by the code. The range of comparison is thus up to 2760 ℃ (COND-32) and not exceeding it for the rest of the correlations.

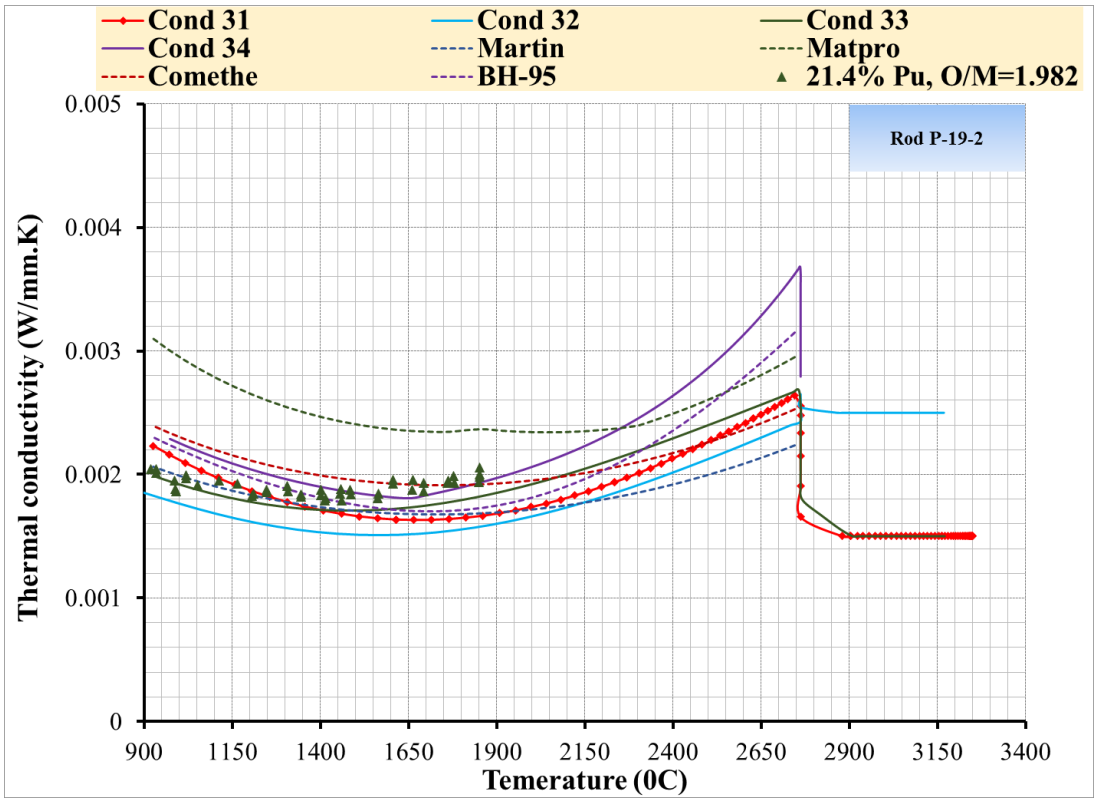

Figure 6-32 Radial profile of thermal conductivity for rod P-19-2.

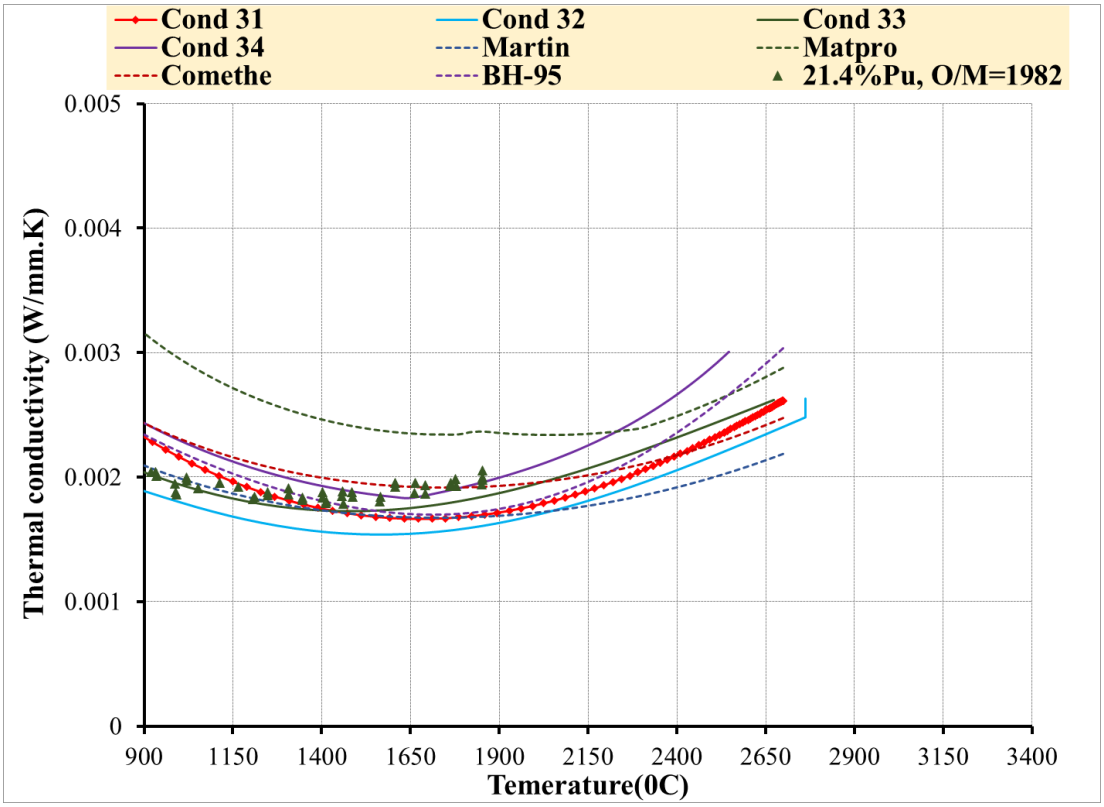

Figure 6-33 Radial profile of thermal conductivity for rod P-19-5.

7 Review of thermal conductivity correlations

COND-31 (Van Uffelen & Schubert), COND-33 (Lanning & Beyer), and Baron-Hervè 1995 correlations will be investigated for the potential differences between them. The main goal is to find out which correlation can result in a better prediction of the FR MOX fuel melting height discussed in the previous chapter. The main causes of differences between the correlations are the O/M ratio, the high temperature conduction term and the Plutonium content. The Plutonium content is not expected to be a significant reason for the incapability of the code to predict the fuel melting. The reason is that the thermal conductivity decreases as the Pu content increases. The thermal conductivity correlations of TU are verified against LWR MOX rods which contains low plutonium content. If the plutonium content is included in TU correlations, the result for high plutonium content rods is a decrease in thermal conductivity relative to what the original correlations predict. A consequence of this expected decrease in thermal conductivity is an increase of the over-prediction of the melting of the investigated fuel rods.

Figure 7-1 represents an analysis of the lattice and electronic terms of the investigated correlations. Several remarks can be made from the figure. It can be seen that the lattice conduction term is lower for the BH-95 correlation than the TU correlations. At higher temperatures, it is noticed that the lack of the O/M ratio term in the COND-31 correlation did not result in any visible deviation from COND-33 correlation. This is expected since at higher temperature the effect of O/M ratio on thermal conductivity decreases. At lower temperatures, the effect of O/M is visible. During high linear power operation of FBR, these temperatures will exist near the periphery of any investigated FR rod where the temperature gradient is more important in heat transfer than the thermal conductivity.

It can be seen also that for most of the temperature range, COND-31 has a higher lattice thermal conductivity except near the melting temperature. Yet the correlation predicts a higher melting height than the height predicted by COND-33. This gives an indication that the overall higher thermal conductivity predicted by COND-33 is related to the higher electronic conduction term of this correlation.

It is therefore expected that the lower prediction of the melting height by COND-33 is related to the electronic conduction term, rather than the O/M factor that is missing from COND-31. The higher electronic conduction term in BH-95 correlation is the reason of the higher thermal conductivity predicted by it at very high temperatures near the melting temperature of the investigated FBR rods in the previous chapter (*Figure 6-32*). In order to properly investigate the melting LHR of FBRs, the conduction due to higher temperature factors should be investigated for fast reactors grade of MOX fuel.

The TRANSURANUS code is going to be used as a verification tool of the effect of the high temperature term in the BH-95 on the prediction of the melting of the investigated FR MOX rods. The functions lamf31.f95 and lamf33.f95 are the TU Fortran functions that contain the functions that are used for calculating the thermal conductivity based on COND-31 and COND-33, respectively. They were both edited so that the higher temperature term in the original correlations was changed to that from the BH-95 correlation. The code was then re-compiled to create a new version in which the new changes were integrated. The FBR rods were then analyzed using TU to verify the ability of the new version of the correlations to predict the integral behavior of the rods and the ability of the code to predict the melting heights, the centerline temperature and the gap width of the two rods.

Rod P-19-2 was analyzed using the modified correlations COND-31 and COND-33. It can be seen in *Figure 7-2* that the code predicted a shorter melting height of the rod than the original correlations. The lower limit of the predicted melting is comparable to the experimental measurement. The higher limit of melting predicted by the correlations is 242 mm height that is slightly shorter than the experimental measurement (249 mm). This cannot lead to a conclusion of under-prediction of the thermal conductivity by the code due to the nature of the discretization of the rod. The next node on the rod where the melting is zero is at 259 mm. As shown in *Figure 7-2***,** the melting fraction prediction by the code at the lowest melting position is between (0.5% and 0.9% of the rod by COND-33 and COND-31 respectively). Therefore as shown in the figure, the actual point at which the rod did not suffer melting is somewhere between 242 and 259 mm which is not determined precisely by the code. The figure also shows how the melting fraction predicted by the code is much lower than that of the original correlations. The similarity between the melting heights of both the modified correlations relative to the difference of melting heights of the original ones strengthen the idea that the electronic conduction term is the key factor in the prediction of the thermal conductivity in HEDL P-19 experiment. When the same high temperature term in both correlations is used, the melting heights predicted became the same.

The gap width predicted by the new correlation is compared with the experimental data in order to be able to relate the newly predicted heights to the change of thermal conductivity rather than any inaccuracy in the prediction of gap size. In *Figure 7-3* the gap width predicted by the original and modified correlations at the end of the experiment is plotted. There is a tendency of the modified version of the code to predict a higher gap size. This is expected due to the lower thermal expansion coming from the lower temperature predicted. However, the difference between the gap widths predicted by all the correlations is within (±1 μm). The gap width predicted by the modified COND-31 is the most accurate and comparable with the experimental measurements.

Finally, the centerline temperature temporal evolution during the whole experiment is considered in *Figure 7-4***.** It can be seen that the reference correlation (COND-31) and the modified version gives the same prediction of the centerline temperature up to 1800^0C. This is expected since at these temperatures the lattice vibration term is more important and is the same for both correlations. Above this temperature, the temperature prediction deviates from each other and the modified correlation predicts lower centerline temperature than the original correlation due to the higher electronic conduction term. The temperature predicted by the modified correlations are comparable to each other with lower difference between them than between the original TU correlations.

The maximum centerline temperature during melting for the modified correlations are 3023^0C and 2965 ^{0}C for COND-31 and COND-33, respectively, which is around 250^0C lower than the original COND-31. This high difference is an evidence of the lack of ability of TU to predict the temperature of FR MOX. The original code is too conservative for the HEDL P-experiment. The modified version is less conservative and more able to accurately predict the melting heights inside the rods, which is reflective of its better capability to predict the real unknown temperature during the melting phase of the experiment. The modified COND-31 is more conservative than the modified COND-33 and predicts a maximum temperature that is 58^0C higher. This is the best qualitative conclusion that can be inferred based on the nature of the HEDL P-19 experiment, which is a melting experiment in which the actual temperatures of the rods were not measured.

The analysis of rod P-19-5 using the modified correlations showed a lower melting height than that of the original code (*Figure 7-5*). The rod did not experience melting during the experiment but the code predicted melting. Still, the prediction of the modified code is lower (better) than the original one for both aspects of the melting: the melting height and fraction. The melting fraction did not

exceed 3.8% at peak position in the rod compared to (10-12%) for the original code (*Figure 7-5*). The code is still conservative but on a lower level. The gap predicted by the code using both modified correlations is wider than the original one (*Figure 7-6*). This leads to a difference between the experimental measurement and the code prediction of about (3 µm). This higher gap width predicted by the code increases the temperature prediction making the code more conservative. The centerline temperature (*Figure 7-7*) during the melting phase predicted by the code did not increase above the melting temperature of the fuel (2762^0C). The temperature predicted by the original reference correlation COND-31 is 3122^0C. Therefore, the original code predicts a temperature that is 360^0C higher than the modified code which is still conservative.

The radial profile of the thermal conductivity is analyzed during the melting phase in the same way as in section 6.5. This time all the results are based on values calculated by TU for the exact conditions predicted by the code for the original and modified code. Only the original and modified COND-31 and COND-33 are considered. COND-34 is plotted as a sort of limiting comparison since it is the correlation that resulted in the highest thermal conductivity predicted by the original code and the only correlation that under predicted the melting heights of rod P-19-2.

It can be seen in *Figure 7-8* that for temperatures above 2000^0C the modified correlations predicts higher thermal conductivities than the original ones. Modified COND-33 predicts the highest thermal conductivities and at some range of the temperature becomes tangential with COND-34. At lower temperatures, the modified COND-31 gives the same results as the original one since at low temperatures, the electronic conduction term is negligible. Above 1400^0C the modified correlation increases more than the original one and keeps increasing to the end of the studied range below melting but does not reach the same level as COND-34. The modified COND-33 predicts the same value for the original one at low temperatures and then decreases below it. This is due to the slightly lower electronic conduction from the BH-95 correlation than that from the original COND-33 as shown in *Figure 7-1*. Above 1900^0C, the modified COND-33 is higher than all the other correlations and keeps increasing above the original correlation but stays below COND-34.

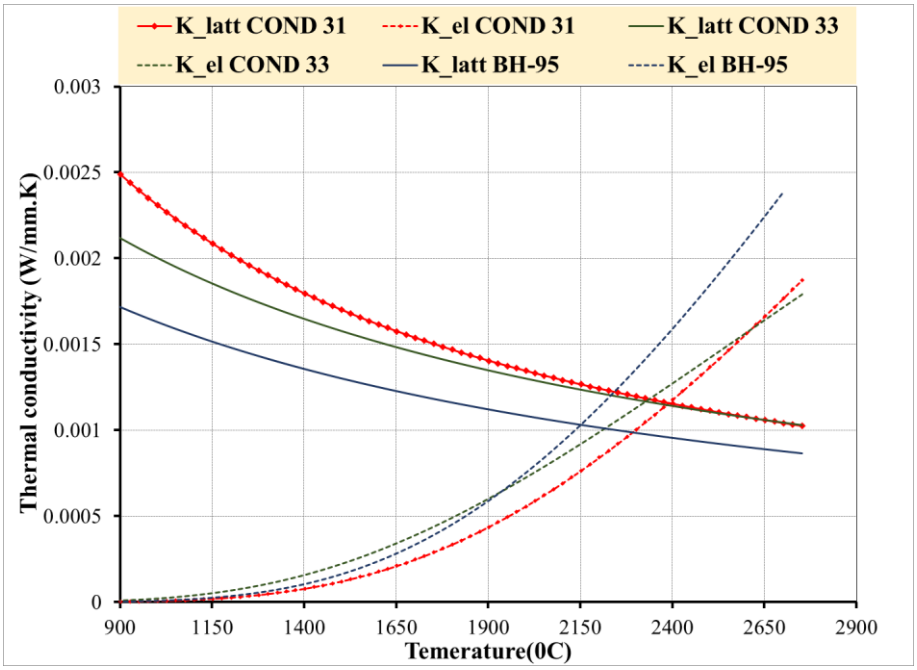

Figure 7-1 lattice and electronic conductivities comparison.

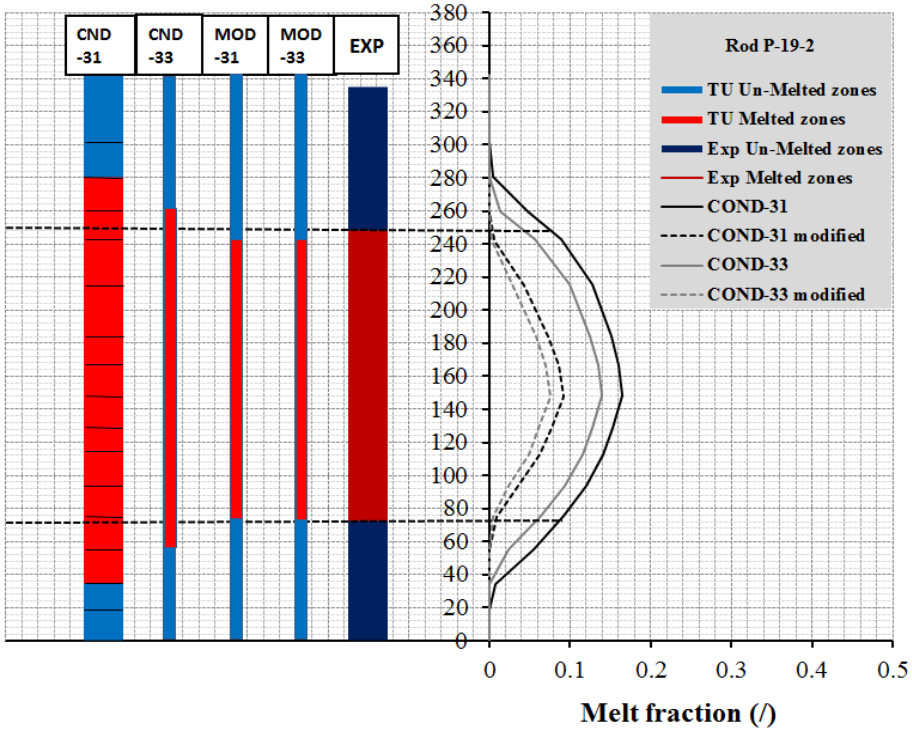

Figure 7-2 Rod P-19-2, Comparison between the melting heights and fraction according to the original and modified correlations.

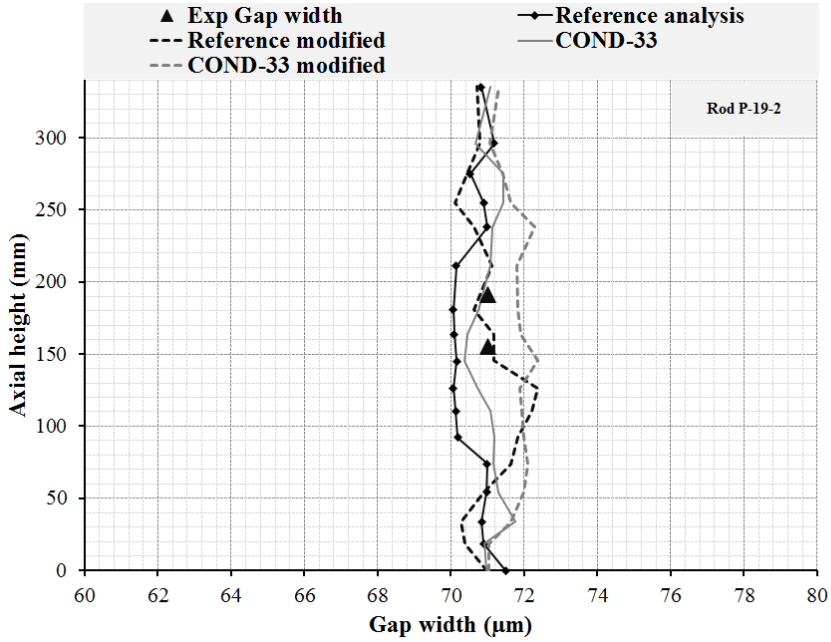

Figure 7-3 Rod P-19-2, Comparison between the predicted gap width at the end of the experiment by the original and modified correlations.

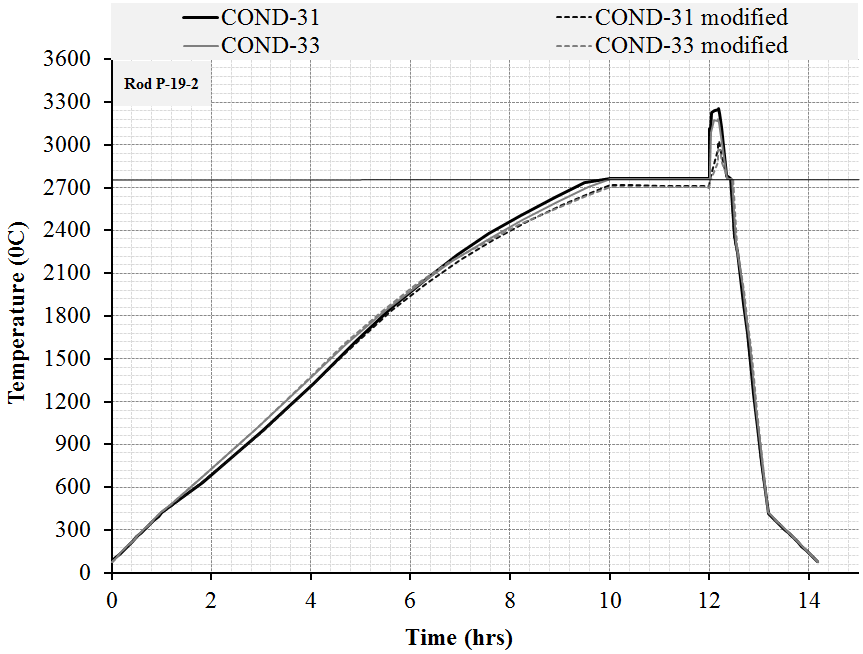

Figure 7-4 Rod P-19-2, Prediction of centreline temperature by the original and modified correlations.

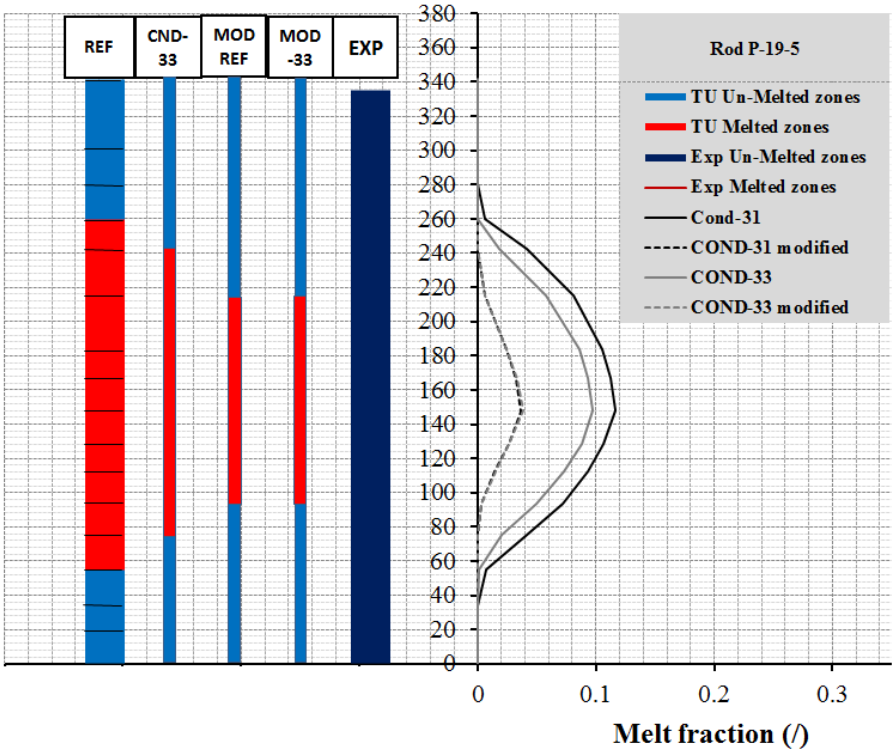

Figure 7-5 Rod P-19-5, Comparison between the melting heights and fraction according to the original and modified correlations.

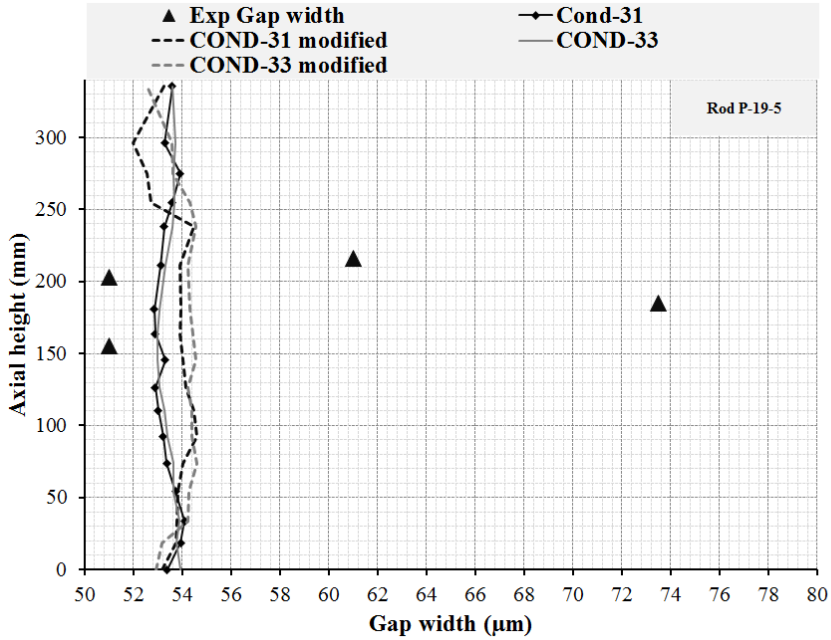

Figure 7-6 Rod P-19-2, Comparison between the predicted gap width at the end of the experiment by the original and modified correlations.

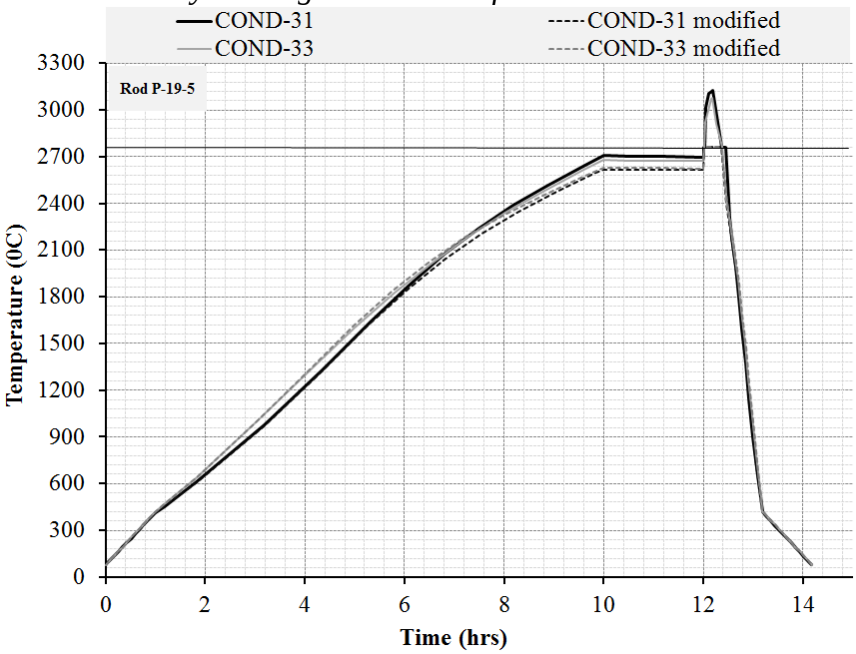

Figure 7-7 Rod P-19-5, Prediction of centreline temperature by the original and modified correlations.

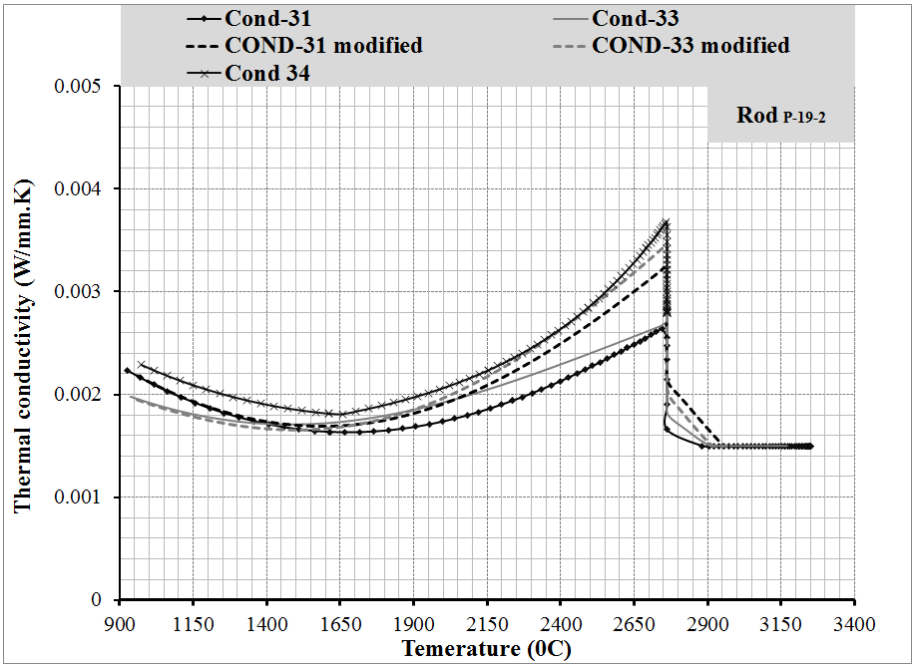

Figure 7-8 Radial comparison of thermal conductivity for rod P-19-2 predicted by the original and the modified correlations.

8 Conclusion

There are various factors that affect the thermal conductivity hence the prediction of the temperature profile in MOX fuel. At different temperature ranges different concepts of heat conduction apply. At lower temperature the lattice vibration term is the main mechanism of heat conduction and results in a general decrease of thermal conductivity with temperature while at higher temperatures, the main mechanism that has an increasing impact with temperature is either modelled as radiation heat transfer or electronic conduction. The way of modelling these parameters and the difference between the two phenomena result in a variation between correlations predicting thermal conductivity. The lattice vibration is affected by several phenomena such as burn-up, deviation from stoichiometry, Plutonium content and fuel porosity. Taking into account or disregarding any of these parameters, how they are considered, and the different data upon which a thermal conductivity correlation is based results in a variation between the predictions of thermal conductivity correlations that needed to be assessed.

Deviation from stoichiometry results in a decrease of thermal conductivity and is an important factor to be considered when modelling non-stoichiometric fuel. Burn-up cannot be neglected and its degrading effect on the thermal conductivity is confirmed. Porosity is taken into account by various corrections factors that represent an averaging effect of the pores shapes and sizes. Plutonium content has a minor effect on the thermal conductivity at low Pu content usually used in thermal reactors. However, there is a significant difference in FR fuel behaviour which uses a higher content of plutonium (>20 wt.%) than at low content. This indicates that thermal conductivity correlations based on LWR fuel type might fail to predict the thermal conductivity of FR fuel type. Therefore, codes that are tailored to predict the thermal performance of the MOX fuel must be validated for both kinds of reactors separately to confirm the range of the applicability of the code to the specified reactor and provide a window for further improvement of the correlations used in the code.

In this work, TRANSURANUS was investigated against thermal and fast reactors rods to assess the ability of the code to predict the integral behaviour MOX fuel rods of both types of reactors. This was done based on two experimental databases IFA597/.4./5 and HEDL P-19.
IFA597/.4./5 was performed in Halden heavy boiling water reactor and included two LWR MOX fuelled rods (solid and hollow). The base irradiation process took place at different levels depending on the purpose of the experiment; higher level to study FGR in IFA597.4, while in IFA597.5 the purpose was to accumulate fission gases in the lattice itself. Reference models and correlations used to predict various phenomena in the fuel (densification, swelling, pellet fragment relocation, etc.) were combined together in a reference input file to predict the overall behaviour of the fuel rods. The code was able to generally capture the experimental centreline temperature measured online on both rods. There were slight under-predictions of the centreline temperature but it still lies within the 5% uncertainly of the LHR. A general conclusion is that the code is able to capture the temporal profile of the centreline temperature during the experiment. This is an indication of the ability of thermal conductivity correlations to predict the temperature profile of thermal reactor MOX fuel. An exclusion to that is the correlation by Wiesenack that resulted in a significant under-prediction of the temperature. The correlation was originally designed for UO_2 fuel and projected to MOX fuel using a correction factor of 0.92. The missing burn-up factor in the open literature correlations limits their ability to predict thermal conductivity of the fuel to lower burn-up rates. Their prediction deviate from TU significantly at higher burn-up and would result in a significant under-prediction of the centreline temperature. TU under-predicted FGR for both rods. A consequence of that is the under-prediction of the pin pressure.

Behaviour of MOX fuel in FR was verified against HEDL-P-19 experiment. The experiment was conducted in the EBR-II to investigate power to melt of fresh MOX rods representative of the FFTFs driven fuel design. The temperature profile was not measured in this experiment since melting of the fuel was expected. Therefore, the fuel was radiographed as part of post irradiation investigation to determine the extent of melting and calculate the power limit at which the fuel is expected to produce melting.

Two rods out of a total of sixteen fresh rods irradiated in this experiment were studied in this work. Rod P-19-2 radiography showed that it suffered partial melting during the experiment while rod P-19-5 did not. The prediction of the melting heights by the code was determined by investigating the melting fractions predicted by the code and determining the melting heights based on it. The code results are an over-prediction of the melting heights for rod P-19-2 and prediction of melting of rod P-19-5 that remained solid during the experiment. The code was able to predict the gap width at the end of the experiment and underestimated the central void. However, the later parameter cannot be compared accurately with the simulations (at least for the rod that experiences melting) due to the occurrence of melting fuel relocation. The over-prediction of the melting heights can be related to the under-prediction of the thermal conductivity of the FR grade of MOX fuel in the high temperature regime (close to melting).

By comparing the radial profile of the thermal conductivity at the melting phase of the experiment, the thermal conductivity at high temperature is expected to be higher that what was predicted by TU. The high temperature thermal conductivity term is expected to be the main reason for this overall under-prediction of the thermal conductivity. The review of the open literature correlations along with TU correlations suggested the usage of the high temperature term from Baron-Hervè correlation along with the standard correlation of TU and the correlation by Lanning and Beyer. This term was inserted to TU and the code was recompiled to generate a new testing version of the code.

The insertion of this term resulted in a melting height comparable to what was investigated experimentally for rod P-19-2. The new version predicted some melting inside the rod P-19-5 but did not exceed 4% at peak power position. The maximum temperature predicted by the code was comparable to the melting temperature of MOX. The gap widths predicted by the code are still comparable to the experimental measurements. The equally predicted heights of melting by using the same high temperature term in the correlations mentioned above confirmed the idea that the lower electronic conduction term in the original correlations is the main factor that led to the under-prediction of the code. Using the same electronic conduction term led to the prediction of the same melting heights. There are still differences in the centreline temperature prediction. The standard correlation adopted by TU is more conservative and predicts a higher centreline temperature than that predicted by Lanning & Beyer but it is around 200^0C lower than the original version.

Unfortunately due to the nature of the experiment, the temperature cannot be compared accurately to determine how much accurate the new versions of the correlations predict the temperature. The effect of this modification on the prediction of normal operation conditions of FR is unknown but it is expected that the code will predict a lower temperature than before but not as low as in the case studied in this work. This modification will not affect the ability of the code to predict the centreline temperature of thermal reactors since the temperatures in this type do not exceed values where the high temperature thermal conductivity terms are important. The current modification would be useful in predicting early in life power-to-melting and simulate the conditions of melted fuel. However, the ability of the code to predict normal operation temperatures and the effect of burn-up on the code prediction should be verified against other types of experiments where the temperature is actually measured.

REFERENCES

[1] *P. Van Uffelen,* **Modeling of Nuclear Fuel Behavior**, Publications Office, JRC Publications, Report EUR 22321 EN, European Commission, 2006.

[2] *Takayuki Nakano, OECD-HRP,* **The MOX fuel behaviour test IFA-597.4/.5./.6/.7; Thermal and gas release data,** Institutt of energiteknikk, Halden, June 2003.

[3] *R.B. Baker,* **Integral heat rate to incipient melting in UO_2-PuO_2 fast reactor fuel,** Hanford Engineering Development Laboratory, May 1978.

[4] *G.J.Hyland,* **Thermal conductivity of solid uo2: critique and recommendation 1982,** *J. Nuclear Materials 113 (125-132), 1983.*

[5] *D. R. Olander,* **Fundamental Aspects of Nuclear Reactors Fuel Elements**, Department of Nuclear Engineering, University of California, Berkeley, 1976.

[6] *http://en.wikipedia.org/wiki/Heat_transfer#Radiation*, Last check 22-09-2014.

[7] **SCDAP/RELAP5/MOD3.1 Code manual volume4: MATPRO—A library of materials properties for light water reactor accident analysis.**

[8] *Neil E. Todreas, Mujid S. Kazimi,* **Nuclear Systems I, thermal Hydraulic Fundamentals 1st edition,** Massachusetts Institute of Technology, 1990.

[9] *D.G. Martin,* **A reappraisal of the thermal conductivity of UO_2 and mixed (U,Pu) oxide fuels,** Journal of Nuclear Materials 110 (73-94), 1982.

[10] *Christian Duriez, Jean-Pierre Alessandri, Thierry Gervais, and Yannick Philipponneau,* **Thermal conductivity of hypostoichiometric low Pu content (U,Pu)O_{2-x} mixed oxide,** J. Nuclear Materials 277 (143-158), 2000.

[11] *K. Lassmann, A. Schubert, P. Van Uffelen, J. Van der Laar,* **TRANSURANUS handbook version v1m1j12,** JRC, ITU 2012.

[12] *L. Luzzi, S. Lorenzi, D. Pizzocri, D. Rozzia, A. Aly, A. Del Nevo,* **Modelling and analysis of nuclear fuel pin behaviour for innovative Lead cooled FBR,** Technical report September 2014.

[13] *K. Lassmann,* **TRANSURANUS: a fuel rod analysis code ready for use,** Journal of Nuclear Material 188 (295-302), 1992 .

[14] *P. Tolonen, M. Pihlatie, H. Fujii,* **The MOX fuel behavior test IFA597-4/5/6; Thermal and gas release data to a burn-up of 25 MWd/kgMOX,** HWR-652, OECD Halden Reactor Project, February 2001.

[15] *C.Ronchi, M. Sheindlin, M. Musella, and G.J. Hyland,* **Thermal conductivity of uranium dioxide up to 2900 K from simulations measurement of the heat capacity and thermal diffusivity,** J. Applied Physics 85, 1999.

[16] Juan J. Carbajo, Gradyon L.Yoder, Sergey G. Popov, and Victor K. Ivanov, **A review of the thermophysical properties of MOX and UO_2 fuels,** J. Nuclear Materials 299 (181-198), 2001.

[17] *Daniel Baron,* **Fuel thermal conductivity: A review of the modeling available for UO_2, (U-Gd)O_2 and MOX fuel,** Thermal performance of high burn-up LWR fuel, seminar proceedings, Cadarache, France, 3-6 March, 1998.

[18] *Y. Philipponeau,* **Thermal conductivity of (U,Pu)O_{2-x} mixed oxide fuel,** J. Nuclear Materials 188 (194-197), 1992.

[19] *S. E. Lemehov,* **MACROS: Modelling MADF and MABB fuels,** PELGRIMM. 3rd progress meeting. ENEA – Rome, March 27-28, 2014.

[20] EPMA. B. Vos, A. Leenaers and M. Verwerft, **On the analysis of Pu distribution in MIMAS MOX**.

[21] *IFE, OECD-HRP*, **Halden Boiling Water Reactor,** Institutt for energiteknikk, Halden January 2003.

[22] *J. a. Turnbull,* **Fuel Behavior Data Available from IFE-OCDE Halden Project for Development and Validation of Computer Codes,** Review of Nuclear Fuel Experimental Data. OECD-NEA, 1995.

[23] *D. Rozzia, A. Del Nevo, A. Ardizzone, M. Tarantino,* **Modeling of FGR in BWR Fuel Rods Based on IFA-409 Database,** ENEA CR Brasimone internal report FM-N-R-046IFA-409, 2013.

[24] *Compiled by Terje Tverberg,* **Mixed oxide (MOX) fuel performance benchmark,** OECD 2007.

[25] *J.T. Maki, J.E. Meyer,* **LWR fuel performance analysis fuel cracking and relocation,** Energy laboratory report No:MIT-EL 78-038. October, 1978.

[26] *D. Rozzia, N. Forgione, A. Ardizzone,* **Analysis of high burn-up MOX fuel behavior under normal operation and DBA conditions,** August 2013.

[27] http://en.wikipedia.org/wiki/Experimental_Breeder_Reactor_II, Last check 19-02-2015.

[28] http://www.ne.anl.gov/About/reactors/frt.shtml#fragment-1, Last check 19-02-2015.

[29] *Leonard J. Koch,* **Experimental breeder Reactor (EBR-II) An integrated experimental fast reactor nuclear power station,** Authorized by Argonne national laboratory 2008.

[30] **http://www.pelgrimm.eu**, Last check 29-04-2015.